

LONG-TERM SPECTROSCOPIC SURVEY OF THE HYADES CLUSTER: THE BINARY POPULATION

GUILLERMO TORRES, ROBERT P. STEFANIK, AND DAVID W. LATHAM

Center for Astrophysics | Harvard & Smithsonian, 60 Garden St., Cambridge, MA 02138, USA; gtorres@cfa.harvard.edu

Accepted for publication in The Astrophysical Journal Supplement Series

ABSTRACT

We report the results of a radial velocity monitoring program in the Hyades region, carried out at the Center for Astrophysics over a period of more than 45 yr. Nearly 12,000 spectra were gathered for 625 stars brighter than $V \approx 14.5$, of which 55% are members or possible members of the cluster. New or updated spectroscopic orbital solutions are presented for more than 100 members and non-members, including several triple systems. In a few cases we incorporate available astrometry. The frequency of binaries in the Hyades with periods up to 10^4 d is determined to be $40 \pm 5\%$, after corrections for incompleteness. This is marginally higher than in other open clusters. The orbital period and eccentricity distributions are found to be similar to those of solar-type binaries in the field. The mass ratio distribution is essentially flat, or slightly rising toward mass ratios of unity. We revisit the determination of the tidal circularization period, obtaining a longer P_{circ} value of 5.9 ± 1.1 d compared to the previous estimate of 3.2 d, still somewhat short of the value expected if most or all of the action of tides happens during the pre-main-sequence phase. We estimate a line-of-sight velocity dispersion of 0.21 ± 0.05 km s⁻¹ within 5.5 pc of the cluster center (approximately the half-mass radius) and a larger dispersion beyond that distance. Our velocity measurements are accurate enough to clearly reveal the signatures of gravitational redshift and convective blueshift among the dwarfs and giants in the Hyades.

1. INTRODUCTION

The assemblage of stars we know today as the Hyades cluster has been recognized since antiquity by its familiar ‘V’ shape, formed by five member stars brighter than the 4th magnitude, plus Aldebaran, which is not a member. Because of its proximity (~ 47 pc) and moderately rich membership, the Hyades has served for many decades as an essential laboratory for stellar astrophysics. It has provided the basis for the construction of some of the most fundamental maps of astronomy, including the mass-luminosity relation and the location of the main sequence in the Hertzsprung-Russell diagram. Throughout much of the 20th century, the distance to the Hyades was an important initial stepping stone for the determination of the extragalactic distance scale.

In many respects, it is a well-studied cluster: its membership has been investigated in great detail (e.g., Gaia Collaboration et al. 2018), and its age (~ 700 Myr) and chemical composition are known (e.g., Gossage et al. 2018; Dutra-Ferreira et al. 2016). We now have a fairly good picture of its internal structure and kinematics, and we know of the presence of extended tidal tails on either side, resulting from the interaction with the Galactic potential (Meingast & Alves 2019). The activity level and rotational properties of many of its member stars have been examined (Savanov & Dmitrienko 2018), as well as their X-ray emission (Freund et al. 2020). The cluster has also been a fertile hunting ground for exoplanets, and a number of them have already been found (see, e.g., Quinn et al. 2014; Mann et al. 2018; Mayo et al. 2023; Distler et al. 2025).

On the other hand, even though scores of spectroscopic binary and multiple systems have been identified in the Hyades, the statistical properties of this important segment of the population have yet to be investigated. This

is somewhat surprising for such a well-known cluster. It stands in contrast with the status of several other classical open clusters including NGC 188 (Geller et al. 2013; Narayan et al. 2026), M67 (Geller et al. 2021), NGC 7789 (Nine et al. 2020), and the Pleiades (Torres et al. 2021), for which definitive studies of their binary constituents have already uncovered their key properties. The present paper aims to remedy this situation.

Binary searches in the Hyades have been carried out both astrometrically (e.g., Mason et al. 1993; Patience et al. 1998) and spectroscopically, with the latter method being the most effective for characterizing multiple systems in greater detail. The history of radial velocity (RV) observations in the Hyades is as old as the technique itself. The earliest measurements were made in the 1890s (see Campbell 1928), and the first spectroscopic orbits for binaries in the cluster made their appearance in the literature shortly after (e.g., 63 Tau, Jantzen 1913; θ^2 Tau, Russell 1914; Plaskett 1915). Since then, several dedicated observing campaigns have been carried out to measure RVs for stars in this region (e.g., Wilson 1948; Kraft 1965; Detweiler et al. 1984), although in general those efforts were not sustained for more than a few years. An exception is the program conducted by Roger Griffin and his collaborators (Griffin & Gunn 1974), which started in the early 1970s and ran for four decades, comprising some 350 stars. The last major data release from this effort was published in a lengthy 172-page monograph reporting about 3000 RV measurements (Griffin 2012). Those measurements supported the determination of 52 newly derived spectroscopic binary orbits in the Hyades field, adding to the several dozen others published earlier by that team.

A few years after the start of Griffin’s project, a similar but independent long-term RV monitoring program

was initiated at the Center for Astrophysics (CfA) (Stefanik & Latham 1985), and has now been completed. It has run for more than 45 yr since the end of the 1970s, and includes nearly twice as many stars in the Hyades region. While there is considerable overlap with Griffin’s study in terms of the scope, the target list, and the time coverage, our survey has shown that the harvest of spectroscopic binaries in the cluster had by no means been exhausted. We have now been able to determine the orbits of several dozen new systems, some with very long periods, but also some with short periods that had been missed. This has benefited in part from the complementary nature of the observations from the two surveys, which in many cases has allowed us to fill in the gaps in the orbital phase coverage. The enlarged sample of spectroscopic binaries provides the basis for a long overdue analysis of their properties, including the distribution of orbital periods, eccentricities, and mass ratios, as well as the overall binary frequency. All of these are important ingredients for population synthesis of clusters (e.g., Hut et al. 1992) and for the study of their dynamical evolution.

The plan for the paper is as follows. Section 2 explains the selection of our sample of 625 targets in the Hyades region, and is followed in Sections 3 and 4 with a description of the spectroscopic observations and the determination of RVs for single-, double-, and triple-lined objects. The procedures for solving the spectroscopic orbits, which in many cases incorporated additional RVs from other sources, are presented in Section 5. Nearly three dozen of our binaries have orbital solutions independently reported by the Gaia mission. This section discusses those external solutions as well, and how they compare with ours. Section 6 explains how we decided when a star has a variable RV. Membership in the cluster is a key attribute, and our criteria for this are laid out in Section 7. Aside from having variable RVs, other indicators of binarity relying on astrometry are discussed in Section 8. These are used later in the paper to produce cleaner samples for extracting the distributions of binary orbital elements. Section 9 describes the determination of our detection sensitivity as a function of orbital period, eccentricity, and mass ratio. The following sections contain our main results concerning the binary frequency (Section 10) and the distribution of orbital properties (Section 11), as well as a discussion of tidal circularization in the Hyades. Then, in Section 12, we make a determination of the internal velocity dispersion in the cluster, and in the process we show that our RVs clearly reveal the effects of the gravitational redshift and convective blueshift. In Section 13 we present tentative evidence of rotation or shear in the cluster, and discuss its interpretation. Final remarks are found in Section 14. Three appendices provide additional information, including (A) the discussion of more complicated orbital solutions, such as those for triple systems or for objects that benefit from incorporating astrometric observations; (B) notes of interest for selected targets; and (C) graphical representations of our orbital solutions for the single- and double-lined binaries from the main text.

2. SAMPLE

The most conspicuous part of the Hyades cluster spans an area on the sky more than 20° across. Other members

are scattered much farther out. This does not include stars that are in the tidal tails of the cluster, revealed in recent years by the Gaia mission (see, e.g., Meingast & Alves 2019; Röser et al. 2019; Risbud et al. 2025). Some of those outliers may be as far as 800 pc, or more than 100° away from the center (Jerabkova et al. 2021). The classical photographic studies of cluster membership, on the other hand, focused mostly on the brighter members in the central parts of the Hyades (e.g., van Bueren 1952; Hanson 1975; Pels et al. 1975), and relied almost exclusively on astrometric or photometric information. Those were largely the lists of targets that this project drew from to begin with, extended down to the magnitude limits accessible to our facilities, $V \approx 14$ – 14.5 , depending on the telescope. The goal was to provide the missing radial velocities needed in many cases to confirm membership, and also to identify binary star candidates (Stefanik & Latham 1985). The initial target list of some 200 objects evolved with time to reach a current total of 625 stars, gradually incorporating many more objects that had been claimed or suspected to be members based on their proper motions or photometric properties, some quite removed from the center (e.g., Weis et al. 1979; Weis 1983; Perryman et al. 1998; Reid & Mahoney 2000; de Bruijne et al. 2001; Douglas et al. 2014, 2016, among other sources). In many cases, known or newly discovered visual companions of the main targets were included in the sample as well, when bright enough and far enough away from the brighter star to be observed separately.

As a result of the way the sample was assembled, the time coverage of our spectroscopic observations is somewhat inhomogeneous, but we estimate that our target list now includes the vast majority of true members of the cluster down to $V \approx 14.5$, along with many others in the general Hyades vicinity that have turned out to be unrelated field stars, as we explain below. The sky positions of our stars are shown at the top of Figure 1, in which objects that our analysis has shown are true members or possible members are marked with red circles. The bottom shows their change in position over 100,000 yr, with the proper motion vectors pointing toward the convergent point as a result of the common space motion.

Table 1 lists all targets with their SIMBAD names, coordinates in ascending R.A. order, and other information gathered from the third data release (DR3) of the Gaia catalog (Gaia Collaboration et al. 2023a). A running number (#) is added to facilitate referencing across other tables in the paper. Membership information is also provided (see below).

3. OBSERVATIONS

The first observation for this project was obtained on the night of 1979 November 5. Over the course of the more than 45 yr since, we have collected a total of 11987 usable spectra using four different instrument/telescope combinations at the Center for Astrophysics. Most (10156 observations) were gathered with three nearly identical copies of the Digital Speedometer (Latham 1992). These were echelle spectrographs delivering a resolving power of $R \approx 35,000$, coupled with intensified photon-counting Reticon detectors that recorded a single order about 45 \AA wide, centered on the Mg I b triplet near 5187 \AA . These instruments were attached to the (now closed) 1.5m Wyeth reflector at

Table 1
Sample of Targets in the Hyades Region

#	Name	R.A. (deg)	Dec. (deg)	Gaia DR3 ID	π_{DR3} (mas)	$\mu_{\alpha} \cos \delta$ (mas yr ⁻¹)	μ_{δ} (mas yr ⁻¹)	G (mag)	$G_{\text{BP}} - G_{\text{RP}}$ (mag)	Memb.
1	vB 157	33.94275	25.78265	106051542927008128	24.352 ± 0.033	176.818 ± 0.034	-65.175 ± 0.032	5.68	0.59	NM
2	HD 14127	34.33297	5.36082	2519811309169118848	14.819 ± 0.022	145.479 ± 0.025	17.050 ± 0.018	8.42	0.71	NM
3	HD 15094	36.54724	11.17938	24656689987510912	22.338 ± 0.024	109.003 ± 0.024	2.607 ± 0.020	9.05	1.04	NM
4	BD+14 400	36.64095	15.37348	76117304500935936	16.880 ± 0.181	181.504 ± 0.196	13.112 ± 0.186	9.28	0.98	NM
5	HD 15128A	36.75458	31.28798	132522762106356224	12.024 ± 0.026	88.185 ± 0.034	-30.672 ± 0.024	7.77	0.67	NM

Note. — For the target names, we have generally favored the SIMBAD designations most commonly used in the Hyades cluster, when available. For performing SIMBAD searches, those names should be prefixed with the cluster designation “Cl Melotte 25” for vB names, or “Cl* Melotte 25” otherwise. Other non-cluster names can be used as listed. Coordinates (ICRS, epoch 2016.0), source IDs, parallaxes, proper motion components, G -band magnitudes, and $G_{\text{RP}} - G_{\text{BP}}$ colors are from the Gaia DR3 catalog. The last column reports our assessment of membership in the cluster as ‘M’ (member), ‘M?’ (possible member), or ‘NM’ (non-member). An additional column in the electronic version of this table lists $\Delta\pi$, which is an additive adjustment to the Gaia DR3 parallaxes to correct for a systematic zero-point offset, as advocated by Lindegren et al. (2021). (This table is available in its entirety in machine-readable form.)

the Oak Ridge Observatory (in the town of Harvard, MA, USA), the 1.5m Tillinghast reflector at the Fred L. Whipple Observatory (Mount Hopkins, AZ, USA), and the 4.5m-equivalent Multiple Mirror Telescope, also on Mount Hopkins, before its conversion to a monolithic 6.5m mirror in 1998. Signal-to-noise ratios varied greatly depending on brightness and sky conditions. The reduction of these spectra used procedures described by Latham (1985, 1992).

The stability of the velocity zero-point for the Digital Speedometers was monitored by gathering exposures of the sky at morning and evening twilight. Based on those observations, small velocity corrections typically under 2 km s⁻¹ were applied to the raw velocities from run to run, in order to place them all on the same native CfA system. Several dozen minor planets in the Solar System were also observed regularly with these instruments. Examination of those observations, reduced in the same way as the science exposures, has determined that the native CfA system is slightly offset from the IAU system by 0.14 km s⁻¹ in the negative direction (Stefanik et al. 1999).¹ In order to remove this shift, we applied a correction of +0.14 km s⁻¹ to all our raw velocities with the Digital Speedometers described in the next section.

The Digital Speedometers were used until March of 2009, when the last of those instruments was retired. Starting in September of that year, we began using the Tillinghast Reflector Echelle Spectrograph (TRES; Fűrész 2008; Szentgyorgyi & Fűrész 2007) on the 1.5m telescope in Arizona, which is a modern, bench-mounted, fiber-fed instrument with a CCD detector. It delivers a resolving power of $R \approx 44,000$ in 51 orders, covering the wavelength range 3800–9100 Å. We collected a total of 1831 spectra with this instrument, through the end of the 2025/2026 observing season. The reductions were performed with a dedicated pipeline (see Buchhave et al. 2012). The velocity zero-point of TRES was monitored with observations of IAU standard stars each run, and observations of minor planets were again used to transfer the raw velocities to the IAU system, as done with the Digital Speedometers.

In Table 2 we list for each object the time span of the observations and the number of Digital Speedometer and TRES spectra we gathered, along with other information

¹ Note that the offset was inadvertently given with the wrong sign in the original publication.

discussed later. The distributions of the time span and number of observations per object are shown in Figure 2.

4. RADIAL VELOCITIES

For the single-lined objects in our sample, radial velocities and corresponding uncertainties were obtained by cross-correlation using the IRAF task XCSAO (Kurtz & Mink 1998). The templates were chosen from a large library of synthetic spectra based on model atmospheres by R. L. Kurucz, and a line list that was fine-tuned by Jon Morse to improve the match to real stars (see Nordström et al. 1994; Latham et al. 2002). The templates cover the region between 5050 Å and 5350 Å, and are available over wide ranges in effective temperature (T_{eff}), projected rotational velocity ($v \sin i$)², surface gravity ($\log g$), and metallicity ($[M/H]$). As all but four of our targets are on the main sequence, we adopted $\log g = 4.5$, which is sufficiently close for our purposes. For the four giants (vB 28, vB 41, vB 70, and vB 71), we used $\log g = 2.5$. The metallicity was held fixed at the solar value, as the composition of the Hyades is only slightly higher ($[Fe/H] = +0.18$; Dutra-Ferreira et al. 2016). The optimal template for each star was determined by running grids of correlations in temperature and $v \sin i$, and selecting the one giving the highest correlation value averaged over all exposures (see Torres et al. 2002). The temperature and $v \sin i$ values adopted in each case are included in Table 2, and their distribution is shown in Figure 3. As the Digital Speedometer spectra are limited to a narrow wavelength range around the Mg Ib triplet, the velocities from the TRES spectra were calculated using the 100 Å order centered on the same region, for consistency, and also because in our experience this is the part of the spectrum that captures most of the velocity information.

For objects in our sample showing two or three sets of lines, RVs were derived using the two-dimensional cross-correlation technique TODCOR (Zucker & Mazeh 1994) and its extension to three dimensions (TRICOR; Zucker et al. 1995). The optimal template parameters were determined in a similar way as above, and are listed below in Table 7 for the double-lined targets. Those for triple-

² We use $v \sin i$ here as shorthand, although this is strictly the total line broadening, including contributions from other effects such as macroturbulence. Our templates were calculated with a fixed macroturbulent velocity of $\zeta_{\text{RT}} = 1 \text{ km s}^{-1}$, representative of main-sequence stars.

Table 2
Statistics of Spectroscopic Observations For Our Targets

#	Name	Time span (day)	N_{DS}	N_{TRES}	N_{tot}	Mean RV (km s^{-1})	e/i	$P(\chi^2)$	RV _{kin} (km s^{-1})	Memb.	T_{eff} (K)	$v \sin i$ (km s^{-1})	M_1 (M_{\odot})	Binarity
1	vB 157	850.8	7	0	7	25.623 ± 0.338	0.931	0.4117	20.858	NM	6750	10	...	
2	HD 14127	843.9	6	0	6	27.116 ± 0.492	0.956	0.4051	21.194	NM	6250	6	...	
3	HD 15094	2807.1	10	0	10	19.428 ± 0.473	0.881	0.5867	22.992	NM	5250	4	...	
4	BD+14 400	279.3	0	3	3	16.071 ± 0.145	1.084	0.2982	23.075	NM	5250	4	...	DUP,RUWE
5	HD 15128A	3902.3	5	0	5	23.376 ± 1.182	0.788	0.5653	22.095	NM	6750	50	...	DUP

Note. — Columns N_{DS} and N_{TRES} contain the number of Digital Speedometer and TRES observations, and N_{tot} is their sum. The following column is the weighted mean RV, followed by the e/i statistic and χ^2 probability described in Section 6. The next two columns contain the expected (astrometric, or kinematic) RV of each target, and their membership assessment (Section 7). We then list the T_{eff} and $v \sin i$ adopted for the templates of the single-lined objects, where ‘Barnard’ means we used an observed spectrum of Barnard’s star (GJ 699) as the template. The templates for the double- or triple-lined objects are given in Table 7 below, or specified in Appendix A or B. The next column lists approximate values of the stellar mass for members and possible members of the cluster with sufficient information to make those determinations. The masses were derived from Gaia photometry and a model isochrone for the Hyades, or rely on dynamical information, where available. For targets that are members of multiple systems, the value corresponds to the primary component (see Section 11.3). The final column gives information on binarity discussed later (Section 8). (This table is available in its entirety in machine-readable form.)

Table 3
Radial Velocity Measurements for Single-Lined Targets

#	Name	BJD (2,400,000+)	RV (km s^{-1})	Inst.
1	vB 157	48903.6887	25.57 ± 0.25	1
1	vB 157	48946.5639	25.36 ± 0.33	1
1	vB 157	49047.4652	26.19 ± 0.34	1
1	vB 157	49226.8129	25.96 ± 0.33	1
1	vB 157	49401.4669	25.15 ± 0.51	1

Note. — Radial velocity measurements and uncertainties. The last column indicates the instrument used (1 = Digital Speedometers; 2 = TRES). The velocities for two single-lined targets from our survey published previously are not listed here, and may be found in the original publication: vB 71 and vB 72 (Torres et al. 1997c). (This table is available in its entirety in machine-readable form.)

lined objects are given in Appendix A or B. In the case of the Digital Speedometers, previous work has shown that the small wavelength coverage can sometimes introduce systematic errors in the velocities from composite spectra, caused by lines of the binary components shifting in and out of the spectral order in opposite directions as a function of orbital phase. These spurious velocity shifts are typically less than 5 km s^{-1} , and were corrected based on numerical simulations as described by Latham et al. (1996) and Torres et al. (1997d). For TRES, with spectral orders that are more than twice as wide, these effects are negligibly small.

Finally, we note that for a few of our coolest targets we found that better results were obtained using an observed spectrum of Barnard’s star (GJ 699, M4 V) as the template.

The individual radial velocities and associated uncertainties for the single-lined objects, as returned by XCSAO, are listed in Table 3, and those for the double-lined objects are found in Table 4. Typical uncertainties for sharp-lined stars when using the Digital Speedometers are just under 0.5 km s^{-1} , and those for TRES are about half as large. Histograms of the RV uncertainties for the Digital Speedometers and TRES are shown in Figure 4.

5. ORBITAL SOLUTIONS

For objects in our sample with enough observations and clear evidence of velocity variations, we performed

Table 4
Radial Velocity Measurements for Double-Lined Targets

#	Name	BJD (2,400,000+)	RV ₁ (km s^{-1})	RV ₂ (km s^{-1})	Inst.
48	LP 413-18	56224.7984	66.78 ± 0.20	-13.95 ± 1.74	2
48	LP 413-18	56262.9048	35.45 ± 0.28	35.45 ± 2.47	2
48	LP 413-18	56282.6123	21.34 ± 0.25	53.65 ± 2.22	2
48	LP 413-18	56309.7136	45.29 ± 0.24	20.20 ± 2.09	2
48	LP 413-18	56346.6366	25.60 ± 0.19	50.01 ± 1.67	2

Note. — Radial velocity measurements and uncertainties for the primary and secondary components. The last column indicates the instrument used (1 = Digital Speedometers; 2 = TRES). The velocities for double- or triple-lined targets from our survey published previously are not listed here, and are to be found in the original publications: vB 120 (Torres et al. 2024b); vB 162, vB 23, vB 34, vB 182, vB 117, vB 119 (Torres et al. 2024a); PELS 20 (Torres et al. 2024c); vB 24 (Torres et al. 1997a); vB 57 (Torres et al. 1997b); vB 75 (Torres et al. 2019b); HAN 346 (Benedict et al. 2021). The RVs for four others (vB 53, vB 95, vB 124, vB 169) will be published in separate studies of those systems. (This table is available in its entirety in machine-readable form.)

weighted least-squares solutions to derive the elements of the single-lined or double-lined orbits (SB1, SB2). The weights were taken to be inversely proportional to the square of the RV uncertainties, σ_{RV} . As these errors are not always accurate, we adjusted them during the solutions by solving for a multiplicative scale factor F applied to σ_{RV} for each star, intended to achieve reduced χ^2 values near unity. These factors were solved for simultaneously with the standard orbital elements, which are P , γ , K_1 , e , ω_1 , and T_0 for SB1s, and the additional parameter K_2 for SB2s. Separate scale factors F_1 and F_2 were used for the primary and secondary in the SB2s.

For many of our targets, orbits have been published previously, mainly by Griffin and collaborators (Griffin & Gunn 1978; Griffin et al. 1982, 1985a, 1988; Griffin 2001, 2012, 2013, 2016), but also by other authors. We take the opportunity here to update those orbits by adding our own observations, which in a number of systems significantly improve the phase coverage, and therefore the accuracy and precision of the elements. For several of these binaries, more than one orbit has been published for the same object. In other cases, our orbital solutions based on our own measurements are new. When combining our velocities with others that may have a differ-

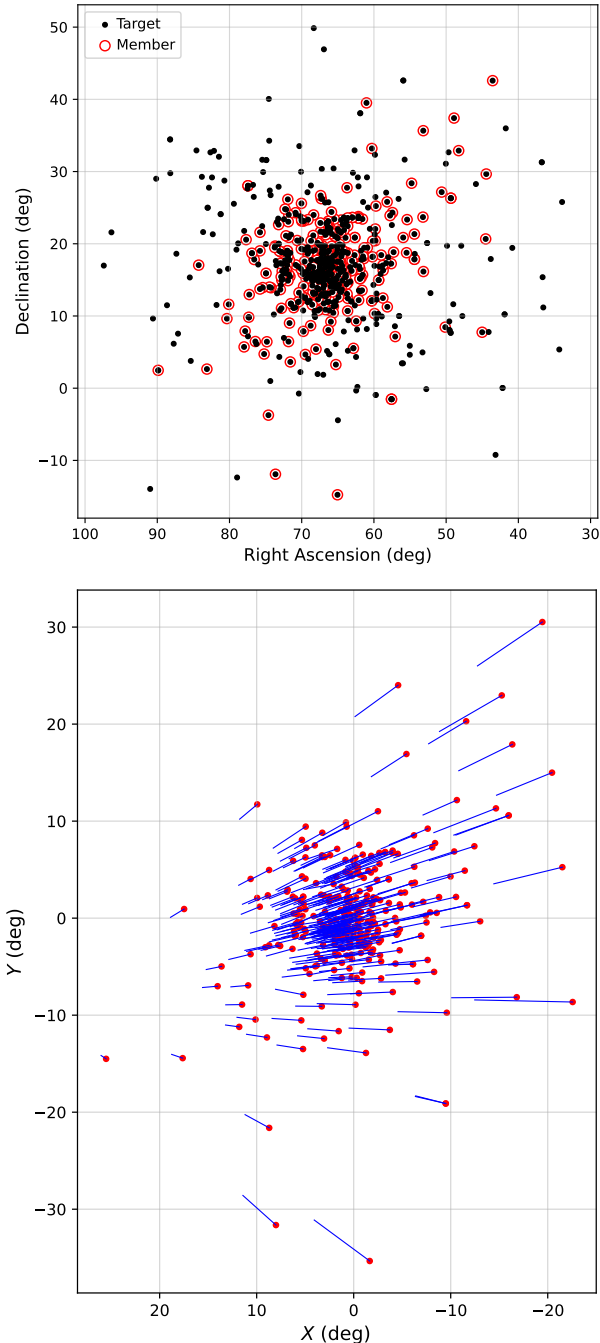


Figure 1. *Top:* Distribution of survey targets on the plane of the sky. Objects considered members or possible members of the Hyades are marked with red circles. *Bottom:* Proper motion vectors for members or possible members, showing the change in position over 100,000 yr. Stars are displayed in equatorial XY coordinates on the tangential plane centered on the cluster. Red dots mark the initial positions.

ent zero-point, we solved for one additional parameter for each external set of velocities, representing a possible systematic offset relative to the CfA system. We report those offsets only when they are statistically significant. Similarly, we have occasionally found and report significant systematic zero-point differences between the primary and secondary velocities in some of the SB2s, which are most likely caused by template mismatch.

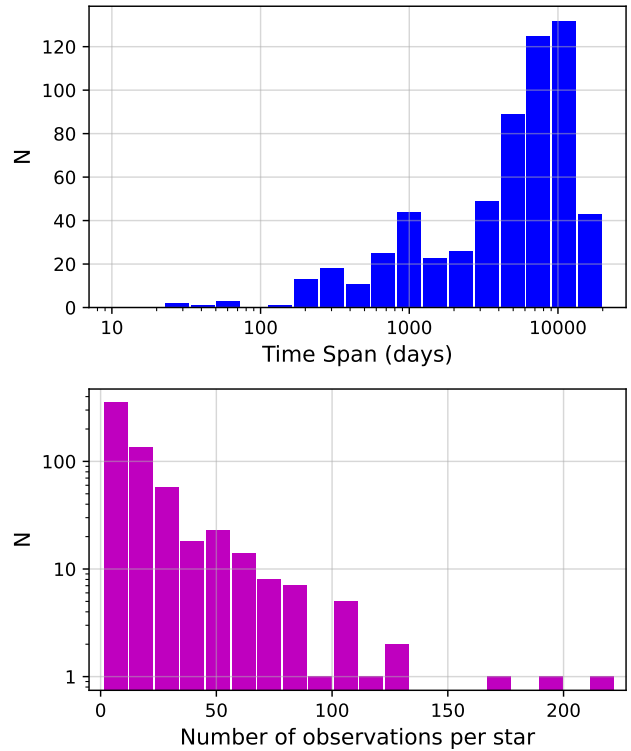


Figure 2. Histograms of the time span of our observations, and of the number of observations per target.

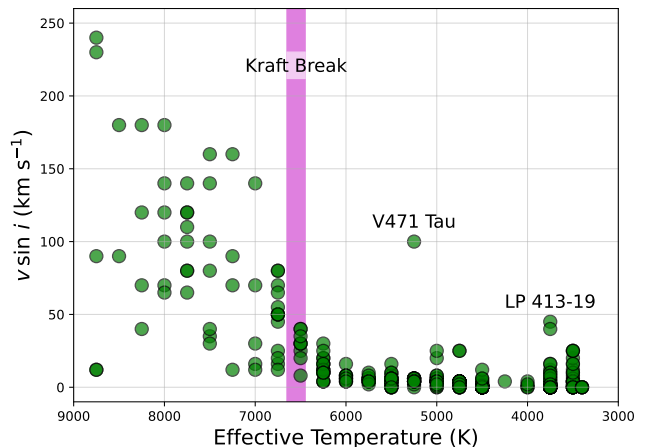


Figure 3. Distribution of the temperatures and $v \sin i$ values adopted for the templates of the Hyades members in our survey. The shaded area (as per Beyer & White 2024) marks the ‘Kraft Break’ (Kraft 1967), where stars transition from slow to rapid rotation as their outer convective envelopes disappear, and magnetic braking becomes ineffective. The two objects that stand out on the cool side of the break are spin-orbit synchronized stars belonging to the shortest period binaries in our sample: V471 Tau (the K dwarf in a system containing a white dwarf; $P = 0.52$ d) and LP 413-19 (both components shown; $P = 0.48$ d).

The orbital elements we obtain for the SB1s and SB2s are listed in Tables 5 and 6. Plots of the orbits along with the observations are shown in Appendix C. For the double-lined binaries, other parameters inferred from the orbital elements are given separately in Table 7, together with the secondary-to-primary spectroscopic flux ratios ℓ_2/ℓ_1 at the mean wavelength of our observations,

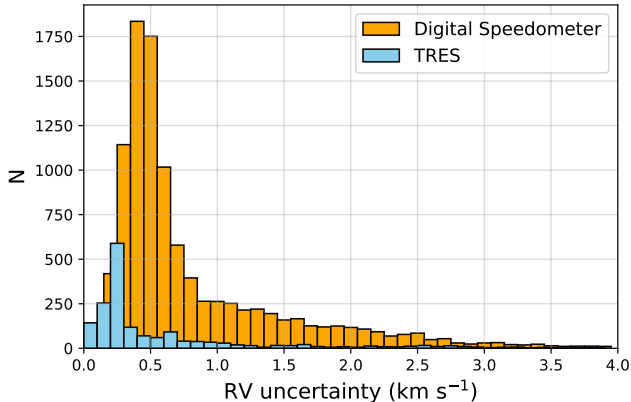


Figure 4. Histogram of the individual radial-velocity uncertainties for our single-lined objects, from the Digital Speedometers and the TRES instrument.

$\sim 5187 \text{ \AA}$. The sources of external velocity measurements used in some of our orbital solutions are listed in Table 8. In three cases (vB 30, HD 40512, vB 102) the velocity residuals from initial fits showed obvious long-term drifts caused by outer companions. For those systems, the final fits included the slope of the trend as an additional adjustable parameter, which we solved together with the other orbital elements. Those results are given in the notes to Table 5.

An additional set of RVs that we considered using is that of Bender & Simon (2008). These authors performed high-resolution near-infrared spectroscopy on more than two dozen targets selected from our survey, which were known only as single-lined spectroscopic binaries at the time. They detected the faint secondaries in 25 systems, and measured between 1 and 5 velocities in each case. Unfortunately, however, we have found those measurements difficult to use, mainly because of concerns about the velocity zero-point, the fact that only the RVs for the secondaries were reported, the significant uncertainties in some cases, and the limited phase coverage in others. Furthermore, in about a third of the systems our own observations also reveal the presence of the secondaries, allowing us to measure their velocities and achieve much more complete phase coverage. For these reasons, we have chosen not to incorporate these near-infrared measurements into our orbital solutions.

About a dozen of our objects are hierarchical triple or quadruple systems in which the inner and outer orbits can be determined. In some cases, available astrometry for the outer orbits allows the dynamical masses to be derived. Other targets are binaries with incomplete phase coverage, for which astrometric information can be folded in to complement the spectroscopy, and enable the orbit to be solved. These more complicated systems are dealt with separately in Appendix A. Table 9 lists all systems in our survey with multiplicity higher than two, for which the inner and outer orbits are known either from this work or the work of others.

Several other objects in our sample have astrometric orbits with orbital periods of decades or centuries, to which our velocities can contribute little. We list them in Table 10, with their periods, eccentricities, and membership information. For completeness, the table also includes all other targets in the survey with astrometric

orbits of any period, including ones for which the same orbit has been determined spectroscopically.

Finally, in a few of our targets with double-lined spectra, we are able to measure the velocities of both components using TODCOR, but we do not have enough of them to derive an orbital solution. In such cases, it is still possible to infer an accurate center-of-mass velocity γ , as well as the mass ratio $q \equiv M_2/M_1$, by employing a simple method described by Wilson (1941), although the idea goes much further back (e.g., Zurhellen 1907; Goos 1908). It involves fitting a straight line through pairs of primary and secondary velocities, which then allows one to solve for γ and q from the slope and intercept. Knowledge of γ , even if the full orbit is not determined, is very useful because it can be sufficient in some cases to immediately rule out membership in the cluster. Because both components have their own RV uncertainties, which can be very different in some systems, here we have implemented the procedure using orthogonal distance regression. The targets for which we used it are noted in Appendix B, and all turn out to be non-members.

5.1. The Griffin velocity zero-point

Throughout his extensive, decades-long program of spectroscopic observations in the Hyades region, R. Griffin maintained a consistent zero-point for his velocities that he reported was 0.8 km s^{-1} more positive than the IAU system (see, e.g., Griffin et al. 1988; Griffin 2012). We have observations for 47 of the SB1 systems he published over the years, and 15 of his SB2s. This allows us to compare his offset estimate with the shifts we have determined independently for each of these systems. We obtained a weighted average offset for the 62 binaries of Griffin – CfA = $+0.778 \pm 0.037 \text{ km s}^{-1}$, which is in excellent agreement with his assessment, on the assumption that our velocities are on the IAU system.

5.2. Comparison with Gaia DR3 orbits

The Gaia DR3 catalog contains orbital or trend solutions for some 800,000 binary or multiple systems of the astrometric, spectroscopic, or eclipsing kind, as well as combinations in some cases (e.g., Gaia Collaboration et al. 2023b). By necessity, these ‘non-single star’ solutions were carried out in a fully automated manner, and this effort has been largely successful. It is a remarkable achievement, given the complexity of the problem and limitations from either the sparseness, irregular distribution, or quality of the measurements, the broad range of stellar characteristics, or even confusion from higher-order multiplicity in many instances (see, e.g., Babusiaux et al. 2023; Gosset et al. 2025).

Gaia has reported full spectroscopic orbital solutions for 34 of our targets, derived from the mission’s RV measurements, or in some cases a combination of RVs and astrometric measurements. We consider 20 of these binaries to be true members of the Hyades (see below, Section 7). An additional 19 targets have astrometric-only solutions from Gaia, of which 14 belong to the cluster. Four of those are among the 34 that also have independent spectroscopic orbits, although the periods from the two kinds of solutions are not always the same. In one case (vB 67B, a non-member), the spectroscopic period from Gaia is 5.8 d and the astrometric one is 1112 d,

Table 5
Orbital Elements for the Single-lined Binaries in the Sample.

#	Name	P (day)	γ (km s ⁻¹)	K_1 (km s ⁻¹)	e	ω_1 (deg)	T_0 (BJD) (2,400,000+)	$f(M)$ (M_\odot)	$M_2 \sin i$ (M_\odot)	$a_1 \sin i$ (10 ⁶ km)	σ (km s ⁻¹) N_{obs}	F Memb.	Source
7	G 36-30	1228.6	31.721	6.518	0.4874	118.1	46635.6	0.02347	0.2863	96.15	0.342	1.164	4,14
7	G 36-30	1.0	0.092	0.068	0.0086	1.2	2.8	0.00063	0.0026	0.86	84	NM	
14	HD 17922	318.879	23.301	7.528	0.3361	107.7	52427.53	0.01178	0.2275	31.09	0.290	1.113	8
14	HD 17922	0.059	0.075	0.048	0.0063	1.3	0.97	0.00023	0.0015	0.20	92	M	
25	vB 158	20843	45.203	3.417	0.645	192.6	46095	0.0385	0.3377	749	0.271	1.019	5
25	vB 158	835	0.054	0.092	0.016	2.4	55	0.0027	0.0080	28	76	NM	

Note. — Uncertainties for the orbital elements and derived quantities are given in the second line for each system. The symbol T_0 represents a reference time of periastron passage for eccentric orbits, or a time of maximum primary velocity for circular orbits. $M_2 \sin i$ is the coefficient of the minimum secondary mass multiplying the factor $(M_1 + M_2)^{2/3}$. The first line of the penultimate column (F) represents the scale factor applied to the internal RV uncertainties to reach a reduced χ^2 of unity. Our membership assessment is listed immediately below F . The last column lists the external RV sources used in these solutions; the corresponding bibliographic references are listed in Table 8. Additional columns reporting the zero-point offsets of each external source relative to the CfA velocity system are included in the electronic version of this table. The offsets are in the same order as the source codes. For the three systems showing long-term RV drifts superimposed on the orbital motion, we obtained the following slopes: $d\gamma/dt = -0.147 \pm 0.020$ km s⁻¹ yr⁻¹ (vB 30), $d\gamma/dt = -0.0394 \pm 0.0082$ km s⁻¹ yr⁻¹ (HD 40512), and $d\gamma/dt = -0.0716 \pm 0.0038$ km s⁻¹ yr⁻¹ (vB 102). (This table is available in its entirety in machine-readable form.)

Table 6
Orbital Elements for the Double-lined Binaries in the Sample.

#	Name	P (day)	γ (km s ⁻¹)	K_1 (km s ⁻¹)	K_2 (km s ⁻¹)	e	ω_1 (deg)	T_0 (BJD) (2,400,000+)	σ_1 (km s ⁻¹) σ_2 (km s ⁻¹)	N_1 N_2	F_1 F_2	Source
48	LP 413-18	16.2493	34.72	28.9	43.1	0.501	284.0	56385.84	0.161	8	0.745	...
48	LP 413-18	0.0054	0.19	1.1	1.9	0.024	3.2	0.11	1.420	8	0.745	M
49	LP 413-19	0.47613265	35.16	119.6	125.9	0.0	...	59590.21672	3.192	16	0.914	...
49	LP 413-19	0.00000018	0.69	1.5	1.9	0.00056	4.005	16	0.917	M?
132	HG 7-97	4.52818	54.63	12.38	12.95	0.128	261	51041.90	1.388	14	0.842	...
132	HG 7-97	0.00044	0.31	0.62	0.65	0.044	16	0.19	1.471	14	0.890	NM

Note. — Uncertainties for the orbital elements are given in the second line for each system. The symbol T_0 represents a reference time of periastron passage for eccentric orbits, or a time of maximum primary velocity for circular orbits. F_1 and F_2 represent multiplicative scaling factors applied to the internal RV errors for the primary and secondary in order to achieve reduced χ^2 values near unity. The last column lists the external RV sources used in these solutions (first line), if any, and our membership assessment below. Bibliographic references for the external sources are given separately in Table 8. (This table is available in its entirety in machine-readable form.)

Table 7
Additional Properties for the Double-lined Binaries in the Sample.

#	Name	$M_1 \sin^3 i$ (M_\odot)	$M_2 \sin^3 i$ (M_\odot)	$a_1 \sin i$ (10 ⁶ km)	$a_2 \sin i$ (10 ⁶ km)	a_{tot} (R_\odot)	q	ℓ_2/ℓ_1	T_{eff} (K)	$v \sin i$ (km s ⁻¹)
48	LP 413-18	0.245	0.164	5.60	8.34	20.04	0.671	0.192	3750	0
48	LP 413-18	0.020	0.012	0.13	0.27	0.52	0.017	0.018	3750	0
49	LP 413-19	0.374	0.356	0.7830	0.824	2.310	0.950	0.84	3750	45
49	LP 413-19	0.012	0.010	0.0098	0.012	0.022	0.019	0.03	3750	40
132	HG 7-97	0.00380	0.00364	0.765	0.800	2.248	0.956	0.986	4250	2
132	HG 7-97	0.00045	0.00042	0.037	0.039	0.084	0.059	0.085	4250	1

Note. — Uncertainties for the derived properties are given in the second line for each system. The mass ratio is defined as $q \equiv M_2/M_1$. The last three columns list the measured flux ratio at ~ 5187 Å (ℓ_2/ℓ_1), and the T_{eff} and $v \sin i$ adopted for the primary and secondary templates (first and second line for each pair), where ‘Barnard’ means we used an observed spectrum of Barnard’s star (GJ 699) as the template. Five additional columns in the electronic version of this table include quantities $\Delta RV_{1,2,\text{CfA}}$, $\Delta RV_{1,2,\text{Other1}}$, and $\Delta RV_{1,2,\text{Other2}}$, which represent systematic primary/secondary offsets for the CfA measurements and for those from up to two external sources (the latter in the same order as they appear in Table 6). A further two columns, $\Delta RV_{\text{Other1}}$, $\Delta RV_{\text{Other2}}$, represent the zero-point offsets of up to two external sources (also in the order in which they appear in Table 6) relative to the CfA system. Offsets are only reported when at least one of them is statistically significant, or in the case of ΔRV_{Other} , when one of the external sources is from Griffin; otherwise they were set to zero in our solutions. (This table is available in its entirety in machine-readable form.)

Table 8
External Radial Velocity Sources.

Source	Source
3 Griffin & Gunn (1978)	16 Tomkin & Griffin (2002)
4 Griffin et al. (1985a)	17 Griffin (2016)
5 Griffin (2012)	18 Paulson et al. (2004)
6 Griffin et al. (1982)	19 Mermilliod et al. (2009)
7 Griffin (2001)	20 Mermilliod et al. (2007)
8 Griffin (2013)	21 Tokovinin (1990)
9 Tomkin (2003)	22 Vaccaro et al. (2015)
10 Tomkin (2005)	23 Tal-Or et al. (2019)
11 Imbert (2006)	24 Conti (1969)
12 Balona (1987)	25 Díaz et al. (2012)
13 Fekel & Henry (2005)	26 Elodie public archive ^a
14 Halbwachs et al. (2018)	27 Sophie public archive ^b
15 Halbwachs et al. (2020)	

Note. — These are the external RV sources used in some of our spectroscopic orbital solutions (see Tables 5 and 6). Sources #1 and #2, omitted here, correspond to our own Digital Speedometer and TRES measurements, respectively.

^a <http://atlas.obs.fr/elodie>

^b <http://atlas.obs.fr/sophie>

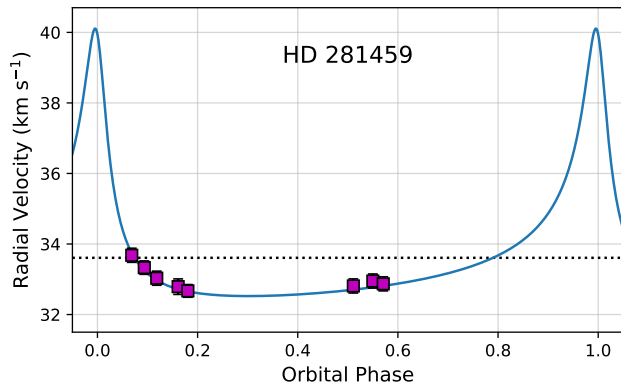


Figure 5. Our RV measurements for HD 281459, shown against the spectroscopic orbit from the Gaia DR3 non-single star solution. RV uncertainties are typically smaller than the symbol size.

implying it may be a hierarchical triple system. Our own four RV measurements for vB 67B show evidence of changes over the long term, but curiously, not over the short term, which should presumably have larger amplitude.

A comparison of our own orbital solutions against those from Gaia reveals that in eight cases the periods and other elements from Gaia are incorrect, or deviate significantly from ours. All are members of the cluster. On the other hand, 11 of our targets have new orbital solutions from Gaia that our survey has missed, due to insufficient observations or limited time or phase coverage. Only three of those are regarded as members of the Hyades. Two have astrometric-only orbits (HAN 291, vB 123), and the other, HD 281459, has a spectroscopic orbit. Our eight RV measurements for this last one are in excellent agreement with the Gaia solution (see Figure 5), which has a period of 721 d and is quite eccentric ($e = 0.75$).

6. RV VARIABILITY

To assess whether the velocity of a star in our sample is variable, we have chosen to rely on the e/i (exter-

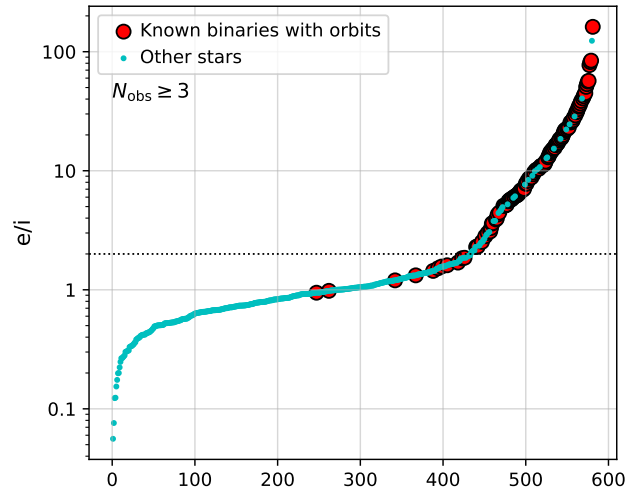


Figure 6. Values of e/i sorted in increasing order for the targets in our sample. Known binaries are marked as labeled, and the dotted line at $e/i = 2$ represents the adopted threshold for this work, above which stars are considered to be binaries.

nal/internal) statistic, which is defined for a given object as the ratio between the standard deviation of the measured RVs and the measurement precision. It has commonly been used to identify variables in a number of other spectroscopic surveys (e.g., Mermilliod et al. 1992; Geller et al. 2015; Torres et al. 2021). We calculated it here as described by Hole et al. (2009), using the individual measurement precision for each observation. Some authors have occasionally adopted the χ^2 probability as a measure of variability. We have found, however, that it is much more sensitive to outliers than e/i , and we therefore prefer the latter as a more conservative metric.

Figure 6 shows the e/i values, sorted in increasing order, for all stars in our sample with three or more observations. Objects with known spectroscopic orbits are indicated with larger red dots. The distribution displays a noticeable change in slope (or “knee”) at a value near $e/i = 2$. Most of the objects with higher values than this are in fact known spectroscopic binaries with orbits, as reported in the previous section. This appears, therefore, as a natural threshold for variability, and we adopt it for our work. It is marked by the dotted line in the figure. There are, however, about a dozen objects that have e/i below this threshold, and that are also known spectroscopic binaries. Not surprisingly, they tend to be systems with long orbital periods and small velocity semiamplitudes. It is quite possible there are other such low-amplitude binaries in our sample with $e/i < 2$, but they would be spectroscopically undetectable given our measurement precision. The figure also shows there are some three dozen objects not previously identified as binaries that have $e/i > 2$. In what follows we consider them to be velocity variables.

The e/i values for all our targets are included in Table 2. We additionally include the probability associated with the χ^2 value for each star, $P(\chi^2)$, for readers who would prefer to use that statistic as a measure of variability.

Table 9
Triple and Quadruple Systems in the Survey with Known Inner and Outer Orbits.

#	Name	P_{inner} (d)	P_{outer}	Memb.	Notes and sources
101	LP 301-69	5.418682	4810 d	NM	Triple, Appendix A
162	PELS 20	2.39436657	43.13 yr	M	Triple, Torres et al. (2024c)
198	vB 22	5.60921410	3077.8 d	M	Triple, Appendix A
250	HD 27691	4.00018569	246.9 yr	M	Triple, outer orbit by Josties & Mason (2021)
288	HAN 346 BC	0.7492425	988.0 d	M	Quadruple, Benedict et al. (2021)
357	vB 75	21.254396	40.752 yr	M	Triple, Torres et al. (2019b)
440,439	HD 29205 A,B	10.691399792	965 yr	NM	Triple, premature outer orbit by Izmailov (2019)
443	vB 102	734.09	124.9 yr	M	Triple, outer orbit by Tokovinin (2021c)
450	vB 304	60.80936	8310 d	M	Triple, Appendix A
466	vB 185	276.7678	79.2 yr	M	Triple, Appendix A
526	vB 124A	143.586	95.10 yr	M	Quadruple, Tomkin et al. (2007)
526	vB 124B	496.7	95.10 yr	M	Quadruple, Tomkin et al. (2007)
585	HD 34031	78.5400	848.9 d	NM	Triple, Appendix A
622	vB 169A	4.4475858	6809.9 d	NM	Quadruple, Fekel et al. (2002)
622	vB 169B	4.7835361	6809.9 d	NM	Quadruple, Fekel et al. (2002)

Note. — The inner and outer periods are given for each subsystem.

Table 10
Visual Binary Systems in the Survey with Known Astrometric Orbits.

#	Name	WDS name	P (yr)	a'' (")	e	Memb.	Notes
5,6	HD 15128 A,B	02270+3117	1041	2.47	0.86	NM	Premature orbit; constant RVs for A and B
7	G 36-30	02433+1926	1214 d	0.03124	0.5210	NM	SB1 with the same period
40	vB 3	03305+2006	31.46	2.94	0.395	NM	Premature orbit
50	vB 5	03376+2121	110.0	0.848	0.434	M	Premature orbit; partial RV coverage
107	vB 9	04007+2023	16.728	0.113	0.287	M	SB1 with the same period

Note. — System properties (orbital periods, semimajor axes, and eccentricities) are taken from the Sixth Catalog of Orbits of Visual Binary Stars (<https://www.astro.gsu.edu/wds/orb6/orb6frames.html>), consulted on 2026 January 30. Bibliographic references may be found therein, or where indicated in the notes. Orbital periods are given in years, with a few exceptions given in days. (This table is available in its entirety in machine-readable form.)

7. MEMBERSHIP

In order to identify which of our targets belong to the Hyades, we relied primarily on their proper motions and parallaxes from Gaia DR3, their G magnitudes and $G_{\text{BP}} - G_{\text{RP}}$ colors, and their RVs as determined here. For the latter, we adopted either the weighted mean for each object (Table 2), or the center-of-mass velocity, for systems with known orbits. The parallaxes were corrected for the known systematic zero-point offset following Lindgren et al. (2021).

Three conditions were required for membership. The first was that the location in the absolute magnitude vs. color diagram must be consistent with what is expected for known members. We ignored extinction, which is negligibly small for the Hyades, and allowed for objects to be slightly above the main-sequence, as would be expected if they are binaries or higher order multiples, or slightly below, to account for errors in the magnitudes or the parallax. The second condition for membership was that the radial velocity should be close to the value expected from the assumption of a common space velocity for all cluster stars. Such predicted RVs (or “astrometric” RVs; see, e.g., Dravins et al. 1999) depend on the sky position of the star and the known components of the space velocity vector of the cluster, along with the coordinates of the convergent point, all of which we adopted from Gaia Collaboration et al. (2018), with their formal errors. The difference ΔRV between the spectroscopic and astrometric velocities was considered to satisfy the criterion for membership when it was less than three times its formal

uncertainty. The uncertainty included not only the errors of both velocities, but also a term added in quadrature to account for the internal dispersion of the cluster in the radial direction ($\sigma_{\text{cl,RV}} = 0.40 \text{ km s}^{-1}$; Gaia Collaboration et al. 2018).³ The third condition for membership, also under the assumption of a common space motion, was that the component of the proper motion perpendicular to the direction to the convergent point, μ_{\perp} , must be small. As with the velocities, we adopted a 3σ threshold, where the uncertainty for each star i was constructed from the quadrature sum of the errors coming from the proper motion components and a term for the dispersion in the plane of the sky. This 2D dispersion term, converted to angular measure (mas yr^{-1}), was taken to be $\pi_i \sqrt{2} \sigma_{\text{cl,RV}} / 4.74047$, assuming that the velocity distribution in the cluster is isotropic. As the proper motions depend on distance, and the Hyades has a significant depth along the line of sight, we normalized μ_{\perp} by multiplying it by the ratio π_{cl}/π_i of the parallaxes, where the mean cluster parallax was taken also from Gaia Collaboration et al. (2018).

Application of the criteria outlined above is complicated by the presence of binaries, whether recognized or not. Even if binarity is recognized (e.g., as indicated by a large e/i value, or a visible trend in the velocities), the mean RV we compute for any given object will generally

³ As will be shown later in Section 12, our own estimate of $\sigma_{\text{cl,RV}}$ is somewhat smaller, especially in the central regions of the cluster, although we prefer to retain the larger value in this section to be conservative.

deviate from the expected value unless the center-of-mass velocity of the system is known from a full orbital solution, and unless there are no additional companions. Furthermore, even if the spectroscopic orbit is known, binarity can also change the measured proper motion components, and therefore μ_{\perp} , particularly if the orbital period is long. This is because in most cases the proper motions from Gaia DR3 did not account for orbital motion when it was not possible to solve for an astrometric orbit simultaneously with the rest of the astrometric parameters. As a result, objects in our sample with known spectroscopic orbits may well satisfy the ΔRV condition, and even have a consistent location in the color-magnitude diagram, but may not meet our μ_{\perp} requirement, making it appear that they are non-members.

To aid in accounting for these complications, we considered additional information that might hint at, or in some cases confirm, the binary nature of an object. This included the Renormalized Unit Weight Error (RUWE) from Gaia (Lindegren 2018), which is a measure of the quality of the astrometric solution. RUWE values in excess of 1.4 can often be a sign of unmodeled binary motion. For each object, we also checked the `ipd_frac_multi_peak` parameter from the Gaia DR3 catalog, which indicates the fraction of the time the object appeared to have more than one peak in scans oriented in different directions. We also consulted the Washington Double Star catalog (WDS; Worley & Douglass 1997; Mason et al. 2001) for information on close companions⁴, as well as other sources available to us (Morzinski 2011). In a number of cases, visual orbits have already been derived, confirming the stars’ physical association. Yet another valuable resource is the catalog of astrometric accelerations of Brandt (2021), which provided homogenized proper motions from Hipparcos and Gaia at mean catalog epochs separated by almost 25 yr. Any significant difference ($> 3\sigma$) in either right ascension or declination was considered here to be a strong indication that the object is a binary, and therefore that our μ_{\perp} estimate might be affected. We note, however, that this information is only available for the relatively bright objects accessible to Hipparcos, which constitute less than half of our target list. Finally, in assessing the robustness of the mean RVs, we considered the number and distribution of measurements by examining plots of the velocity history for each object for subtle trends that may have gone unnoticed.

In view of the potential for biases from target multiplicity, it was deemed more practical to carry out the membership assessment manually, object by object. For those displaying any of the conditions described above, we chose to relax our general 3σ criteria on ΔRV and μ_{\perp} to some degree, to account for their binary nature. While this does bring an element of subjectivity to the procedure, we believe it also reduces the risk of excluding objects that might reasonably still be bona fide members of the cluster, especially ones with spectroscopic orbits that are the focus of the rest of this paper.

Not all of our 625 targets have all the information we needed in order to decide on their membership status. There are 21 that are missing either the Gaia parallaxes or proper motions, or one or more of the Gaia magni-

tudes. Several of these are close companions to other targets. In these cases, we have drawn the missing information from the Gaia DR2 or Hipparcos catalogs (Gaia Collaboration et al. 2018; van Leeuwen 2007), when possible, or done our best to make a judgment based on what is available.

We find that a total of 282 stars are clearly non-members, and we flag them as “NM” in Table 1 and Table 2. Borderline cases, of which there are 16, are noted as “M?”. The remaining 327 objects are considered confirmed members of the Hyades. Figure 7 (top) shows the Gaia color-magnitude diagram of the members and possible members from our survey. The bottom panel displays a histogram of the stellar masses, estimated mostly from Gaia photometry (Table 2); they range from about 0.4 to $2.4 M_{\odot}$. An independently constructed membership list of 920 objects based on Gaia DR3 was compiled by Gaia Collaboration et al. (2021) using different criteria, and offers a chance for an intercomparison. It includes 267 of the targets in our sample, with most of the others being below our magnitude limit. All but one of those 267 objects are confirmed members based on our own criteria. The exception (vB 184) is in the “M?” category, and shows a long-term trend in the RVs and a very large RUWE value, both of which signal it has a companion.

On the other hand, there are 76 targets in our sample that we consider to be members or possible members, and that are missing from the Gaia membership list. The brightest one, vB 71 ($G = 3.58$), is θ^1 Tau, a well-known binary member of the cluster. All except for 8 of the others also show indications of one or more companions, from spectroscopic and/or astrometric information. We suspect this may have caused them to be missed in the Gaia list. We discuss these signs of binarity in our sample next.

8. BINARITY

Statistically significant changes in the radial velocity of a star, as described in Section 6, can be evidence of its binary nature, although this generally only works for periods up to a few decades. Here we have taken advantage of other sources of information that increase our completeness, and that also extend the census of multiple systems in the Hyades into the realm of the astrometric binaries. In particular, the Gaia DR3 catalog (Gaia Collaboration et al. 2023a) contains a wealth of information in both regimes. This comes in the form of various flags relevant to binarity, as well as the actual detection of companions separate from the target, sometimes with their own measured parallaxes, proper motions, and photometry. This can allow for the confirmation of the physical association. However, Gaia is not complete at the smallest separations, and for DR3, close pairs are increasingly missing for separations below about $1''.5$ (see Fabricius et al. 2021), or are increasingly lacking measurements of their parallaxes and proper motions. Nevertheless, as many of our targets are fairly bright, they are accessible to the visual binary observers, who have been recording the presence of many companions over the last two centuries, in some cases down to separations as small as $0''.1$. These measurements, also used earlier in Section 7, are collected in the WDS catalog, which includes lunar occultation observations that can reach even smaller separations. Other indirect evidence of binarity

⁴ Consulted on 2024 August 12.

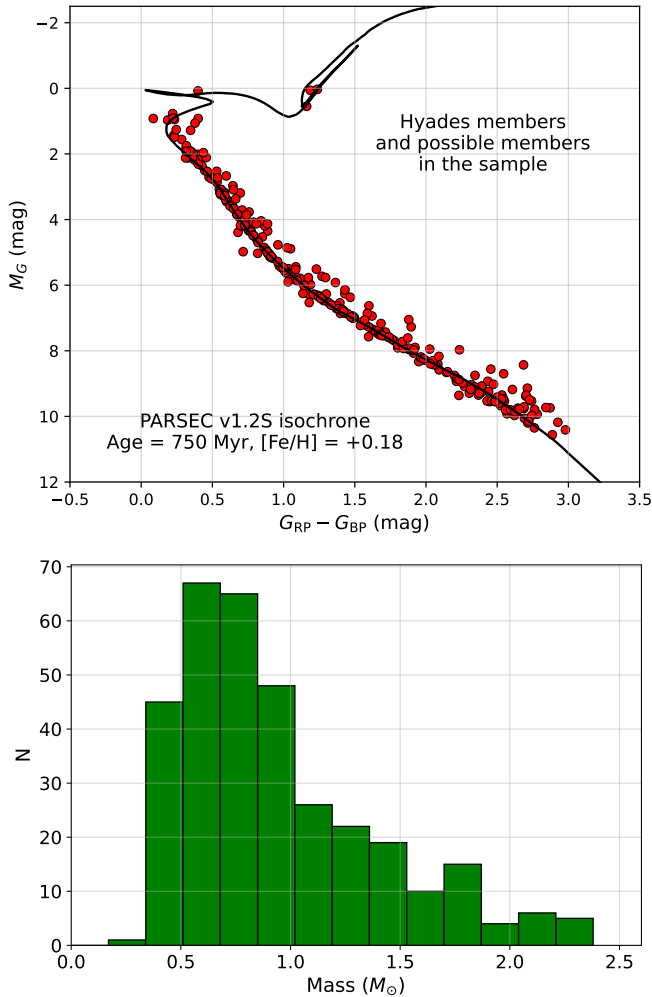


Figure 7. *Top:* Color-magnitude diagram of the Hyades from Gaia photometry, for all members (“M”) and possible members (“M?”) in our sample. Also shown is the model isochrone for the cluster we use throughout this paper, including color corrections as prescribed by Wang et al. (2025). *Bottom:* Distribution of stellar masses for objects in the top panel with sufficient information to make an estimate. For binary and multiple systems, the value shown is for the primary component (see Table 2).

comes from changes in the magnitude or direction of the proper motion at the mean epochs of the Hipparcos and Gaia surveys, as reported in the catalog of astrometric accelerations by Brandt (2021).

We have summarized the available information on binarity within our sample with a series of codes in Table 2, which we defined as follows. Targets that are either single-, double-, or triple-lined, and for which we have determined spectroscopic orbits (Tables 5–7, and Appendix A) are indicated with “SB1”, “SB2”, or “ST3”, respectively. For triple systems that are only single- or double-lined, we used “ST1” and “ST2”. Targets discussed in Appendix A are distinguished with a “+” sign at the end of the code, and those we have published previously have an added “p” at the end. For stars with no spectroscopic orbit but with $e/i > 2$, we use the code “VAR”. The few cases in which long-term trends in the RVs were detected visually, even if $e/i < 2$, are flagged as “LT”. Stars with significant changes in their proper motions ($> 3\sigma$ in either component) between the Hip-

parcos and Gaia DR3 catalog epochs, as listed by Brandt (2021), are given the code “ACC” (astrometric acceleration). If the Gaia DR3 catalog reported a RUWE value in excess of 1.4, we take that as an indication of unmodeled binary motion in the satellite astrometry, and assign the code “RUWE”. For other stars, more direct evidence of duplicity may come from the presence of more than one peak in the Gaia scans that were recorded along different directions (parameter `ipd_frac_multi_peak`); those situations are indicated with “DUP”.

Of the many stars with visual companions listed in the WDS, a few have more than one at different separations. Here we have considered only companions under $5''$, provided that Gaia observed them separately, that the physical association to our target is confirmed by the similarity of the parallaxes and proper motions, and that they were not observed spectroscopically by us as a separate target in our sample. These cases are indicated with “VB” in Table 2. If the Gaia mission did not observe these companions separately, or if it did, but no parallax or proper motion are available, then we only accepted them if the separations are less than $1''.5$, our adopted completeness threshold for Gaia.⁵ The same holds when two different visual companions are listed in the WDS (“VT”), indicating a triple system. A good number of these visual companions are listed in the WDS as having astrometric orbital solutions in the literature, which confirms their association. We indicate them with “VBO” or “VTO”, and in the case of the interesting hierarchical quadruple systems vB 124 and vB 169, as “VQO” (both of the inner orbits as well as the outer orbit are known). In many cases the astrometric companions are the same as the spectroscopic ones, i.e., the same orbits have been determined by both techniques. For such instances, the code indicating availability of an astrometric orbit is written in lower case letters.

The Gaia team has reported “non-single star” solutions of several kinds for about three dozen of our targets (see Holl et al. 2023; Halbwachs et al. 2023), as indicated earlier. This includes full spectroscopic orbits that we missed due to insufficient RV observations (flagged here as “GaiaSBO”), astrometric orbits in which Gaia was able to follow and model the center-of-light of the object (“GaiaVBO”), and objects showing obvious curvature in their paths on the plane of the sky, sometimes supported by a similar trend in the RVs from the satellite. These latter cases are similar in nature to those listed by Brandt (2021), and we assign them the code “GaiaACC”. Finally, the Gaia catalog contains entries for additional visual companions that are not listed in the WDS. If they are within $5''$ and are confirmed to be associated based on their parallaxes and proper motions, we accepted them and used the flag “GaiaVB”. If they cannot be confirmed in that way due to a lack of information, we accepted them as true companions only if they are within $1''.5$ of the primary, which makes it more likely that they are related.

A total of 347 of our targets have one or more indica-

⁵ Given the relatively large proper motion of the Hyades, in some cases it is possible to confirm the physical association of a companion lacking a parallax or proper motion by verifying that it has a small motion relative to the target, as measured at multiple epochs by visual observers. We have not pursued this possibility here.

tors of binarity, although many do not belong to the cluster. For objects we consider members or possible members of the Hyades, the percentage of stars with some evidence of multiplicity is quite high: 58% (198 out of 343 objects).

9. COMPLETENESS

Because the RV sampling for our targets is neither uniform nor complete, and there are limits to our velocity precision that degrades for rapid rotators, many spectroscopic binaries will have been missed. This is especially true for ones with long orbital periods, small secondary masses or mass ratios, and/or high eccentricities. To determine our sensitivity limits as a function of each of these parameters, we carried out simulations closely following the procedures of Torres et al. (2021). The reader is referred to that work for the full details (see also Geller et al. 2015). Briefly, we considered the 232 targets in our sample that are members of the Hyades, have three or more observations, and no indication of variability. We excluded objects for which spectroscopic or astrometric orbits have been published by Gaia or by others, even if we ourselves detected no variability. For each star, we generated 10,000 synthetic orbits with random orbital elements taken from suitable distributions for field stars, as described in the above references. For synthetic binaries with periods shorter than the tidal circularization period ($P_{\text{circ}} = 5.9$ d; see Section 11.4), we assumed circular orbits. Approximate primary masses sufficient for our purposes for each synthetic binary were obtained from a PARSEC v1.2S model isochrone for the Hyades from Chen et al. (2014), using photometry for our targets as listed in the Gaia DR3 catalog. We accounted for the color corrections to the models advocated by Wang et al. (2025). For each orbit, we predicted the RVs at the actual times of observation for each star, and added Gaussian noise corresponding to the actual RV error at each epoch. We then used the e/i criterion described earlier to determine whether the binary would be detected. The fraction of detected synthetic binaries represents our completeness.

The results indicate that our survey is highly sensitive to binaries with periods under 10 d (99.2% completeness), still very sensitive to those with periods up to 100 d (97.8%), and that we should detect 88% of systems with periods up to 1000 d. Completeness begins to fall off for longer periods, such that we are able to detect only about half of the systems with $1000 \text{ d} < P < 10^4 \text{ d}$, and very few beyond that. Our overall sensitivity up to periods of 10^4 d is 75%. This is very similar to the completeness level found by others in spectroscopic surveys of about the same duration and velocity precision as ours (e.g., in the M67 cluster; Geller et al. 2021). A histogram of our completeness as a function of orbital period is shown in the left panel of Figure 8.

While this paper does report a handful of spectroscopic orbits for cluster members with periods even longer than 10^4 d (~ 27 yr), in some cases they incorporate astrometric observations to constrain or determine the period (vB 185, $P \approx 28,600$ d; vB 80, $P \approx 63,000$ d), and in others they rely also on earlier RV measurements by R. Griffin (vB 176, vB 50, $P \approx 16,600$ d and 47,900 d), or the orbits were reported originally by other authors (vB 124, $P \approx 34,800$ d; Tomkin et al. 2007). Some of

these, and others (vB 75, PELS 20, $P \approx 14,900$ d and 15,800 d), are hierarchical triple or quadruple systems in which the inner orbits have also been determined. Because the completeness of our survey is far lower at these longer periods, we have chosen to restrict our attention to binaries with $P < 10^4 \text{ d}$.

Our completeness as a function of orbital eccentricity out to binary periods of 10^4 d decreases only slightly toward higher eccentricities. On the other hand, our sensitivity to binaries of different mass ratios is high for equal mass binaries, but not surprisingly, much poorer for small mass ratios, especially below $q = 0.2$ (see Figure 8).

10. THE MULTIPLICITY FRACTION IN THE HYADES

Because of its proximity, the discovery of binaries in the Hyades is likely to be substantially more complete than in other more distant clusters. This is especially true for the astrometric technique, thanks not only to the Gaia mission but also to the efforts of the visual binary observers since the 19th century, and to the observers of the precious but relatively rare lunar occultation events. Here we define the multiplicity fraction as the fraction of objects in our sample that are in multiple systems, including hierarchical triples and quadruples, provided that at least one of their periods is shorter than 10^4 d . We will also refer to it simply as the binary frequency.

Of the 343 targets in our sample that we consider to be members or possible members of the Hyades, 90 have known spectroscopic orbits with periods shorter than our cutoff: 53 are SB1s, 28 are SB2s, 7 are triples, and 2 are quadruples.⁶ A further 5 objects have variable RVs ($e/i > 2$) and are considered to be binaries as well. However, examination of the RV histories of these 5 stars shows that two of them (vB 328, vB 184) have slow upward or downward drifts over at least 10^4 d , indicating that their periods must be significantly longer. We therefore excluded them. For the other 3 (vB 290, vB 141, REID 88B) we assumed here that their periods are shorter, based on the fact that the vast majority of binaries with known orbits and $e/i > 2$ have periods under 10^4 d (see Figure 9).

The total number of spectroscopic systems is then $53 + 28 + 7 + 2 + 3 = 93$, which gives a raw multiplicity of $93/343 = 27\%$. After correction for our incompleteness up to 10^4 d (Section 9), we obtained $36 \pm 4\%$. This represents the spectroscopic binary fraction in the Hyades for stars of all spectral types (AFGKM). However, binary frequency estimates for other open clusters and field populations have typically focused on binaries with “solar-type” primaries (approximately FGK). If we restrict our estimate to just those spectral types for a more fair comparison (corresponding approximately to temperatures of 4000–7000 K, or masses of ~ 0.7 – $1.5 M_{\odot}$), the result is only a little different. We count 65 spectroscopic systems in our sample among the 217 FGK targets, for a raw frequency of $65/217 = 30\%$. After correction for incompleteness, this becomes $40 \pm 5\%$, which is slightly

⁶ Two of the SB1s (vB 30 and HD 40512) show long-term velocity trends superimposed on the orbital motion, indicating they are actually triple systems. However, this reclassification does not change the total number of systems, so our frequency calculations are unaffected. The third such case with a RV drift (vB 102) has a known outer orbit.

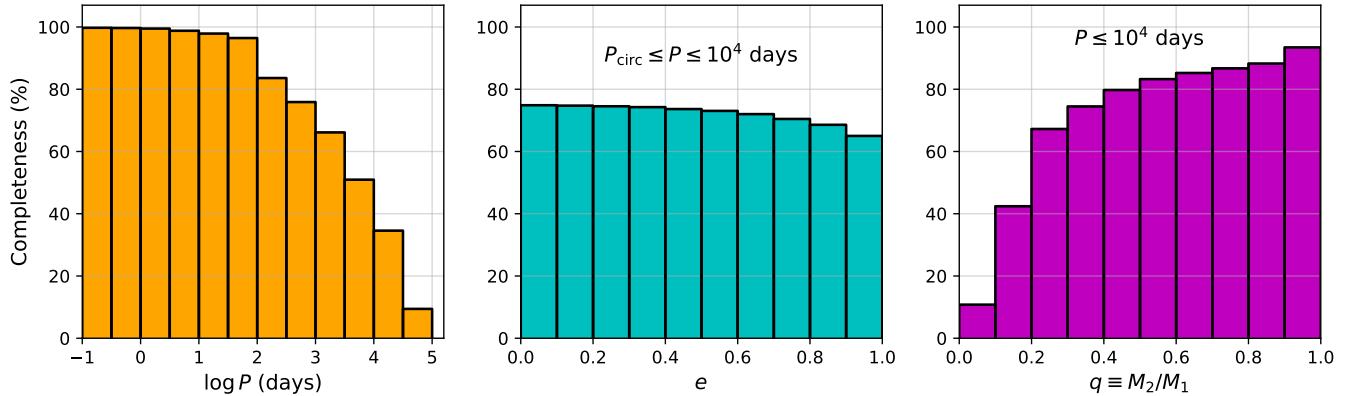


Figure 8. Results of our Monte Carlo simulations illustrating the sensitivity of our survey to spectroscopic binaries in the Hyades. The panels show our detection completeness as a function of orbital period, eccentricity (for $P_{\text{circ}} \leq P \leq 10^4$ d), and mass ratio ($P \leq 10^4$ d). Binaries with periods shorter than the circularization period P_{circ} , taken here to be 5.9 d (see Section 11.2), are excluded from the calculation of our sensitivity as a function of eccentricity because their orbits have typically been made circular by tidal forces.

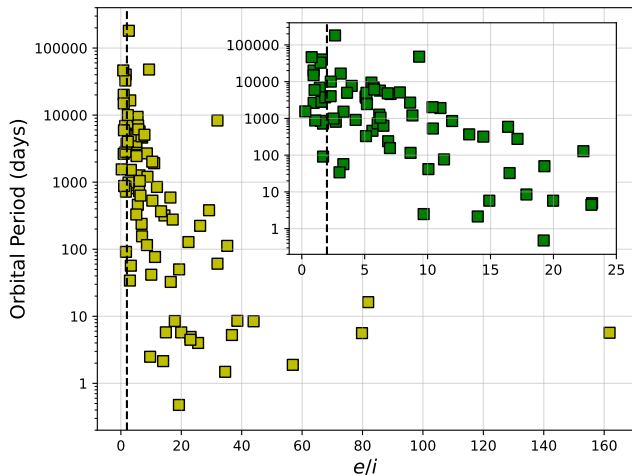


Figure 9. Orbital period as a function of the e/i statistic for members or possible members of the Hyades with known astrometric or spectroscopic orbits. The inset zooms in on the inner portion of the diagram ($e/i < 25$), and shows that most targets with $e/i > 2$ (marked with a dashed line) tend to have periods under 10^4 d, with very few exceptions. We may expect, then, that other objects with $e/i > 2$, which we consider to be binaries even though the orbits are unknown, will also typically have periods under 10^4 d, and we include them in the calculation of the multiplicity fraction.

higher than that found in other open clusters, and significantly higher than the halo and solar-neighborhood (field) samples, although the former has not been corrected for incompleteness. Table 11 summarizes these determinations, expanded from a similar table by Torres et al. 2021. As suggested above, the higher binary fraction in the Hyades may be caused in part by the more complete inventory of multiple systems in this cluster.

Aside from the spectroscopic systems, 3 of our targets were not detected as RV variables, but do have astrometric orbits with periods shorter than our cutoff (vB 122, HAN 291, vB 123). The first is from the WDS, and the other two are from Gaia. Many other objects in our sample are known to have close visual companions, although in most cases the information is limited to the angular separations and photometric properties. Nevertheless, these systems are of interest for computing the total (spectroscopic + astrometric) multiplicity fraction

Table 11
Spectroscopic Binary Frequency in the Hyades Compared with Other Populations.

Population	Age (Gyr)	Frequency (%)	Source
α Per	0.09	32 ± 9	1
Blanco 1	0.1	20 ± 6	2
Pleiades	0.125	25 ± 3	3
M35	0.15	24 ± 3	4
Coma Berenices	0.45	22 ± 8	5
Praesepe	0.7	30 ± 6	6
Hyades	0.7	40 ± 5	This paper
NGC 7789	1.6	31 ± 4	7
NGC 2506	2.0	35 ± 5	8
NGC 6819	2.5	22 ± 3	9
M67	4	34 ± 3	10
NGC 188	7	33 ± 4	11
Field	...	14 ± 2^a	12
Halo	~ 10	15 ± 2	13

Note. — Binary frequencies for mostly solar-type stars in different populations, generally up to orbital periods of 10^4 days, and generally corrected for incompleteness. Sources are: (1) Mermilliod et al. (2008a); (2) Mermilliod et al. (2008b); (3) Torres et al. (2021); (4) Leiner et al. (2015); (5) Mermilliod et al. (2008c); (6) Mermilliod & Mayor (1999); (7) Nine et al. (2020); (8) Linck et al. (2024); (9) Milliman et al. (2014); (10) Geller et al. (2021); (11) Narayan et al. (2026); (12) Raghavan et al. (2010); (13) Latham et al. (2002). The estimates for α Per, Blanco 1, Coma Berenices, Praesepe, and the halo sample have not been corrected for incompleteness.

^a We inferred this value from the work of Raghavan et al. (2010), by scaling their 44% total binary frequency for all periods (including triples and quadruples) by the fractional area of their log-normal period distribution up to periods of 10^4 d, for consistency with the typical cutoff period for the other samples.

in the Hyades. At the mean distance to the cluster, Kepler’s third law and an assumed typical binary mass of $\sim 1 M_{\odot}$ indicates that a period of 10^4 d corresponds to a semimajor axis of about $0''.2$, which we may assume is also a typical angular separation for such systems. We therefore considered targets with companions up to this separation, unless they are already in one of the other categories mentioned above. A total of 12 objects meet this condition. We obtained a corrected total multiplicity fraction of $41 \pm 4\%$ for stars of all spectral types, and $44 \pm 5\%$ for FGK stars. These should be considered lower limits, as the completeness for the astrometric systems is unknown.

11. DISTRIBUTION OF BINARY PROPERTIES

In the following subsections, we analyze the distributions of binary orbital periods, eccentricities, and mass ratios for confirmed cluster members and possible members in our sample, as well as the eccentricity-period relation. The total number of orbits with $P \leq 10^4$ d is 97, counting also 4 outer orbits of systems with multiplicity higher than two. This includes one outer orbit from the WDS (vB 122), as well as three spectroscopic or astrometric orbits from Gaia (HD 281459, HAN 291, vB 123). Out of these 97 orbits, we have ignored the one for the white dwarf binary V471 Tau, in which mass transfer has likely altered the orbital elements.

11.1. The Period Distribution

Figure 10 presents the histogram of the 96 Hyades binaries with orbital periods up to 10^4 d, in which we include triple and quadruple systems as well, and we count the period of each subsystem as if it were from an independent binary. We assume here, and in the following section, that internal dynamics in these higher-multiplicity systems have not modified the orbital elements significantly over the age of the Hyades. The bottom part of each bin corresponds to the binaries actually detected, and the top part adds the incompleteness correction from Figure 8, applied individually to each binary period. The dashed line represents the log-normal distribution for solar-type binaries in the field from Raghavan et al. (2010), with a mean of $\log P = 5.03$ and a standard deviation of $\sigma_{\log P} = 2.28$. We have normalized the field distribution to the same number of detected binaries up to 10^4 d, with the added incompleteness corrections.

In the bottom panel of Figure 10, we show the cumulative distribution of the observed periods, together with the log-normal field distribution (dashed line) from Raghavan et al. (2010), modified so that it reflects the same level of incompleteness as the real distribution. This latter curve was obtained by multiplying the Gaussian field distribution by our completeness function from Figure 8, and integrating. The Anderson-Darling test indicates that the shapes of the Hyades and field distributions are statistically indistinguishable (p value = 0.62).

In an earlier study, Duquennoy & Mayor (1991) presented a figure with the binary period distribution in the Hyades based on 45 systems taken from the work of Griffin et al. (1985a). They noted an apparent excess of short-period binaries between 1 and 10 d compared to the distribution of solar-type binaries in the field, as it was then known, and speculated this might be an evolutionary effect. They suggested that tidal forces may have shortened the periods of some systems, causing a pile-up at the present time, with the possibility that some of these binaries may eventually coalesce. Alternatively, a similar outcome could result from the mechanism invoked to produce W UMa systems (angular momentum loss in spin-orbit coupled binaries). However, it does not appear that the period distribution of Duquennoy & Mayor (1991) was corrected for incompleteness, so it is unclear how significant that feature was. Nevertheless, with a sample that is now more than twice the size of the one they had at the time, and proper corrections for incompleteness, the cumulative distribution function of Figure 10 still shows a small kink at that location, al-

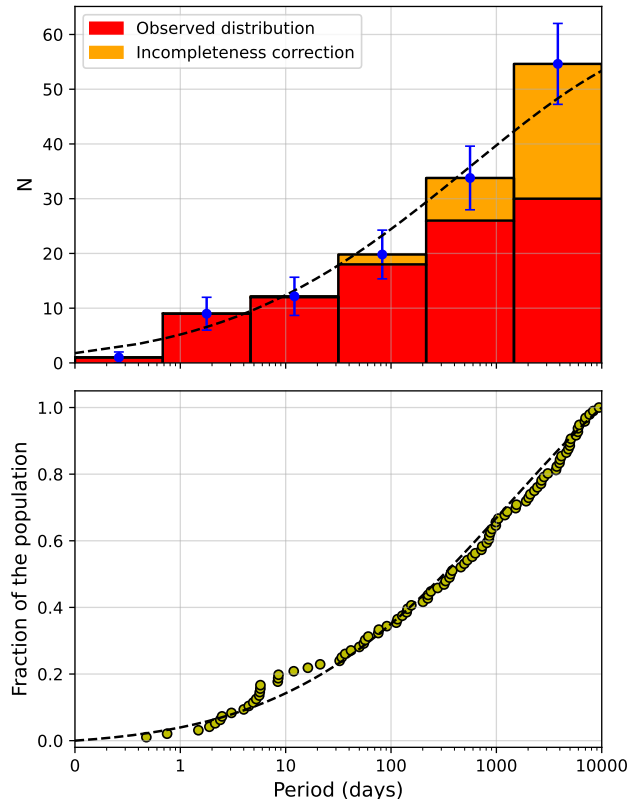


Figure 10. *Top:* Distribution of orbital periods for the 96 binary members of the Hyades cluster with $P \leq 10^4$ d. The optimal number of bins was determined following the Freedman-Diaconis rule. Error bars on the corrected distribution are from counting statistics, and the dashed line is the log-normal distribution for solar-type binaries in the field, from the work of Raghavan et al. (2010). *Bottom:* Cumulative distribution function of observed periods, compared against the same field distribution as above (dashed line; see the text).

though as mentioned earlier, it does not appear to be statistically significant.

11.2. The Eccentricity Distribution

Figure 11 presents the distribution of eccentricities for the 78 binaries with periods between the tidal circularization period ($P_{\text{circ}} = 5.9$ d; Section 11.4) and 10^4 days, out of the 96 systems considered in the previous subsection. Here we have also excluded the two giants in the Hyades with known orbits (vB 41, vB 71), as stronger tidal forces due to their much more extended structures may have affected their eccentricities differently than the dwarfs.

The top portion of each bin in the histogram represents the correction for incompleteness, derived in the same way as explained for the periods. We have indicated with a dashed line the eccentricity distribution for field binaries, which Geller & Mathieu (2012) have shown is well approximated by a Gaussian with a mean of 0.39 and a standard deviation of 0.31. This is the same distribution adopted for our incompleteness corrections in Section 9. The cumulative distribution function of eccentricities is shown in the bottom panel, where the dashed line represents the field distribution with the same incompleteness as the binaries in our sample. There is very close agreement between this model and the observed distribution:

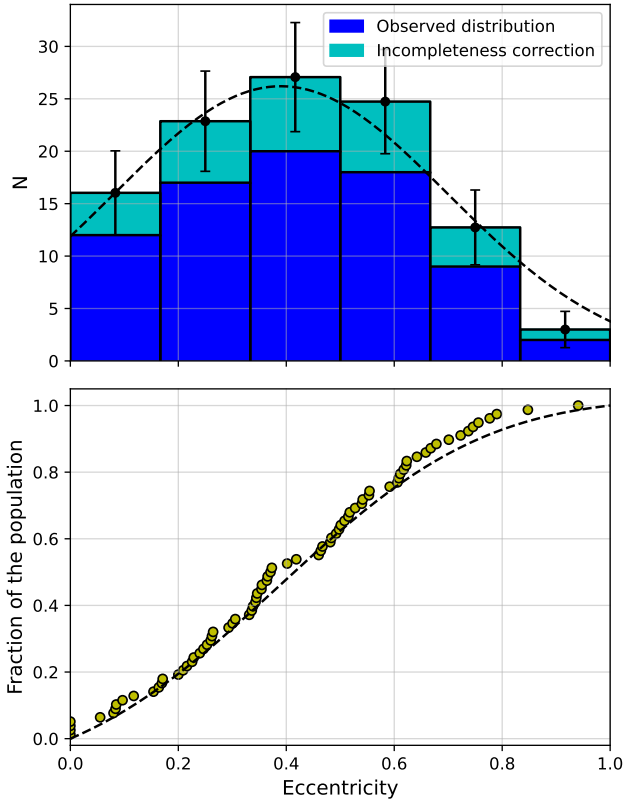


Figure 11. *Top:* Distribution of orbital eccentricities for the 78 binary members of the Hyades cluster with periods $P_{\text{circ}} \leq P \leq 10^4$ d, including triples and quadruples, and excluding the two giants with known spectroscopic orbits. Error bars on the corrected distribution are from counting statistics, and the dashed line is the Gaussian model for solar-type binaries in the field, from the work of Geller & Mathieu (2012). *Bottom:* Cumulative distribution function (see the text).

the Anderson-Darling test returns a p value of 0.68.

11.3. The Mass Ratio Distribution

The mass ratios measured directly for the SB2s in our sample ($q \equiv M_2/M_1 = K_1/K_2$) were supplemented here with mass information from the SB1s, which comes only in the form of the spectroscopic mass function, $f(M) = M_2^3 \sin^3 i / (M_1 + M_2)^2 = (P/2\pi G)(1 - e^2)^{3/2} K_1^3$. Inferring a mass ratio from $f(M)$ requires knowledge of the primary mass and the inclination angle. While statistical inversion methods may be applied to convert the distribution of $f(M)$ into one of q if rough estimates of M_1 are available (see, e.g., Lucy & Ricco 1979; Mazeh & Goldberg 1992; Shahaf et al. 2017, and references therein), here we have chosen to proceed differently and follow the methodology of Torres et al. (2021). This uses the fact that in a cluster such as the Hyades, with a known age and metallicity, it is possible to obtain sufficiently accurate values for both M_1 and M_2 , and therefore q , by using a model isochrone to deconvolve the brightness measurements for the combined light of each binary, constrained by the measured values of $f(M)$, or equivalently, by the minimum secondary mass, $M_2 \sin i = (P/2\pi G)^{2/3} \sqrt{1 - e^2} K_1 (M_1 + M_2)^{2/3}$. The model isochrone we used is from the PARSEC v1.2S series (Chen et al. 2014), with color corrections as de-

termined by Wang et al. (2025). Accurate parallaxes are also required, and the photometry must be free from contamination by other nearby sources.

In addition to the Gaia DR3 photometry (G , G_{BP} , G_{RP}) that is available for all our SB1s, we also used the 2MASS JHK_S magnitudes (Cutri et al. 2003), as these near-infrared measurements are more sensitive to the low-mass companions that many of these binaries have. Complete details on the methodology to infer the mass ratios and their uncertainties may be found in the paper by Torres et al. (2021). The determination of q for each SB1 was repeated 100 times, propagating the uncertainties in the photometry and in $M_2 \sin i$ in a Monte Carlo fashion.

Initial determinations revealed poor photometric fits for some of the binaries, which we traced to inaccurate Gaia parallaxes, most likely a result of biases from the very binary nature of the objects. We found much improved fits by replacing the trigonometric parallaxes for all objects with their “kinematic” parallaxes (moving cluster method), derived using the Gaia proper motions and the assumption that all Hyades members share a common motion in space. The space motion vector and convergent point coordinates were adopted also from the Gaia mission itself (Gaia Collaboration et al. 2018). In a few cases for which Gaia DR3 did not report a proper motion, we used highly precise values from Altmann et al. (2017), which are based on positions from an earlier data release by the Gaia mission (DR1) combined with positions from ground-based catalogs going back decades. This tends to average out the orbital motion in most cases, yielding more accurate proper motions.

For our study of the mass ratio distribution we have included triple and quadruple systems in which the mass ratios for the outer subsystems are also known. In these cases, we have added up the masses of the inner components and considered them as a single object for the purpose of computing the mass ratio involving the outer component. This assumes that these mass ratios in the outer orbits of triple and quadruple systems are drawn from the same population as those of binary systems.

Among the 96 member systems in our sample (V471 Tau excluded) with known inner or outer orbits and periods under 10^4 d, 54 are SB1s, 39 are SB2s (including triples and quadruples; see above), and another 3 have only astrometric orbits from Gaia or the WDS (HAN 291, vB 123, vB 122). These last three provide no useful dynamical mass information for our purposes,⁷ and were excluded. Two of the SB1s are in triple systems with known outer orbits (vB 22, vB 102; see Table 9). For the first, in which the inner pair is an eclipsing binary with known absolute masses, astrometric observations have allowed us to determine the mass of the tertiary, and therefore the mass ratio in the outer orbit (see Appendix A). For the other, the detectable wobble of the inner pair on the plane of the sky allowed Tokovinin (2021c) to derive the mass ratio for the inner binary. We have added these two systems to the 39 with directly measured values of q .

On the other hand, not all 52 of the remaining SB1s are

⁷ The orbits for HAN 291 and vB 123, reported by Gaia, only pertain to the motion of the photocenter, and vB 122 has no parallax or proper motion in the Gaia DR3 catalog.

suitable for the purpose of this section. We removed 6 of these objects for a variety of reasons. Three of the ones with long periods (vB 91, vB 271, HAN 432) have components of similar brightness ($\Delta m \lesssim 1$ mag), and suffer from severe blending of the spectral lines such that the velocities could only be measured from the blend, as if it were a single object. In these cases, the mass functions are unreliable because the velocity semiamplitudes will always be underestimated. Another object (vB 190) lacks a parallax and a proper motion from Gaia. Our attempt to use proper motions from an alternate source to infer its kinematic parallax resulted in a large mass ratio (~ 0.8), inconsistent with the fact that the companion is 5.5 mag fainter than the primary. Two additional systems (vB 9, vB 41) were removed for giving very poor fits to the photometry. The remaining $52 - 6 = 46$ SB1s were analyzed together with the 41 SB2s.

Our procedure for inferring mass ratios for the SB1s generates a distribution of 100 estimates of q for each binary. The median values for each system are plotted in histogram form in the top panel of Figure 12 (bottom section of each bin). Incompleteness corrections were computed for each of those 100 estimates, and the median values of those corrections for each binary are shown in the top portion of each bin. As expected, the distribution with incompleteness corrections included rises toward small mass ratios, as such systems are increasingly harder to detect spectroscopically.

The second panel of Figure 12 displays the distribution of mass ratios for the SB2s. In this case, it is unclear whether incompleteness corrections should be applied because these systems are often recognized as double-lined early-on in the observations, and are typically then followed up more frequently until a publishable orbital solution has been obtained. We show the distribution without any adjustments. The preference for equal-mass systems reflects the fact that components of similar mass also have similar brightness, making the secondaries easier to detect and measure.

The third panel adds together the distributions for the SB1s and SB2s. There is perhaps a slight rise toward equal-mass systems, although the Anderson-Darling test indicates no significant difference compared to a flat distribution (p value = 0.48), which we show with a dashed line in the figure. The bottom panel presents the cumulative probability distribution of observed mass ratios, with the flat model adjusted for incompleteness.

Returning to the three systems with blended lines that were excluded above, the relatively bright secondaries in all three cases imply that the mass ratios must be quite large. As an experiment to see how their exclusion might influence the results, we added them to the sample with randomly chosen q values larger than 0.9, which places them in the rightmost bin of the SB1+SB2 histogram. We then repeated the Anderson-Darling test to compare against a flat distribution. Although adding these three binaries tends to reinforce the visual impression of an increase in the frequency toward large mass ratios, the p value we obtain is still large (0.19), indicating no meaningful distinction between the two distributions.

Finally, for the benefit of the reader, we collected in Table 12 the properties of the binary and multiple systems used for the study of the distributions of mass ratios, periods, and eccentricities in this section and in the

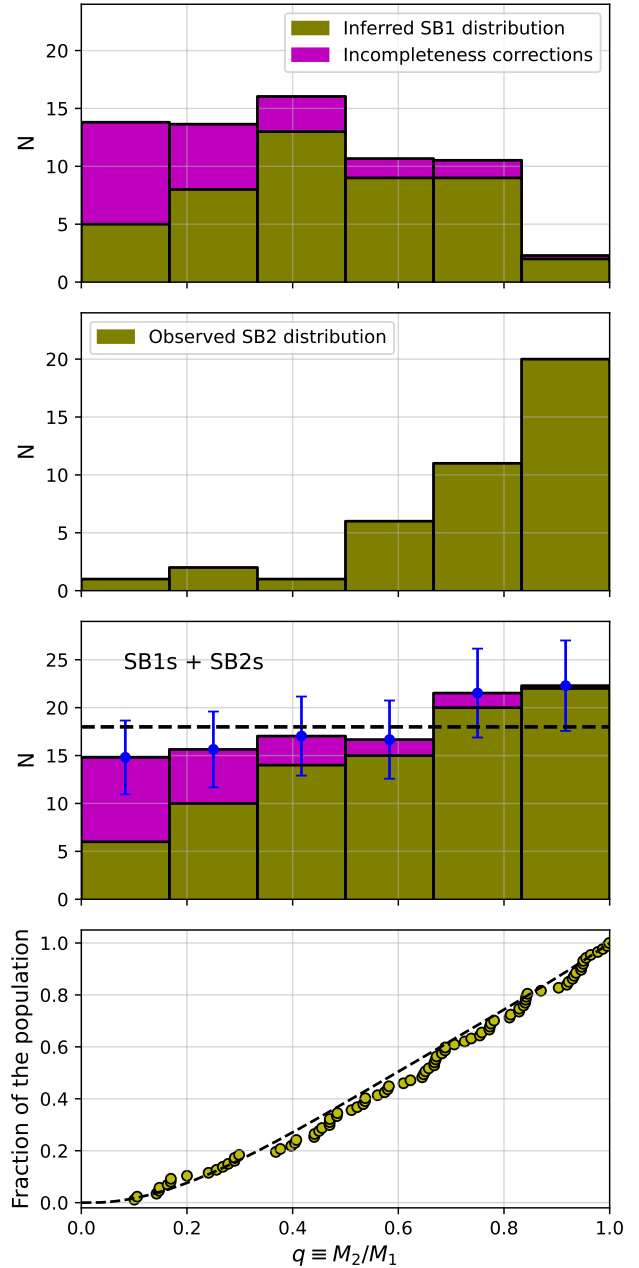


Figure 12. Distribution of mass ratios in the Hyades cluster, from 87 binary and multiple systems. From top to bottom, the panels show the inferred distribution for single-lined systems, the observed distribution for double-lined systems, the sum, and finally the cumulative distribution (see the text). Incompleteness corrections are indicated in the first and third panels. Error bars on the corrected distribution for SB1s+SB2s are from counting statistics, and the dashed line (shown also in the bottom panel) corresponds to a flat distribution.

previous two. In addition to P , e , q , and M_1 for each system, we list the correction factors applied to account for incompleteness. The table has 96 entries, which is the number of systems used for the period distribution. Not all were used for the eccentricity and mass ratio statistics, as explained earlier.

Table 12
Material Used for Binary Statistics.

#	Name	P (d)	e	q	M_1 (M_\odot)	$C(P)$	$C(e)$	$C(q)$
14	HD 17922	318.8792	0.3361	0.441	1.186	1.216	1.349	1.224
48	LP 413-18	16.2493	0.5009	0.671	0.540	1.029	1.362	1.181
49	LP 413-19	0.4761	0.0000	0.950	0.449	1.000	...	1.059
68	LP 357-4	1523.8262	0.4924	0.829	0.411	1.479	1.361	1.152
103	vB 8	855.8604	0.3733	0.377	1.429	1.358	1.351	1.283

Note. — Primary masses (M_1) were estimated using photometry from Gaia, and the isochrone for the Hyades employed in this work. The mass ratios were estimated as described in this section. For the triple systems (vB 22, HAN 346, vB 304), which have two entries each, M_1 in the second entry is the total mass of the “primary” in the outer orbit. For the hierarchical quadruple system vB 124, which also has two entries, the mass ratios pertain to each of the inner binaries. The last three columns contain the correction factors applied to account for incompleteness in the distributions of P , e , and q . Empty fields in the q column indicate the system was not used to generate the corresponding distribution, for reasons explained in the text. In those cases, the $C(q)$ column is also empty. Systems with no $C(e)$ value are either giants (vB 41, vB 71) or ones with $P < P_{\text{circ}}$, which were excluded from the eccentricity distribution. (This table is available in its entirety in machine-readable form.)

11.4. Tidal Circularization: the e -log P Diagram

The empirical property that the shortest-period spectroscopic binaries tend to have circular orbits was recognized by observers more than a century ago (see, e.g., Campbell 1910; Ludendorff 1910; Schlesinger & Baker 1910), even if the physical reason appeared somewhat mysterious at the time. It is now well understood that this is caused by tidal forces, with their strong dependence on the orbital separation (inverse cube relation), and additional dependence on the stellar radii and masses. However, there is still considerable debate about the efficiency of the different tidal mechanisms that have been proposed. Tidal forces result in the dissipation of orbital energy through friction, with gradual reduction of the eccentricity and period over time. The effect is easily seen in the familiar eccentricity-log period (e -log P) diagram, in which most binaries tend to be circular up to a certain period, beyond which there is a rise toward higher eccentricities with a broad distribution of values. This transition period has been postulated to depend on stellar age (e.g., Mathieu & Mazeh 1988; Latham 1992; Mathieu et al. 2004; Mazeh 2008), and these works and others published since have presented evidence to that effect from studies of several coeval populations of solar-type binaries. Those data sets have included pre-main-sequence (PMS) objects, several open clusters, field binaries in the solar neighborhood, and a sample of older halo binaries (Meibom & Mathieu 2005; Meibom et al. 2006; Geller & Mathieu 2012; Milliman et al. 2014; Leiner et al. 2015; Nine et al. 2020; Geller et al. 2021).

Meibom & Mathieu (2005) introduced a robust way of measuring this transition or “circularization” period, P_{circ} , and used it to make determinations for several of the samples of coeval binaries mentioned above (see their Figure 9, which has been updated more recently by Nine et al. 2020 and by Zanazzi 2022). One of the Meibom & Mathieu (2005) data sets combined 21 systems in the Hyades with a slightly larger number of binaries in Praesepe, which is of similar age. They discussed all of these determinations in the context of the two leading tidal mechanisms: the equilibrium tide, operating in stars with convective envelopes (Zahn 1966, 1977, 1989), and the dynamical tide, acting in hot stars

with radiative envelopes (Zahn 1975, 1977; Goodman & Dickson 1998; Terquem et al. 1998; North & Zahn 2003). They found that the measurements are not consistent with the predictions by Zahn & Bouchet (1989), who proposed that essentially all of the circularization should occur during the pre-main-sequence phase, when stars have larger sizes and deeper convective envelopes. For binaries with typical initial eccentricities near 0.3, Zahn & Bouchet (1989) expected the “cutoff” period separating circular from eccentric binaries to be between about 7.2 and 8.5 days, depending somewhat on the masses and initial conditions. However, while the younger samples from Meibom & Mathieu (2005) (PMS binaries, the Pleiades, M35) were consistent with those expectations, the older ones (M67, NGC 188, field binaries, and halo binaries) had even longer P_{circ} values, suggesting that tidal forces continue to act during the main-sequence phase, reducing the eccentricities even further. Notably, the Hyades + Praesepe sample was an outlier, with a P_{circ} value they estimated to be 3.2 ± 1.2 d, or less than half of that expected.

An early version of the e -log P diagram for the Hyades alone, based on 46 systems (including triples), was presented by Stefanik & Latham (1992), who remarked that the transition period was somewhat uncertain, and may be between 5.75 and 8.50 d, based on the binaries with the first eccentric and last circular orbits. An update was shown by Griffin (2012) (see their Figure 69), although without any discussion other than the mention of a few objects of interest at the short period end. The 64 systems they displayed also included the outer orbits of several triples known at the time. The present work offers an opportunity to revisit the determination of P_{circ} with a larger and cleaner sample, now including much improved knowledge about higher-order multiplicity. Our sample features several new binaries in the critical period range (< 10 days): LP 413-19 (0.47 d), vB 34 (3.06 d), HD 283810 (4.92 d), and HD 36525 (5.68 d). Our goal in this section is to include, to the extent possible, only unevolved main-sequence systems that have not suffered changes in their eccentricity due to internal dynamics. Therefore, in addition to excluding the triples and quadruples with known orbits, and other systems mentioned at the beginning of Section 11, we have removed

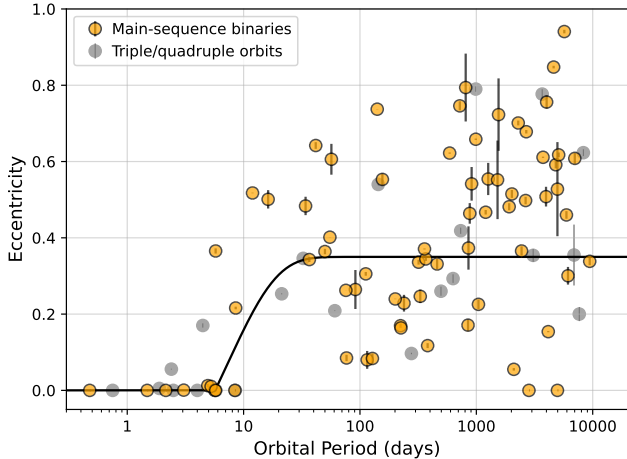


Figure 13. Eccentricity vs. period diagram for our sample of 72 binary members in the Hyades. The curve represents our fit to the circularization function of Meibom & Mathieu (2005), giving $P_{\text{circ}} = 5.9$ d. The gray symbols represent 22 additional inner and outer orbits of triple and quadruple systems, which were not used to determine the circularization period.

the two giants that have spectroscopic orbits (vB 41 and vB 71).

The data for the remaining 72 binary members with periods up to 10^4 d were used to determine P_{circ} using the formalism of Meibom & Mathieu (2005), for consistency with the earlier studies of other coeval populations. We obtained $P_{\text{circ}} = 5.9 \pm 1.1$ d, where the uncertainty is statistical only.⁸ This is longer than the value of 3.2 d reported by Meibom & Mathieu (2005), but is still well below the predictions by Zahn & Bouchet (1989). The e - $\log P$ diagram for the Hyades is shown in Figure 13.

The spectral types for our Hyades binaries range between A and M, based on our spectroscopic temperatures, whereas the previously reported coeval samples used to estimate P_{circ} have been described loosely as consisting of binaries with solar type primaries (FGK), although some of the samples extend beyond that range. As before, this corresponds approximately to $T_{\text{eff}} = 4000$ – 7000 K, or masses of ~ 0.7 – $1.5 M_{\odot}$. On the other hand, the tidal theory of Zahn & Bouchet (1989) focused on masses in the range 0.5 – $1.25 M_{\odot}$. We find that if we restrict the temperatures in our sample to correspond to the range 0.7 – $1.5 M_{\odot}$ (49 binaries) or to 0.5 – $1.25 M_{\odot}$ (~ 3500 – 6300 K, 55 binaries), the result for P_{circ} in both cases is only slightly shorter: 4.9 ± 1.3 d.

Recent studies of tidal circularization in binaries have cast doubt on the long-held belief that the circularization period depends primarily on the age of the population being considered. This perception that age is the dominant factor has been driven largely by the findings of Meibom & Mathieu (2005), and others, that binaries in older samples such as M67 or the halo are circularized out to much longer periods than younger ones. In a recent investigation based on several hundred eclipsing binaries from the Kepler and TESS missions, Zanazzi (2022) agreed with

⁸ The true uncertainty in the circularization period is difficult to quantify, as it is likely dominated by the finite size of our sample, rather than errors in the eccentricity measurements. Furthermore, the value of P_{circ} can be sensitive to the properties of just one or two systems at critical locations in the e - $\log P$ diagram (see below).

earlier authors that there is indeed a statistically significant difference between the eccentricity distributions of young and old binaries (see also Penev & Schussler 2022; Narayan et al. 2026). A different interpretation was put forward by Bashi et al. (2023) and IJspeert et al. (2024), who analyzed even larger samples of binaries from Gaia and from TESS, respectively. They concluded that P_{circ} depends primarily on the effective temperature, rather than on age, although the two properties are of course statistically correlated. Their hotter binaries displayed shorter circularization periods than the cooler ones.

As a test, we divided our Hyades sample in half by temperature, and determined the circularization period in each subset. We obtained P_{circ} values of 5.9 ± 1.5 d for the hotter half and 6.0 ± 1.5 d for the cooler half. Within the uncertainties there is no difference, although admittedly our samples here are very small.

It is worth reiterating that inferring a circularization period from relatively small samples of just a few dozen binaries, as has been the case for most previous studies in clusters, is fraught with uncertainty stemming in part from the irregular distribution of orbital periods, over which there is no control, and possibly also the methodology used. Limitations from the finite sample sizes have previously been pointed out, e.g., by Zanazzi (2022). On the other hand, the one parameter we can control perfectly in the case of the Hyades is the age. Field samples, such as those analyzed in the larger studies above, are less homogeneous as they must rely instead on age estimates that are necessarily less precise, and are subject to various observational uncertainties, including a lack of information on multiplicity, or imperfect knowledge of the stellar parameters or of interstellar reddening.

To further illustrate the dependence of P_{circ} on the distribution of orbital periods, and its sensitivity to the location of just one or two systems in the e - $\log P$ diagram, we point out that our result above (5.9 d) changes significantly if we remove two binaries with relatively short periods that stand out for their large eccentricities: vB 121 ($P = 5.75$ d, $e = 0.37$) and vB 62 ($P = 8.55$, $e = 0.22$). Without these two systems, we obtain $P_{\text{circ}} = 8.6$ d, which would then become consistent with the predictions of Zahn & Bouchet (1989). The primary of vB 121 is a late F star, for which we find no evidence of additional components that might be perturbing the eccentricity, in either the WDS or Gaia DR3 catalogs, or from our own spectroscopy. vB 62 has the same spectral type, and in this case there is a distant and faint tertiary companion ($\rho \approx 11''$, $\Delta G \approx 8$) that appears to be physically associated, according to information in the Gaia DR3 catalog. It is therefore possible, in principle, that the inner eccentricity is being pumped up by the third star (e.g., Mazeh 1990). However, we estimate the modulation timescale for this to be on the order of 2×10^{10} yr (see, e.g., Rappaport et al. 2013), and this is long enough that the effect on the eccentricity of vB 62 since birth is expected to have been minimal.

Thus, there is currently no reason to exclude these two systems from our estimate of P_{circ} , and it is possible that both started out with an exceptionally large eccentricity, and have not yet had time to circularize.

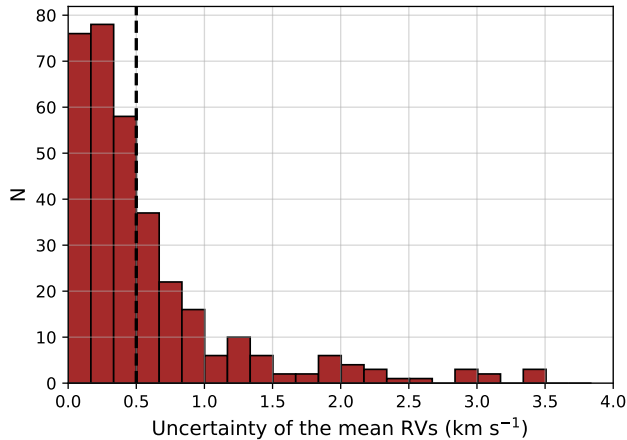


Figure 14. Distribution of the uncertainties of the mean RVs for the cluster members in our sample with $N_{\text{obs}} \geq 3$. Our determination of the cluster velocity dispersion is based on stars with errors under 0.5 km s^{-1} (dashed line).

12. THE RV DISPERSION IN THE HYADES

In Section 7 we used an estimate from Gaia of the internal velocity dispersion of the Hyades in the radial direction, to assist in establishing membership. Here we employ our own RV measurements to obtain an independent estimate of $\sigma_{\text{cl,RV}}$, which we will show is somewhat smaller. We began by removing from the mean RV of each star the large geometric effect coming from the range in viewing perspectives from one side of the cluster to the other, which can change the velocities by about $\pm 10 \text{ km s}^{-1}$ relative to a location at the cluster center. As in Section 7, we relied for this on the convergent point coordinates and the cluster space velocity vector from the Gaia mission. We refer to the differences between the measured mean RVs and these calculated (“astrometric”) RVs as ΔRV .

Hotter and rapidly rotating stars, as well as our fainter targets, tend to have much larger RV uncertainties that would unduly inflate our estimate of the velocity dispersion. Therefore, we chose to restrict the sample to stars (or multiple systems) with the most precise mean velocities. Figure 14 displays the histogram of the uncertainties of the mean velocities for the 339 member stars with at least three RV measurements. We adopted a cutoff of 0.5 km s^{-1} , marked in the figure with a dashed line. In the following we will focus our attention on the main-sequence FGK stars in our survey (T_{eff} approximately 4000–7000 K), which dominate the population.

The standard deviation of the 184 ΔRV values for the FGK stars with the best mean RVs is $0.79 \pm 0.04 \text{ km s}^{-1}$. However, this overestimates the velocity dispersion for several reasons. Unrecognized binaries, as well as any unrecognized non-members that remain in the sample, will tend to increase the dispersion. Even when their presence is known, visual companions, with their orbital periods much longer than the duration of our survey, can affect the RV of a target at a low level, shifting it away from the value expected if it were a single star. Because the Hyades cluster is so well studied, a sizable fraction of our targets have such close visual companions listed either in the WDS or Gaia catalogs (see Table 2), and these are likely to corrupt our estimate of $\sigma_{\text{cl,RV}}$. We identified

and removed 41 cases, after which the standard deviation was reduced to $0.53 \pm 0.03 \text{ km s}^{-1}$. Furthermore, out of concern that there may be a few non-members among the stars we classified as possible members, we chose to remove 8 of those objects with less secure membership credentials. With this, the dispersion became $0.44 \pm 0.03 \text{ km s}^{-1}$. Measurement errors in the velocities will also inflate the dispersion. We corrected for this effect following McNamara & Sekiguchi (1986), and obtained a further reduced dispersion of $0.34 \pm 0.04 \text{ km s}^{-1}$ from 135 stars.

It is important to note that while the astrometric RVs represent the true line-of-sight motion of the center of mass of a star, this is generally not the case for our measured RVs. As explained in Section 4, our velocity zero-point was established using asteroid observations, which represent reflected sunlight. Because of this, all our measured RVs have the gravitational redshift (GR) and convective blueshift (CB) of the Sun removed. Velocities we measure for a solar-type star should accurately be on the IAU system, but those for any other type of star will not. There will be a small offset equal to the difference between the star’s GR and CB relative to those of the Sun, and this will lead to an overestimate of the internal dispersion.

Figure 15 shows the expected difference between the GR of a star in the Hyades and the value for the Sun (0.63 km s^{-1}). The curve is based on masses and radii read from the same PARSEC v1.2S isochrone used previously. For FGK stars on the main sequence ($T_{\text{eff}} \approx 4000\text{--}7000 \text{ K}$), the offset can be up to about 0.1 km s^{-1} in the positive direction, and less in the negative direction. It becomes larger in the negative direction as stars approach the turnoff and proceed to the giant branch. CBs have a stronger dependence on temperature. We show that relation in the same figure, in which the curve was derived from Figure 3 of the work by Meunier et al. (2017), based on measurements for F7–K4 dwarfs, after subtracting the value for the Sun (-0.34 km s^{-1}). The dashed line in Figure 15 adds the two contributions together.

Examination of our ΔRV values reveals a clear dependence on temperature, in the same direction as predicted above. Separating our measurements into three temperature bins containing the majority of our targets (4000–5000 K, 5000–6000 K, 6000–7000 K), we find average ΔRV values of $+0.313 \pm 0.058 \text{ km s}^{-1}$, $+0.144 \pm 0.050 \text{ km s}^{-1}$, and $-0.104 \pm 0.088 \text{ km s}^{-1}$, respectively. These averages are represented in Figure 15 with filled squares, and are seen to be fairly consistent with expected trend shown by the dashed line (GR + CB). Intermediate temperature bins overlapping by half with the previous three (4500–5500 K, 5500–6500 K; open squares) suggest that the average ΔRV varies in a continuous fashion.

The smaller magnitude of the CB expected for K giants, as determined by Liebing et al. (2023), is shown by the magenta line in Figure 15. The dashed line at the top of the figure combines this effect with the GR for giants relative to the Sun, over the same temperature range. The average of our measured ΔRV values for the four giants in the Hyades is indicated with the cyan square, and again matches the prediction.

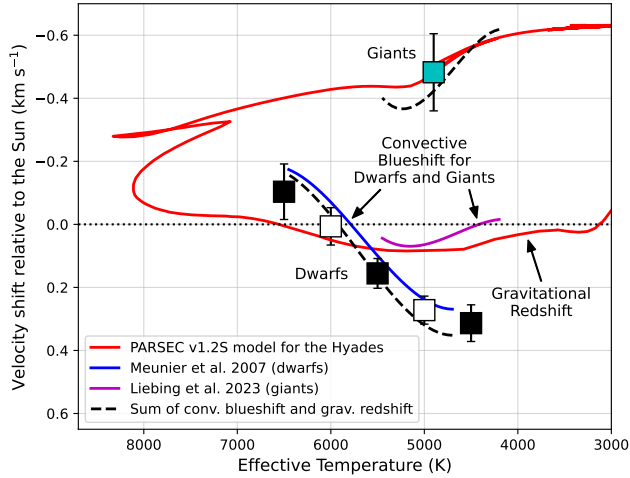


Figure 15. Magnitude of the GR and CB affecting the RVs of stars in the Hyades, relative to those effects in the Sun. The red curve for the GR is based on the same PARSEC v1.2S model isochrone used earlier in this work. The temperature dependence of the CB relative to the Sun is from empirical determinations by other authors, and is represented by a blue curve for FGK dwarfs (Meunier et al. 2017) and a magenta curve for giants (Liebinger et al. 2023). The dashed lines correspond to the combination of the two effects, separately for dwarfs and giants. Filled black squares mark the average ΔRV (measured RVs minus astrometric RVs) for stars in three separate 1000 K temperature bins (see the text). Open squares are shown for non-independent 1000 K bins overlapping with the previous ones.

We used a simple linear fit to the observed trend in ΔRV to subtract out the GR and CB effects from the individual values for the FGK dwarfs in our sample, and recalculated the internal RV dispersion of the cluster. Our estimate then becomes $\sigma_{cl,RV} = 0.31 \pm 0.04 \text{ km s}^{-1}$, which is somewhat smaller than the result from the Gaia mission used in Section 7 (0.40 km s^{-1}).

Numerous other empirical estimates of the velocity dispersion of the Hyades in one dimension have been reported, based either on RVs, on proper motions, or a combination of both. They have generally assumed that the dispersion is isotropic, at least in the central part of the cluster, which most authors consider to be the case. These determinations have typically ranged from about 0.3 to 0.7 km s^{-1} (Schwan 1990; Perryman et al. 1998; Lindegren et al. 2000; Madsen 2003; Röser et al. 2011; Reino et al. 2018; Leão et al. 2019; Oh & Evans 2020; Evans & Oh 2022). Smaller estimates around 0.2 km s^{-1} have been obtained through modeling of the light or mass density distribution, by adopting a Plummer potential or similar, along with some estimate for the total mass and for the tidal or core radius of the cluster (e.g., Gunn et al. 1988; Perryman et al. 1998; Oh & Evans 2020). In the next section we will show that our own estimate of the overall cluster dispersion, $\sigma_{cl,RV}$, may still be overestimated, and that it appears to be significantly smaller in the inner regions of the Hyades.

In other clusters, the observed internal velocity dispersion has been used to determine the total mass through the virial theorem, on the assumption of dynamical equilibrium (e.g., Geller et al. 2015; Torres et al. 2021). If applied to the Hyades, with values for the half-mass radius of 4.1 pc (Röser et al. 2011) or 5.75 pc (Evans & Oh 2022), the result is $M_{tot} \sim 700\text{--}1000 M_{\odot}$, about a

factor of 2 larger than most other estimates. The reason is that the Hyades cluster is not in virial equilibrium, as has been noted by many authors, but rather, is in a state of dissolution and near the end of its life. It has long been known to display mass segregation (e.g., Reid 1992; Perryman et al. 1998; Röser et al. 2011; Evans & Oh 2022), and has already lost a significant fraction of its lighter stars through evaporation or tidal stripping in the Galactic field. By some estimates, as much as 60% of the original mass of the cluster has already been stripped away (e.g., Röser et al. 2011; Lodieu et al. 2019; Oh & Evans 2020). Many of the escaped stars have ended up in the prominent tidal tails of the Hyades, which extend for several hundred parsecs on either side in the direction of Galactic rotation (Röser et al. 2011; Jerabkova et al. 2021).

13. CLUSTER ROTATION OR SHEAR – IMPACT ON $\sigma_{CL,RV}$

In all likelihood, the natal molecular cloud from which the Hyades emerged had some angular momentum to begin with, and it would not be surprising to see that property reflected in the motion of stars in the present-day cluster. The possibility of rotation in the Hyades has been examined for at least six decades (Wayman et al. 1965), although the results have been mixed. Gunn et al. (1988) used proper motions and RVs, but were unable to confirm rotation at a significant level. Negative results were also obtained by others (Perryman et al. 1998; Lindegren et al. 2000; Vereshchagin et al. 2013; Reino et al. 2018). On the other hand, Leão et al. (2019) presented what they interpreted as a significant signature of rotation by examining the ΔRV differences between the RVs from high-resolution ground-based spectroscopy and the corresponding astrometric velocities based on Gaia DR2, for a sample of 56 stars. They reported a statistically significant correlation between ΔRV and the right ascension of their stars (their Figure 3), with a slope of $0.0340 \pm 0.0032 \text{ km s}^{-1}$ per degree. Other possible explanations for this trend, such as an inaccurate space velocity vector, or cluster expansion, were tested and ruled out.

Inspired by this result, we examined our own ΔRV values from the previous section, which, as explained above, include an additional correction compared to those of Leão et al. (2019) to remove the effects of GR and CB. We have also gone to greater lengths to exclude triple systems with unknown spectroscopic orbits, which may bias the RVs. Figure 16 shows the run of ΔRV versus right ascension, revealing a similar trend as found by Leão et al. (2019), only with a smaller but still statistically significant slope of $0.0228 \pm 0.0017 \text{ km s}^{-1}$ per degree.

A more sophisticated analysis of the Gaia DR2 proper motions and RVs was carried out by Oh & Evans (2020). Their model allowed for rotation, shear, expansion or contraction, as well as for an anisotropic velocity dispersion. Their results revealed only mild anisotropy in the velocity field except in the tails, but more importantly, no significant rotation. Instead, they measured significant azimuthal and radial shear in the Galactic frame, and indicated that any rotation of the magnitude claimed by Leão et al. (2019) would have been easily detected in their analysis. In view of this, they expressed the opinion that the Leão et al. (2019) result is a consequence of shear rather than rotation.

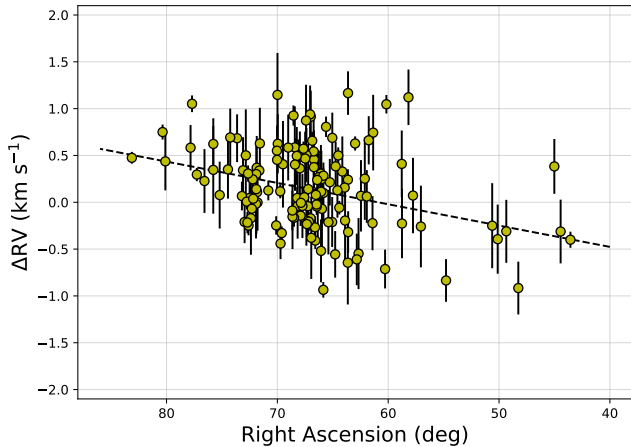


Figure 16. ΔRV values (difference between the measured spectroscopic RVs and the astrometric RVs, with GR and CB removed) shown as a function of right ascension for 135 stars in the Hyades. The dashed line is a least-squares fit, giving a slope of $0.0228 \pm 0.0017 \text{ km s}^{-1} \text{ per degree}$. The Pearson correlation coefficient is 0.35 ($p \text{ value} = 3 \times 10^{-5}$). For the interpretation of this trend, see the text.

More recently, Hao et al. (2024) carried out an independent analysis based on data from Gaia DR3, and reported a statistically significant measure of rotation of $0.09 \pm 0.03 \text{ km s}^{-1}$ within the tidal radius of the Hyades, which they assumed to be 9 pc. Jadhav et al. (2024), however, found no rotation, despite also using Gaia DR3 data. Finally, in another Gaia DR3 study, Olivares et al. (2025) concluded that the cluster does display a modest degree of rotation with a rate of $0.0321 \pm 0.0110 \text{ km s}^{-1} \text{ pc}^{-1}$.

Whether the trend in Figure 16 is caused by rotation or by shear, it has a direct impact on the estimate of the internal velocity dispersion $\sigma_{\text{cl,RV}}$ that we reported previously. As stars farther from the cluster center dominate the correlation, we separated the sample into two groups by linear distance from the center and recomputed the dispersion in each half. In the inner region within about 5.5 pc (68 stars), where ΔRV shows no trend with distance, the dispersion corrected for GR, CB, and observational errors is $\sigma_{\text{cl,RV}} = 0.21 \pm 0.05 \text{ km s}^{-1}$. In the outer region it is $0.38 \pm 0.05 \text{ km s}^{-1}$, with about two thirds of those 67 stars lying beyond the tidal radius of the cluster (~ 10 pc; Perryman et al. 1998; Röser et al. 2011), some possibly in the tails. Interestingly, the dispersion for the subset of stars closest to the center matches the smallest estimates inferred by others from steady-state dynamical modeling using a Plummer model (e.g., Gunn et al. 1988; Perryman et al. 1998; Oh & Evans 2020).

14. DISCUSSION AND CONCLUSIONS

This study marks the completion of the spectroscopic survey of the Hyades region conducted at the CfA over 45+ years. During that time, we collected $\sim 12,000$ spectra for 625 objects covering an area on the sky of nearly 4000 square degrees. Among the 343 cluster members and possible members in the sample, there are 90 systems with known spectroscopic orbits having periods shorter than 10^4 d. About three dozen other systems with known spectroscopic orbits are non-members, or are members with even longer periods. Several additional objects in our survey have astrometric orbits, generally also with longer periods. The precision and accuracy of our RV

measurements is high enough that the subtle effects of gravitational redshift and convective blueshift are clearly discernible in both the dwarfs and the giants.

As a result of this work, and that of others, we now have the most complete inventory of spectroscopic binaries in the cluster. The frequency of solar-type (FGK) spectroscopic binaries up to periods of 10^4 d is determined to be $40 \pm 5\%$, after a correction for incompleteness. This is only slightly higher than estimates for other open clusters, and considerably higher than measured for field samples (the solar neighborhood, and the halo), which collectively span two orders of magnitude in age.

Taking into account our sensitivity, we find that the distributions of both the orbital periods and the eccentricities for systems up to 10^4 d are consistent with those of solar-type binaries in the field. In particular, the shape of the eccentricity distribution in the Hyades is quite similar to that in other open clusters of very different ages, including the Pleiades, M67, and NGC 188 (Torres et al. 2021; Geller et al. 2021), although for M67 and NGC 188 the distributions are also formally consistent with being uniform. The eccentricity distribution in the Hyades resembles the Rayleigh distribution found by Wu et al. (2025) from a large sample of main-sequence binaries from Gaia DR3, even though that sample is a mixture of objects of unknown ages, compositions, and origins. As suggested by Wu et al. (2025), this type of distribution is most likely primordial, and may reflect a universal process. As examples of this process, they proposed excitation by the circumbinary disks, or ejection of brown dwarfs that may have been part of the binary systems at birth.

The distribution of mass ratios provides useful constraints on theoretical models of binary star formation. Unlike the periods and eccentricities of binaries, the mass ratios are largely insensitive to dynamical evolution within a cluster. However, a survey of the literature reveals rather different results from one study to the next. In the Hyades, we find a distribution that is essentially flat, with only a hint of an upward trend with q . This is similar to what was found in the Pleiades (also flat). On the other hand, the distributions in M67, and especially NGC 188, show a rise toward small mass ratios (Geller et al. 2021). Similar bottom-heavy shapes for field samples have been found by Gullikson et al. (2016), Murphy et al. (2018), and others, with the distributions peaking at $q \sim 0.2\text{--}0.3$. On the other hand, an independent study of the Hyades by Albrow (2024), based on the location of stars above the main-sequence ridge line in the color-magnitude diagram of the cluster, found a distribution that rises toward mass ratios of unity. In the widely cited study by Raghavan et al. (2010), solar-type binaries in the field show a fairly flat mass ratio distribution between 0.2 and 0.95, much like the Hyades, but then display a significant enhancement for equal-mass (‘twin’) binaries. Moe & Di Stefano (2017) found a similar enhancement toward $q = 1$, with slight variations depending on the orbital period. We do not see such an excess of twin binaries in the Hyades. A sharp excess of mass ratios near unity was also found by El-Badry et al. (2019) in a large-scale study based on main-sequence binaries from Gaia DR2, although their results focused on much wider binaries than those considered here, with

separations larger than 50 au ($P \sim 10^5$ d) and up to 50,000 au.

We determine a tidal circularization period in the cluster of 5.9 ± 1.1 d, using the methodology of Meibom & Mathieu (2005). This is significantly longer than their estimate of 3.2 d. Tidal theory has yet to provide a coherent explanation for the results published previously from various coeval samples of binaries in clusters and in the field, which appear to suggest a dependence of P_{circ} on age. Part of the difficulty may be related to the empirical determination of P_{circ} itself, which is highly sensitive to the size of the sample and the distribution of orbital periods, or even the methodology used. The evolution of the eccentricity in a binary depends not only on the separation, but also on the primary mass as well as the nature of the secondary component (see, e.g., Mazeh 2008). The cluster samples referenced above are not completely homogeneous (and the field samples are even less so), such that there is likely to be some added scatter in the P_{circ} estimates due to these factors, beyond their statistical uncertainties.

An additional drawback for the determination of P_{circ} is the contamination of the binary sample by triple systems, as the tertiaries can influence the eccentricities of the inner pairs. While we have made an effort here to weed out such cases, especially among the shorter-period binaries that are the most critical, there will inevitably be triples that have escaped our detection, even in a nearby and well-studied cluster like the Hyades. It is difficult to quantify how this might impact P_{circ} , but the limitation must be kept in mind. To make things worse, binaries with short periods almost always seem to have tertiary components. Tokovinin et al. (2006) reported that the fraction of spectroscopic binaries with third components is as high as 96% for binaries with periods under 3 d, and still 34% for periods longer than 12 d. Similar results have been found by Laos et al. (2020). This appears to be a rather fundamental difficulty, as removing all triples from the sample, even if that were possible, would most likely preclude a determination of the circularization period.

Open clusters are known to be fragile structures. Unless they are very massive to begin with, most disintegrate after a few hundred million years through interactions with the Galactic environment (e.g., Friel 1995). At its age of about 700 Myr, the Hyades cluster has completed three revolutions around the Galactic center, and clearly shows signs of stress. It has already lost a substantial fraction of its members, and is gradually being torn apart in the Galactic field. It displays leading and trailing tidal tails with a total extent of almost 1 kpc (Jerabkova et al. 2021). The cluster is not in a state of dynamical equilibrium. In the central regions within about 5.5 pc (roughly the half-mass radius), we measure a line-of-sight velocity dispersion of 0.21 ± 0.05 km s $^{-1}$, close to what is expected on theoretical grounds (Gunn et al. 1988; Perryman et al. 1998; Röser et al. 2011). Farther out, the dispersion is larger: we obtain 0.38 ± 0.05 km s $^{-1}$ for the outer half of our sample, as the kinematics of the cluster become increasingly dominated by stars that are slowly drifting away. Studies of the dynamical evolution of the Hyades indicate that it is approaching the end of its life. The most dire predictions (e.g., Oh & Evans

Table 13
Orbital Parameters for LP 301-69

Parameter	Value	Prior
P_A (day)	5.418682 ± 0.000024	[5, 6]
$T_{\text{max},A}$ (BJD)	54154.9764 ± 0.0095	[54152, 54156]
K_{Aa} (km s $^{-1}$)	30.30 ± 0.26	[10, 50]
P_{AB} (day)	4810 ± 50	[2000, 6000]
$T_{\text{max},AB}$ (BJD)	56539 ± 47	[53000, 57500]
K_A (km s $^{-1}$)	7.67 ± 0.44	[1, 20]
γ (km s $^{-1}$)	$+20.33 \pm 0.29$	[0, 50]
f_{CfA}	0.90 ± 0.27	[-5, 5]
Derived Properties		
$a_{Aa} \sin i$ (10^6 km)	2.258 ± 0.019	...
$M_{Ab} \sin i / (M_{Aa} + M_{Ab})^{2/3}$	0.2499 ± 0.0022	...
$a_A \sin i$ (10^6 km)	507 ± 31	...
$M_B \sin i / (M_A + M_B)^{2/3}$	0.607 ± 0.035	...

Note. — The values listed correspond to the mode of the posterior distributions from our MCMC analysis, with uncertainties representing the 68.3% credible intervals. Times of maximum primary velocity are referred to BJD 2,400,000. f_{CfA} represents a multiplicative scale factor applied to the internal RV errors. Priors in square brackets in the last column are uniform over the ranges specified, except for the one for f_{CfA} , which is log-uniform.

2020) have it completely dissolving into the Galactic field within the next 30 Myr.

The full-sky astrometric and spectroscopic survey performed by Gaia, along with extensive and complementary RV monitoring from the ground, have provided valuable knowledge about the structure, kinematics, and dynamical evolution of the cluster, and about its composition, including binarity. Future data releases from the Gaia mission promise to increase that knowledge even further, adding to the importance of the Hyades as a valuable benchmark for stellar astrophysics.

APPENDIX A: ORBITAL SOLUTIONS FOR SPECIAL CASES

Here we describe our orbital solutions for more complex systems, including ones for which we incorporated astrometric measurements to strengthen or add value to the results from the RVs alone. The velocities for the single- and double-lined objects discussed below are listed in Tables 3 and 4 of the main text.

(101) LP 301-69

The 15 RV measurements we have of this object, which are listed in Table 3 of the main text, clearly indicate variability with a period of 5.4 d. The very large scatter we initially found from a single-lined orbital solution is due to a third star in the system with a period of about 13 yr and a near-circular orbit. The inner orbit appears to be circular as well. A simultaneous triple star solution was carried out in a Markov chain Monte Carlo (MCMC) framework, with both eccentricities set to zero, to reduce the number of free parameters. Light travel time corrections were applied to the times of observation in the inner orbit. The results are presented in Table 13. Figure 17 displays our model with the observations. The center-of-mass velocity of LP 301-69, as well as its Gaia parallax and proper motion, all rule out association with the Hyades. The large Gaia RUWE value of 4.309 is likely a reflection of the perturbation from the wide companion.

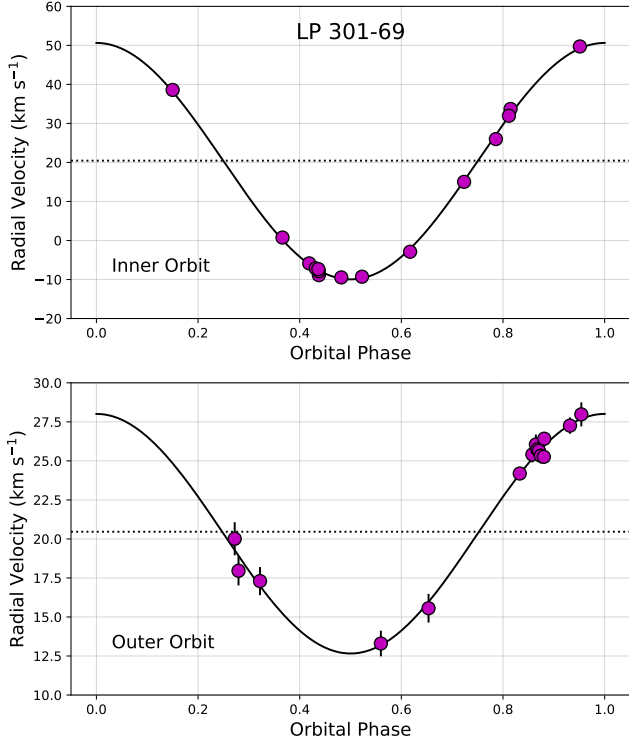


Figure 17. RV measurements for LP 301-69, together with our models for the inner and outer orbits. In each case, the motion in the other orbit has been subtracted for display purposes. The dotted line represents the center-of-mass velocity.

(145) HD 26090

This is a close visual binary (WDS 04089+2911, $\rho \sim 0''.3$) with a long orbital period and a fairly high eccentricity, in which the spectroscopic observations are concentrated mostly near periastron. The companion was discovered and first measured visually in 1891 (Burnham 1894). HD 26090 is double-lined. Additional RVs were obtained by Griffin (2001), and partially overlap in time with ours. The phase coverage provided by the RVs is limited, and the orbital period cannot be determined from the velocities alone. However, the astrometric measurements made since Burnham’s time complement the spectroscopy well, and enable the period to be better constrained. Several astrometric orbits have been reported in the literature, the most recent of which appears to be the one by Muller (1978). It gives a period of 60 yr, and is considered preliminary. Griffin adopted that period, and held it fixed to derive a preliminary spectroscopic orbital solution from his RV measurements obtained between 1986 and 2000.

The spectroscopic observations at the CfA began with the Digital Speedometers in 1983, and continued through 2006. Additional spectra of HD 26090 were obtained between 2012 and 2024 with the TRES instrument. The templates adopted for the TODCOR analysis had temperatures of 6000 and 5500 K, and $v \sin i$ values of 4 km s^{-1} for both components. The flux ratio we determined from the higher-quality TRES spectra is $\ell_2/\ell_1 = 0.419 \pm 0.028$, at the mean wavelength of our observations. The combined velocity coverage of the CfA material is a little over 40 yr, or about 2/3 of the binary orbit.

Table 14
Orbital Parameters for HD 26090

Parameter	Value	Prior
P (days)	23379 ± 390	[5000, 40000]
T_{peri} (BJD−2,400,000)	49873.2 ± 9.6	[35000, 55000]
a'' (")	0.2550 ± 0.0049	[0.1, 2.0]
$\sqrt{e} \cos \omega_1$	-0.6163 ± 0.0069	[−1, 1]
$\sqrt{e} \sin \omega_1$	-0.6143 ± 0.0078	[−1, 1]
$\cos i$	$+0.121 \pm 0.027$	[−1, 1]
Ω (deg)	169.2 ± 1.5	[0, 360]
K_1 (km s^{-1})	6.953 ± 0.058	[1, 20]
K_2 (km s^{-1})	7.86 ± 0.11	[1, 20]
γ (km s^{-1})	$+38.001 \pm 0.033$	[20, 60]
$\Delta RV_{\text{Griffin}}$ (km s^{-1})	-1.102 ± 0.083	[−5, 5]
Error Scaling Factors		
$f_{\text{CfA},1}$	1.09 ± 0.10	[−5, 5]
$f_{\text{CfA},2}$	1.037 ± 0.096	[−5, 5]
$f_{\text{Griffin},1}$	1.08 ± 0.17	[−5, 5]
$f_{\text{Griffin},2}$	1.17 ± 0.19	[−5, 5]
f_{θ}	2.60 ± 0.30	[−5, 5]
f_{ρ}	2.42 ± 0.33	[−5, 5]
Derived Properties		
i (deg)	83.1 ± 1.5	...
e	0.7569 ± 0.0049	...
ω_1 (deg)	224.89 ± 0.66	...
a (au)	20.97 ± 0.23	...
M_1 (M_{\odot})	1.193 ± 0.032	...
M_2 (M_{\odot})	1.055 ± 0.022	...
M_{tot} (M_{\odot})	2.249 ± 0.051	...
$q \equiv M_2/M_1$	0.885 ± 0.015	...
π_{orb} (mas)	12.16 ± 0.23	...
Distance (pc)	82.2 ± 1.6	...

Note. — When expressed in Julian years, the period is 64.0 ± 1.1 yr, and the time of periastron passage is 1995.423 ± 0.026 . The values listed in the table correspond to the mode of the posterior distributions from our MCMC analysis, with uncertainties representing the 68.3% credible intervals. $\Delta RV_{\text{Griffin}}$ is the offset to be applied to the Griffin RVs to place them on the same system as the CfA velocities. The f symbols represent multiplicative scaling factors for the nominal errors of the radial velocity and astrometric measurements, solved for simultaneously with the other elements. Priors in square brackets are uniform over the ranges specified, except those for the error inflation factors f , which are log-uniform.

As in other cases discussed in this section, a simultaneous astrometric-spectroscopic orbital solution is the preferred approach to take advantage of the strengths of each type of observation. Our joint MCMC solution incorporates the Griffin RVs in addition to ours, as well as the astrometric measurements. To account for a possible difference in the zero-points between our RVs and Griffin’s, we solved for an offset $\Delta RV_{\text{Griffin}}$ simultaneously with the other elements, to place his measurements on the same system as ours. We also solved for separate multiplicative scale factors for the nominal RV errors of the primary and secondary from each data set.

The pair’s relative positions have only been measured at times when the angular separation was near maximum, while spectroscopy tightly constrains the orbit at periastron. The early visual measurements are less reliable, particularly some of the angular separations, and several of those are best excluded. Other measurements prior to the 1950s have been assigned uncertainties of 5° in position angle and $0''.02$ in separation. More recent ones are better. The results are presented in Table 14, where the symbols have their usual meaning.

The RV measurements from the CfA and from Griffin

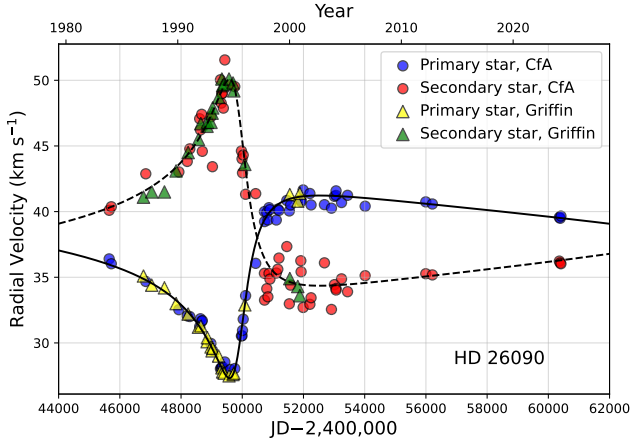


Figure 18. Radial velocity measurements of HD 6090 from this paper and from Griffin (2001), along with our model for the spectroscopic orbit.

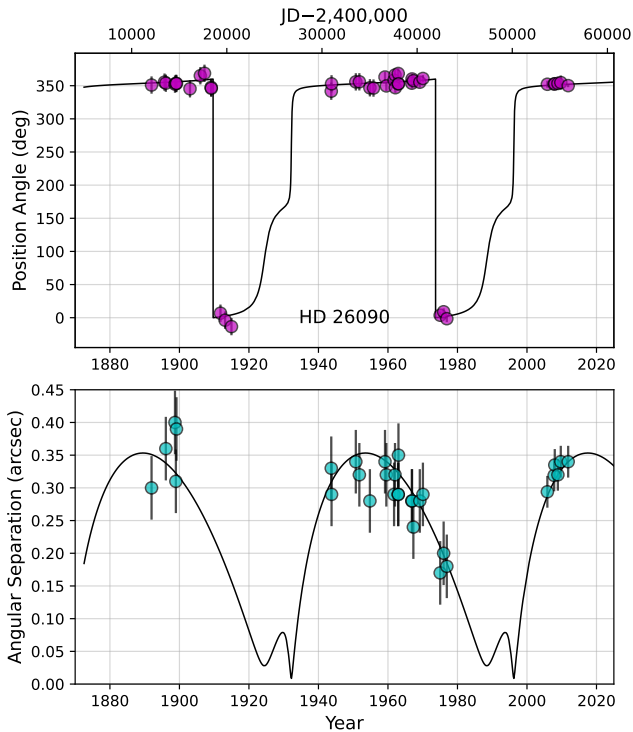


Figure 19. Measured position angles and angular separations for HD 26090 from the WDS, together with our orbit model.

are displayed in Figure 18, showing virtually complete coverage of the 1995 periastron passage. The astrometric measurements (position angles and separations) are shown as a function of time in Figure 19, and are seen to cover two orbital cycles.

In addition to the dynamical masses we obtained, which are formally good to better than 3%, we inferred an orbital parallax of $\pi_{\text{orb}} = 12.16 \pm 0.23$ mas, implying a distance of more than 80 pc. The original Hipparcos catalog (ESA 1997) listed a trigonometric parallax of 10.68 ± 1.43 mas, which was later revised to 12.84 ± 1.07 mas (van Leeuwen 2007). Interestingly, the Gaia DR2 catalog (Gaia Collaboration et al. 2018) re-

ported a much larger value of 24.03 ± 0.50 mas, although the most recent release (DR3; Gaia Collaboration et al. 2023a) has it back down again at 13.95 ± 0.11 mas. None of these values except our own took into account the binarity of the object. The large implied distance, the 15° projected separation from the center of the Hyades, and the fact that the center-of-mass velocity of $+38.0 \text{ km s}^{-1}$ deviates by almost 2.5 km s^{-1} from what is expected for a star at this position in the cluster, led Griffin (2001) to argue that HD 26090 is not a member of the Hyades. We agree with that assessment.

(198) VB 22

This is a well-known member of the Hyades, also referred to as HD 27130. It is a hierarchical triple system in which the inner, 5.6 d binary was found by McClure (1982) to be eclipsing, the brightest such system in the cluster. This makes it special because it enables precise model-independent masses and radii to be determined for the components. This can provide useful constraints on models of stellar evolution, particularly in a cluster like the Hyades with a known age and chemical composition (see, e.g., Lebreton et al. 2001; Pinsonneault et al. 2003; Torres et al. 2019b, 2024a).

The long history of RV observations of vB 22, spanning more than a century, has been described in detail by Griffin et al. (1985a) and by Griffin (2012). Double-lined spectroscopic orbits for vB 22 were published in both of those studies, and also previously by McClure (1982) and Mayor & Mazeh (1987), as well as more recently by Brogaard et al. (2021). Studies of the light curve have been carried out by (McClure 1982) and Schiller & Milone (1987), with the latest being the one by Brogaard et al. (2021).

The first evidence of a possible drift in the center-of-mass velocity of the inner binary was reported by Griffin et al. (1985a), and although they did not go so far as to claim the presence of a third star, surely they would have had that in mind, and recommended further monitoring of the system. Our own spectroscopic observations of vB 22 at the CfA started in October of 1992, and reveal the lines of both stars. By the next season, it was clear from the run of the residuals from a double-lined orbit that the center-of-mass velocity was drifting upward, and over the following two seasons the change reversed course, leaving little doubt as to the cause. By 2002 the residuals had returned to their maximum value from some 8 yr earlier. An orbit for the tertiary was eventually published by Griffin (2012), with a period of 3079 d (8.4 yr). The third star has remained undetected spectroscopically, and is believed to be a faint M dwarf.

We continued to monitor vB 22 until 2013, and we now present an updated simultaneous solution for the inner and outer spectroscopic orbits that incorporates the RV measurements from McClure (1982), Mayor & Mazeh (1987), Mermilliod et al. (2009), Griffin (2012), and Brogaard et al. (2021), in addition to our own. Our velocities from TODCOR used templates with temperatures of 5000 and 4500 K for the primary and secondary, and $v \sin i$ values of 8 and 6 km s^{-1} , respectively. The secondary-to-primary flux ratio we measured at the mean wavelength of our observations is $\ell_{\text{Ab}}/\ell_{\text{Aa}} = 0.072 \pm 0.012$. We assumed the inner and outer orbits are well represented by unperturbed Keplerian models, and light travel time

corrections have been accounted for. The elements and auxiliary quantities are listed in Table 15, from a solution that also includes astrometry, as described below. Because the eccentricity of the inner orbit is very small, it was more convenient to solve for a time of nodal passage, $T_{\text{node,A}}$, which is better defined than a time of periastron passage in such cases, although we also list the latter among the derived quantities. As done for the previous system, we solved for separate multiplicative scale factors for the nominal RV errors of the primary and secondary from each data set, and for velocity zero-point offsets for each source relative to our own. Some of the external sources contribute little to the outer orbit because they do not cover a sufficient interval in phase, and allowing their zero-point to vary freely would negate any benefit they could otherwise provide to that orbit. Nevertheless, we included them because they do help to improve the precision of the inner orbit, and therefore of the absolute masses we report below for the eclipsing components.

The results from our orbital solution are similar to those reported by others, only more precise. We note that the Gaia mission also detected vB 22 as a complex system, and reported both an SB2 solution as well as astrometric acceleration due to the third star (star ‘B’). However, while the RV semiamplitude K_{Aa} of the more massive component from Gaia is similar to ours, their K_{Ab} is 8 km s^{-1} larger than what we and others derive, and must be biased. Figure 20 shows our models for the inner and outer spectroscopic orbits, along with the observations.

It is also possible to constrain the motion of the tertiary of vB 22 on the plane of the sky, using available astrometric information. For this, we combined the RVs with measurements from the Hipparcos mission taken over a period of 2.5 yr, and with the highly precise parallax, position, and proper motion from Gaia DR3. The use of the Hipparcos intermediate data (abscissa residuals) introduces five adjustable parameters in the form of corrections $\Delta\alpha^*$ and $\Delta\delta$ to the catalog values of the position of the barycenter at the mean catalog epoch of 1991.25, corrections $\Delta\mu_\alpha^*$ and $\Delta\mu_\delta$ to the barycenter proper motion components⁹, and a correction to the catalog parallax, $\Delta\pi$. To reduce the number of free parameters, we constrained $\Delta\pi$ using the improved parallax reported as part of the astrometric acceleration solution from Gaia, referenced above ($\pi_{\text{Gaia}} = 21.458 \text{ mas}$), adjusted for a zero-point offset of $+0.035 \text{ mas}$, as recommended by Lindgren et al. (2021). Because Hipparcos did not spatially resolve the tertiary (nor did Gaia), the measurements track the motion of the center of light, so an additional parameter a''_{phot} must be solved for. This represents the semimajor axis of the photocenter orbit, which is a scaled-down version of the relative orbit, reflected about the origin. Checks based on a model isochrone for the Hyades show that, despite the difference in wavelengths between the two space missions, the semimajor axis of the photocenter is not expected to be significantly different for Hipparcos and Gaia, so we have assumed here that they are the same. The final two parameters of the astrometric orbit are the inclination angle, expressed as

⁹ We follow here the practice in the Hipparcos catalog in defining $\Delta\alpha^* \equiv \Delta\alpha \cos \delta$ and $\Delta\mu_\alpha^* \equiv \Delta\mu_\alpha \cos \delta$.

Table 15
Spectroscopic Orbital Parameters for vB 22

Parameter	Value	Prior
Inner Orbit		
P_{A} (day)	$5.60921410 \pm 0.00000058$	[5.5, 5.7]
$T_{\text{node,A}}$ (BJD)	52190.13836 ± 0.00049	[52188, 52192]
$\sqrt{e_{\text{A}}} \cos \omega_{\text{Aa}}$	$+0.017 \pm 0.011$	[-1, 1]
$\sqrt{e_{\text{A}}} \sin \omega_{\text{Aa}}$	$+0.0229 \pm 0.0097$	[-1, 1]
K_{Aa} (km s^{-1})	60.798 ± 0.030	[50, 100]
K_{Ab} (km s^{-1})	83.790 ± 0.051	[50, 100]
γ (km s^{-1})	$+38.475 \pm 0.036$	[10, 50]
$\Delta\text{RV}_{\text{McClure}}$ (km s^{-1})	-0.10 ± 0.24	[-5, 5]
$\Delta\text{RV}_{\text{Griffin}}$ (km s^{-1})	-0.760 ± 0.056	[-5, 5]
$\Delta\text{RV}_{\text{Mayor}}$ (km s^{-1})	-0.08 ± 0.19	[-5, 5]
$\Delta\text{RV}_{\text{Brogaard}}$ (km s^{-1})	$+0.038 \pm 0.092$	[-5, 5]
Outer Orbit		
P_{AB} (day)	3077.8 ± 8.6	[1000, 5000]
$T_{\text{peri,AB}}$ (BJD)	49570 ± 20	[48000, 51000]
$\sqrt{e_{\text{AB}}} \cos \omega_{\text{B}}$	$+0.540 \pm 0.019$	[-1, 1]
$\sqrt{e_{\text{AB}}} \sin \omega_{\text{B}}$	$+0.248 \pm 0.027$	[-1, 1]
K_{A} (km s^{-1})	2.306 ± 0.056	[1, 5]
Error Scaling Factors		
$f_{\text{Aa,DS}}$	1.017 ± 0.059	[-5, 5]
$f_{\text{Ab,DS}}$	0.996 ± 0.055	[-5, 5]
$f_{\text{Aa,TRES}}$	0.96 ± 0.31	[-5, 5]
$f_{\text{Ab,TRES}}$	0.40 ± 0.10	[-5, 5]
$f_{\text{Aa,McClure}}$	0.93 ± 0.15	[-5, 5]
$f_{\text{Ab,McClure}}$	1.23 ± 0.24	[-5, 5]
$f_{\text{Aa,Griffin}}$	1.080 ± 0.077	[-5, 5]
$f_{\text{Ab,Griffin}}$	1.12 ± 0.19	[-5, 5]
$f_{\text{Aa,Mayor}}$	1.59 ± 0.31	[-5, 5]
$f_{\text{Ab,Mayor}}$	1.33 ± 0.48	[-5, 5]
$f_{\text{Aa,Brogaard}}$	1.13 ± 0.30	[-5, 5]
$f_{\text{Ab,Brogaard}}$	1.20 ± 0.28	[-5, 5]
Derived Quantities		
e_{A}	0.00094 ± 0.00041	...
ω_{Aa} (deg)	55 ± 27	...
e_{AB}	0.354 ± 0.017	...
ω_{A} (deg)	24.7 ± 2.9	...
$T_{\text{peri,A}}$ (BJD)	52191.00 ± 0.42	...
$M_{\text{Aa}} \sin^3 i$ (M_{\odot})	1.0181 ± 0.0014	...
$M_{\text{Ab}} \sin^3 i$ (M_{\odot})	0.73874 ± 0.00085	...
$q_{\text{A}} \equiv M_{\text{Ab}}/M_{\text{Aa}}$	0.72560 ± 0.00058	...
$a_{\text{Aa}} \sin i$ (10^6 km)	4.6895 ± 0.0023	...
$a_{\text{Ab}} \sin i$ (10^6 km)	6.4629 ± 0.0040	...
$a_{\text{A}} \sin i$ (R_{\odot})	16.0314 ± 0.0033	...
$M_{\text{B}} \sin i / (M_{\text{A}} + M_{\text{B}})^{2/3}$	0.1474 ± 0.0030	...
$a_{\text{A}} \sin i_{\text{AB}}$ (10^6 km)	91.3 ± 1.9	...

Note. — $T_{\text{node,A}}$, $T_{\text{peri,AB}}$, and $T_{\text{peri,A}}$ are referred to BJD 2,400,000. The values listed correspond to the mode of the posterior distributions from our MCMC analysis, with uncertainties representing the 68.3% credible intervals. Priors in square brackets in the last column are uniform over the ranges specified, except the error inflation factors f , which are log-uniform. Velocity offsets Δ are in the sense ‘‘CfA minus other’’.

$\cos i_{\text{AB}}$, and the position angle of the ascending node, Ω .

The formalism for incorporating Hipparcos abscissa residuals has been described in the Hipparcos documentation (see also, e.g., Torres 2007). The predicted position at the Gaia epoch (α_{G}^* , δ_{G}) was computed as follows, from the other parameters of the model:

$$\begin{aligned} \alpha_{\text{G}}^* &= \alpha_{\text{H}}^* + \Delta\alpha^* + (\mu_{\alpha,\text{H}}^* + \Delta\mu_{\alpha}^*)(t_{\text{G}} - t_{\text{H}}) + \Delta\alpha_{\text{G}}^* \\ \delta_{\text{G}} &= \delta_{\text{H}} + \Delta\delta + (\mu_{\delta,\text{H}} + \Delta\mu_{\delta})(t_{\text{G}} - t_{\text{H}}) + \Delta\delta_{\text{G}}. \end{aligned} \quad (1)$$

Here α_{H}^* and δ_{H} are the published Hipparcos positions

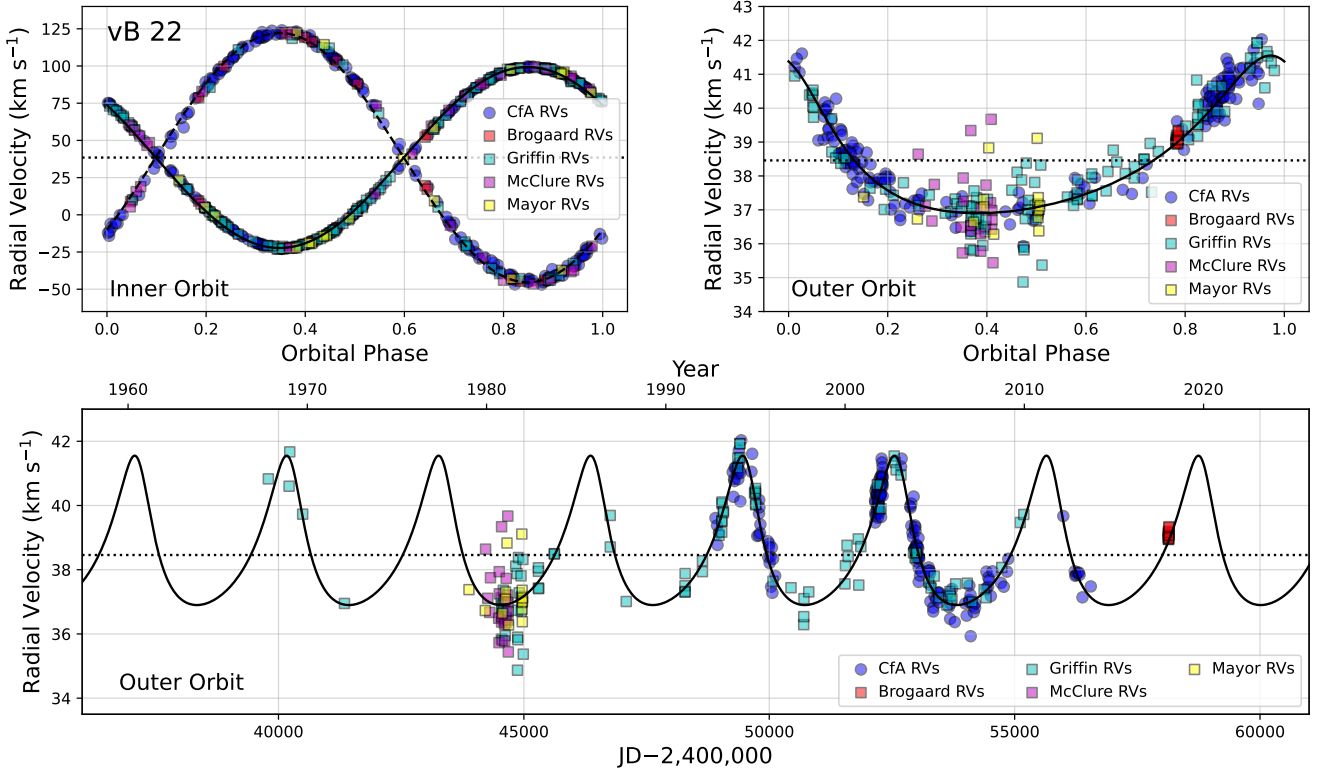


Figure 20. RV measurements for vB 22 together with our models for the inner and outer orbits (phase-folded plots in the top panels; see the text). Each panel has the motion from the other orbit subtracted. The bottom panel shows the outer orbit as a function of time. The center-of-mass velocity of the triple system is indicated with the dotted lines.

at the catalog epoch, $\mu_{\alpha,H}^*$ and $\mu_{\delta,H}$ are the published proper motion components, and t_G and t_H are the mean Hipparcos and Gaia catalog epochs taken from Brandt (2021). The quantities $\Delta\alpha_G^*$ and $\Delta\delta_G$ represent the contributions to the position of the photocenter from orbital motion at the Gaia epoch. They are expressed in terms of the classical Thiele-Innes constants as follows,

$$\begin{aligned} \Delta\alpha^* &= a''_{\text{phot}}(Bx + Gy) \\ \Delta\delta &= a''_{\text{phot}}(Ax + Fy), \end{aligned} \quad (2)$$

in which $x = \cos E - e_{AB}$ and $y = \sqrt{1 - e_{AB}^2} \sin E$, with E being the eccentric anomaly. Because Gaia only observed vB 22 for a fraction of the 8.4 yr period of the tertiary, and the path on the sky is curved, computing the orbital position at the mean Gaia catalog epoch is not the same as taking the average of the positions over each individual epoch (see an illustration of this in Figure 3 of Brandt 2024). We therefore calculated $\Delta\alpha_G^*$ and $\Delta\delta_G$ at each individual Gaia epoch, as predicted by the Gaia Observation Scheduling Tool (GOST; Fernández-Hernández & Joliet 2019), and then took the average.

The predicted proper motion components at the Gaia epoch, $\mu_{\alpha,G}^*$, $\mu_{\delta,G}$, were calculated as

$$\begin{aligned} \mu_{\alpha,G}^* &= \mu_{\alpha,H}^* + \Delta\mu_{\alpha}^* + \Delta\mu_{\alpha,G}^* \\ \mu_{\delta,G} &= \mu_{\delta,H} + \Delta\mu_{\delta}^* + \Delta\mu_{\delta,G}, \end{aligned} \quad (3)$$

where the last terms on the right are the derivatives of the last terms on the right-hand side of eqs.[1].

We used the Hipparcos abscissa residuals from the original catalog (ESA 1997) as well as those from the re-

vised version (van Leeuwen 2007), which are different. Brandt (2018, 2021) has shown that a combination of the original and revised catalogs with relative weights of 0.4 and 0.6, respectively, leads to an improvement in the positions and proper motions over either version. Here we have chosen to apply the same recipe to independent astrometric-spectroscopic solutions using the original and revised abscissae, which give very consistent results. The astrometric parameters from this procedure are listed in Table 16, and the spectroscopic ones were given earlier.

The most recent analysis of the light curve of vB 22 by Brogaard et al. (2021) provided accurate measurements of the photometric parameters of the system. The higher precision of the spectroscopic minimum masses and projected semimajor axis of the eclipsing pair in Table 15 now allows us to improve on the absolute masses and radii for the components. From Table 5 of Brogaard et al. (2021), we adopted weighted mean values for the inclination angle of the inner orbit, the radius ratio, and the sum of the relative radii of $i = 85^\circ.657 \pm 0^\circ.045$, $r_2/r_1 = 0.796 \pm 0.013$, and $r_1 + r_2 = 0.1035 \pm 0.0011$. Revised masses, radii, and surface gravity determinations are included in the bottom section of Table 16, along with the inferred inclination angle and semimajor axis of the relative orbit of the tertiary, a'' . With this, we were able to infer a rather precise value for the mass of the tertiary as well, formally good to about 2%. This adds to the interest of the system, as all three components now have well determined masses. Those for components Aa and Ab are known to better than 0.13%. Even though the third star is not visible in the spectra, it is possible to

Table 16
Astrometric Parameters for vB 22, and Derived Properties

Parameter	Value	Prior
a''_{phot} (mas)	14.95 ± 0.47	[0, 50]
$\cos i_{\text{AB}}$	0.424 ± 0.017	[-1, 1]
Ω (deg)	70.7 ± 3.9	[0, 360]
$\Delta\alpha^*$ (mas)	$+14.7 \pm 1.1$	[-100, 100]
$\Delta\delta$ (mas)	-1.6 ± 1.1	[-100, 100]
$\Delta\mu_{\alpha}^*$ (mas yr $^{-1}$)	$+1.824 \pm 0.035$	[-100, 100]
$\Delta\mu_{\delta}^*$ (mas yr $^{-1}$)	-5.307 ± 0.026	[-100, 100]
Derived Properties		
i_{AB} (deg)	64.9 ± 1.1	...
a'' (mas)	112.76 ± 0.24	...
M_{B} (M_{\odot})	0.2611 ± 0.0056	...
$\mu_{\alpha, \text{bary}}^*$ (mas yr $^{-1}$)	$+114.894 \pm 0.035$...
$\mu_{\delta, \text{bary}}^*$ (mas yr $^{-1}$)	-26.697 ± 0.026	...
M_{Aa} (M_{\odot})	1.0269 ± 0.0014	...
M_{Ab} (M_{\odot})	0.74515 ± 0.00086	...
R_{Aa} (R_{\odot})	0.927 ± 0.012	...
R_{Ab} (R_{\odot})	0.737 ± 0.010	...
$\log g_{\text{Aa}}$ (cgs)	4.516 ± 0.011	...
$\log g_{\text{Ab}}$ (cgs)	4.575 ± 0.012	...
β	0.0034 ± 0.0042	...
ΔHp (mag)	6.2 ± 1.3	...

Note. — The values listed correspond to the mode of the posterior distributions from our MCMC analysis, with uncertainties representing the 68.3% credible intervals. Priors in square brackets in the last column are uniform over the ranges specified. Distributions for the Gaia DR3 parallax and for the photometric parameters taken from Table 5 of (Brogaard et al. 2021) were assumed to be Gaussian.

infer its brightness in the Hipparcos band, relative to the combined light of the inner binary, ΔHp , via the classical relation

$$a''_{\text{phot}} = a'' \left(\frac{M_{\text{B}}}{M_{\text{A}} + M_{\text{B}}} - \beta \right), \quad (4)$$

where $\beta = (1 + 10^{0.4\Delta\text{Hp}})^{-1}$ is the fractional brightness of the third star. In practice, however, β is poorly determined. The magnitude difference is $\Delta\text{Hp} = 6.2 \pm 1.3$ mag.

Confirmation or improvement of the astrometric orbit of the tertiary and its brightness could come from the direct detection of the star by ground-based near-infrared imaging techniques. The angular separation and position angle can now be estimated to be $[0''.050, 155^\circ]$ in mid 2026 and $[0''.068, 229^\circ]$ in mid 2027.

(246) VB 259

This cluster member was announced as a spectroscopic binary by Griffin et al. (1988), who estimated the period to be about 3 yr. It was only seen as single-lined at the time, but subsequent observations allowed both components to be measured. A double-lined orbit was published by Griffin (2012), based on about 20 RV measurements of the two components made between 1990 and 2010.

The observations at the CfA began in 1979 and continued until 2003. All 44 spectra taken with the Digital Speedometers are double-lined. The velocities for both stars were measured with TODCOR, using best-fitting templates with temperatures of 4750 K and 4500 K for the primary and secondary, and no rotational broadening. We measured a flux ratio of $\ell_2/\ell_1 = 0.528 \pm 0.045$ at the

mean wavelength of our observations.

The companion of vB 259 was detected in K -band speckle observations by Patience et al. (1998) at a separation of just 43 mas, and a brightness difference of 0.14 mag at that wavelength. A handful of speckle measurements by others since have now covered most of the orbit, constraining the astrometric elements fairly well. A solution of the speckle orbit was published recently by Tokovinin et al. (2024).

For this work we performed an MCMC analysis combining these astrometric measurements with our own RVs and those of Griffin. We incorporated also the abscissa residuals from the Hipparcos mission, weighted as explained above for vB 22, which show hints that the motion of the photocenter is detectable. They therefore help to constrain the astrometric elements. The results are listed in Table 17 in a similar format as employed previously. Plots of the visual and spectroscopic orbit models and observations are shown in Figure 21. Unfortunately, the dynamical masses are not well constrained in this case because the inclination of the orbit is rather low, and its uncertainty is significant.

(374) VB 80

This bright visual binary member, with a current separation of about $1''.5$ and a brightness difference of 2.5 mag, was observed many times in combined light with the Digital Speedometers at the CfA between 1989 and 1999, including several attempts to split the components on nights of good seeing. However, the limited signal-to-noise ratios with those instruments and especially the rapid rotational velocity of the primary star ($v \sin i \approx 180 \text{ km s}^{-1}$) have prevented us from extracting useful RV information. A handful of spectra of the combined light were also gathered with TRES more recently, between 2011 and 2013.

The latest solution for the 172 yr, highly eccentric astrometric orbit of vB 80 ($e = 0.915$) was reported by Torres (2019). That study made use of ground-based visual and speckle observations, as well as proper motions for the individual components from the Gaia and Hipparcos missions, but did not use RVs because they were not considered to be reliable at the time. Nevertheless, the astrometry alone allowed the determination of the mass ratio as well as the dynamical masses for both stars.

We have reanalyzed the six TRES spectra of the combined light using TODCOR, and we are now able to extract meaningful velocities for the two components using templates with effective temperatures of 7750 and 5750 K, along with $v \sin i$ values of 180 and 6 km s^{-1} . Given the angular separation and the $2''.3$ diameter of the spectrograph fiber, the amount of flux from each star entering the instrument under typical sky conditions is highly dependent on seeing and guiding, so for this case we left the flux ratio between the primary and secondary as a free parameter for each exposure. The velocities we obtained are shown in Figure 22 together with the spectroscopic orbit of vB 80, all of whose parameters are known or can be inferred from the visual elements by Torres (2019) and the masses, except for the center-of-mass velocity. With all other orbital parameters held fixed, the determination of this missing parameter using the measured velocities yields $\gamma \approx 40.06 \text{ km s}^{-1}$, which is in very good agreement with the expected astrometric velocity for the sys-

Table 17
Orbital Parameters for vB 259

Parameter	Value	Prior
P (days)	1042.14 ± 0.45	[500, 2000]
T_{peri} (BJD-2,400,000)	49947.6 ± 5.3	[49700, 50500]
a'' (")	0.05003 ± 0.00072	[0.02, 0.10]
$\sqrt{e} \cos \omega_1$	$+0.227 \pm 0.014$	[-1, 1]
$\sqrt{e} \sin \omega_1$	-0.430 ± 0.011	[-1, 1]
$\cos i$	$+0.824 \pm 0.021$	[-1, 1]
Ω (deg)	135.8 ± 1.4	[0, 360]
K_1 (km s $^{-1}$)	6.852 ± 0.092	[1, 20]
K_2 (km s $^{-1}$)	7.38 ± 0.17	[1, 20]
γ (km s $^{-1}$)	$+40.239 \pm 0.090$	[20, 60]
$\Delta RV_{\text{Griffin}}$ (km s $^{-1}$)	-0.55 ± 0.13	[-5, 5]
a''_{phot} (mas)	7.0 ± 2.9	[0, 50]
$\Delta\alpha^*$ (mas)	$+3.6 \pm 2.1$	[-100, 100]
$\Delta\delta$ (mas)	-1.4 ± 1.2	[-100, 100]
$\Delta\mu^*_\alpha$ (mas yr $^{-1}$)	$+3.6 \pm 2.9$	[-100, 100]
$\Delta\mu_\delta$ (mas yr $^{-1}$)	-6.0 ± 2.3	[-100, 100]
Error Scaling Factors		
$f_{\text{CfA},1}$	1.08 ± 0.12	[-5, 5]
$f_{\text{CfA},2}$	0.93 ± 0.11	[-5, 5]
$f_{\text{Griffin},1}$	1.08 ± 0.20	[-5, 5]
$f_{\text{Griffin},2}$	1.10 ± 0.20	[-5, 5]
f_θ	2.3 ± 1.3	[-5, 5]
f_ρ	1.26 ± 0.66	[-5, 5]
Derived Properties		
i (deg)	34.5 ± 2.2	...
e	0.2376 ± 0.0078	...
ω_1 (deg)	297.9 ± 1.9	...
a (au)	2.33 ± 0.14	...
M_1 (M_\odot)	0.78 ± 0.15	...
M_2 (M_\odot)	0.72 ± 0.13	...
M_{tot} (M_\odot)	1.52 ± 0.28	...
$q \equiv M_2/M_1$	0.928 ± 0.025	...
π_{orb} (mas)	21.3 ± 1.5	...
Distance (pc)	46.3 ± 3.3	...

Note. — The values listed in the table correspond to the mode of the posterior distributions from our MCMC analysis, with uncertainties representing the 68.3% credible intervals. Δ_{Griffin} is the offset to be applied to the Griffin RVs to place them on the same system as the CfA velocities. The f symbols represent multiplicative scaling factors for the nominal errors of the radial velocity and astrometric measurements, solved for simultaneously with the other elements. Priors in square brackets are uniform over the ranges specified, except those for the error inflation factors f , which are log-uniform.

tem (39.93 km s $^{-1}$). The difference of only 0.13 km s $^{-1}$ is well within the internal velocity dispersion of the cluster (see Section 12).

(417) VB 96

This is a double-lined binary with a period just under 14 yr, and is a long-recognized member of the Hyades. The spectroscopic orbit published by Griffin (2012) rests on spectrometer scans he collected between 2002 and 2012, although only the ones after 2007 allowed him to measure RVs for both components. As this represents less than one cycle, Griffin was forced to hold the period fixed at a value determined by including earlier measurements of lower quality that did not split the components, on the assumption that they represented the primary.

Observations at the CfA were carried out earlier with the Digital Speedometers between 1980 and 2001, and both stars can be seen in most of the 58 spectra, which cover 1.5 cycles of the binary. The templates for our

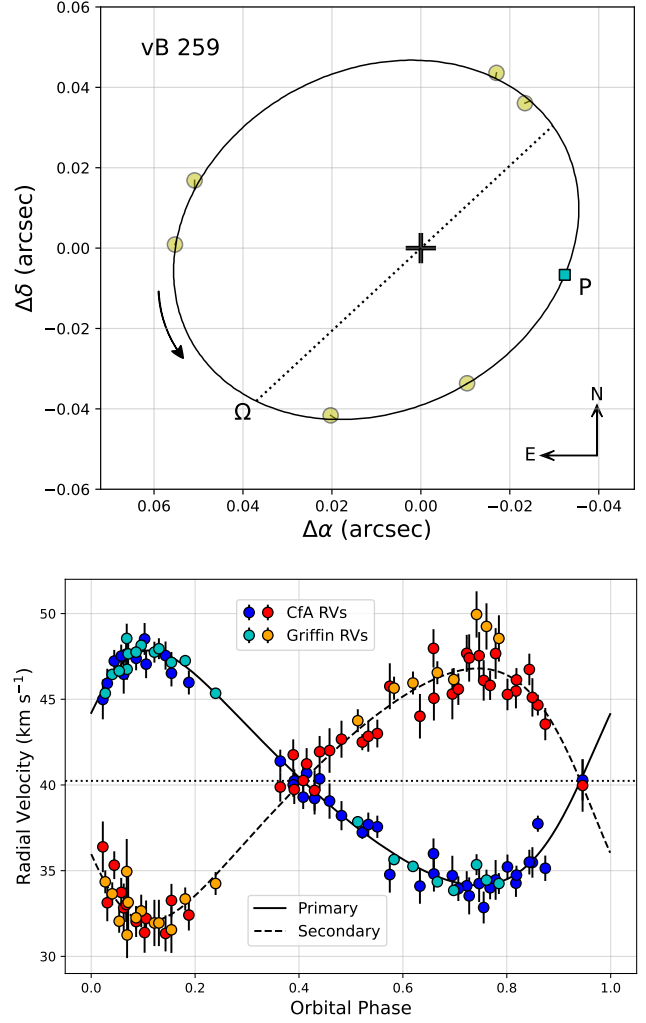


Figure 21. *Top:* Astrometric observations of vB 259 together with our model for the orbit. Periastron is marked with a square and labeled ‘P’. The dotted line represents the line of nodes, with the ascending node labeled Ω . *Bottom:* RV measurements together with our model for the spectroscopic orbit. The center-of-mass velocity is indicated with the dotted line.

TODCOR analysis had temperatures of 5500 and 4750 K for the primary and secondary, and zero rotational broadening. The flux ratio we determined at the mean wavelength of our observations is $\ell_2/\ell_1 = 0.200 \pm 0.017$.

The companion of vB 96 was spatially resolved in 1985 with the speckle interferometry technique by McAlister et al. (1987), at a separation of 0".15. The double star designation is WDS 04340+1510. About four dozen astrometric observations have been obtained since, and trace the orbit over 2.5 cycles quite well (e.g., Cvetković & Ninković 2008), although measurements near periastron are sparse because the angular separation there is less than 0".05. The Gaia mission reported the binary was partially resolved in 9% of the observations.

Here we have combined the RV and speckle measurements in order to derive model-independent masses for the components. The results of our MCMC analysis are given in Table 18 in a similar format as for other systems. The dynamical masses for the primary and secondary of vB 96 are determined to about 4% and 3%, respectively, and the uncertainty of the orbital parallax

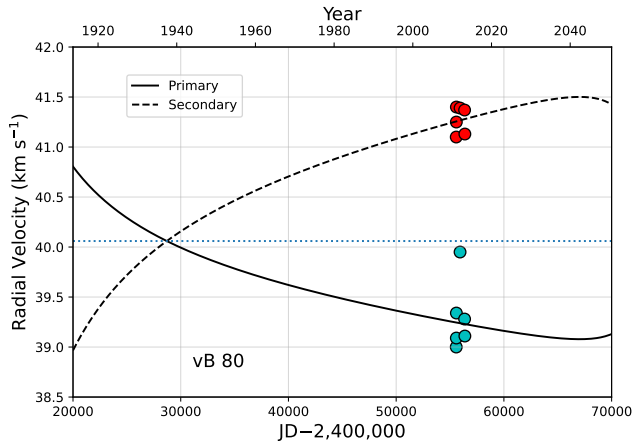


Figure 22. RV measurements for vB 80, compared with a section of the spectroscopic orbit calculated from the visual elements of Torres (2019) and the velocity semi-amplitudes inferred from the individual masses in that work. The only free parameter we have adjusted is the center-of-mass velocity (dotted line), $\gamma = 40.06 \text{ km s}^{-1}$. The one discrepant primary measurement happens to be from a spectrum of much lower signal-to-noise ratio compared to the others.

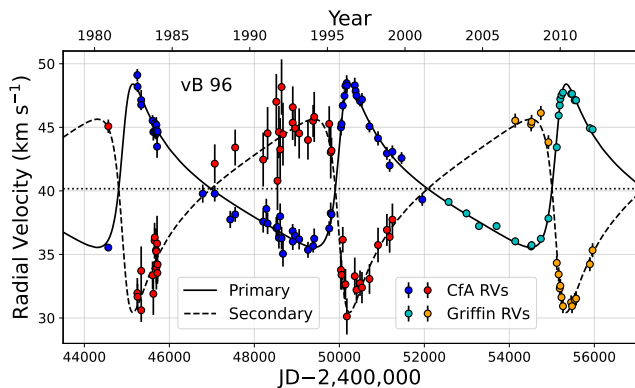


Figure 23. RV measurements for vB 96, along with our best-fit model. The dotted line marks the center-of-mass velocity.

is 1.3%, a factor of two smaller than the value reported in the Gaia DR3 catalog. The Gaia parallax is also about 1 mas smaller than ours: $\pi_{\text{DR3}} = 20.68 \pm 0.61 \text{ mas}$, including a correction for the known zero-point offset (Lindgren et al. 2021). The spectroscopic orbit is shown in Figure 23, and the astrometric measurements together with our model are seen in Figure 24.

The V -band brightness difference between the components, from an average of eight independent measures contained in the WDS, is $1.38 \pm 0.03 \text{ mag}$. By adopting a consensus apparent brightness from the literature of $V = 8.495 \pm 0.020 \text{ mag}$, along with the distance we obtain, we infer absolute visual magnitudes for the components of 5.440 ± 0.035 and $6.815 \pm 0.042 \text{ mag}$. These values along with the masses are compared against evolutionary models for the Hyades in Figure 25, and show good agreement. The secondary falls one or two tenths of a magnitude below the predictions, and seems to follow an emerging trend found for other cluster stars (see, e.g., Torres et al. 2024a).

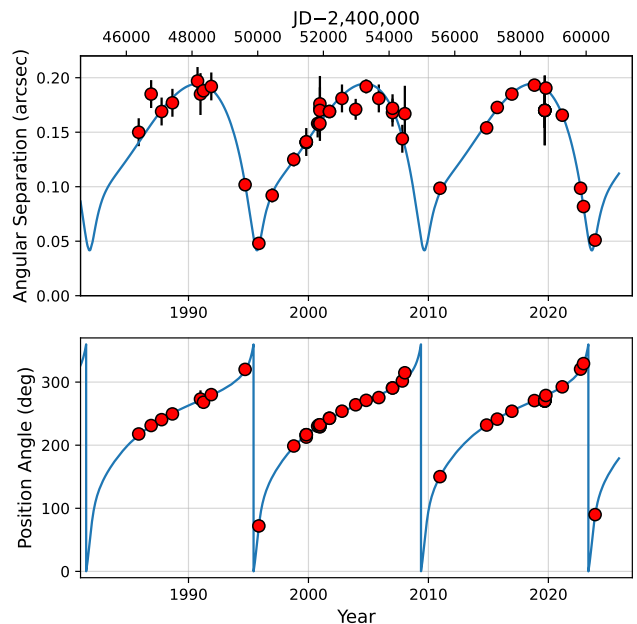
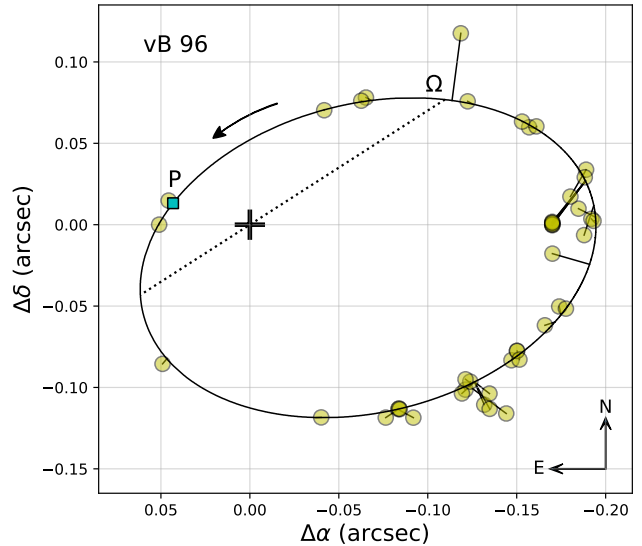


Figure 24. Astrometric orbit of vB 96; see Figures 21 and 19.

(450) VB 304

This is a hierarchical triple system (HD 285947), and a member of the cluster. The inner binary has a period of 60 d and a moderate eccentricity (Griffin et al. 1985a), but only the primary was detected in those authors' spectroscopic observations. The third star in the system was discovered in a K -band speckle imaging survey of the Hyades by Patience et al. (1998), at a separation of about $0''.2$. The system has received the double star designation WDS 04384+1733. Subsequently, Tomkin & Griffin (2002) were able to detect the secondary of the inner binary in their higher quality spectra, as well as a drift of the center-of-mass velocity in response to the third star. The tertiary, which they estimated to be a much fainter mid-M dwarf, remained undetected. Tomkin & Griffin (2002) combined their RVs with those of Griffin, and estimated the period of the tertiary to be about

Table 18
Orbital Parameters for vB 96

Parameter	Value	Prior
P (days)	5097.5 ± 2.8	[3000, 10000]
T_{peri} (BJD-2,400,000)	50036.9 ± 4.7	[48000, 52000]
a'' (")	0.15220 ± 0.00042	[0.02, 0.40]
$\sqrt{e} \cos \omega_1$	$+0.3607 \pm 0.0045$	[-1, 1]
$\sqrt{e} \sin \omega_1$	-0.6899 ± 0.0030	[-1, 1]
$\cos i$	$+0.6699 \pm 0.0037$	[-1, 1]
Ω (deg)	305.03 ± 0.38	[0, 360]
K_1 (km s $^{-1}$)	6.426 ± 0.069	[1, 30]
K_2 (km s $^{-1}$)	7.60 ± 0.14	[1, 30]
γ (km s $^{-1}$)	$+40.171 \pm 0.072$	[20, 60]
$\Delta RV_{\text{Griffin}}$ (km s $^{-1}$)	-1.068 ± 0.091	[-5, 5]
Error Scaling Factors		
$f_{\text{CfA},1}$	1.04 ± 0.10	[-5, 5]
$f_{\text{CfA},2}$	1.01 ± 0.10	[-5, 5]
$f_{\text{Griffin},1}$	1.15 ± 0.21	[-5, 5]
$f_{\text{Griffin},2}$	1.06 ± 0.22	[-5, 5]
f_{θ}	1.93 ± 0.22	[-5, 5]
f_{ρ}	3.13 ± 0.34	[-5, 5]
Derived Properties		
i (deg)	47.94 ± 0.29	...
e	0.6059 ± 0.0020	...
ω_1 (deg)	297.62 ± 0.39	...
a (au)	7.046 ± 0.084	...
M_1 (M_{\odot})	0.969 ± 0.040	...
M_2 (M_{\odot})	0.820 ± 0.026	...
M_{tot} (M_{\odot})	1.795 ± 0.064	...
$q \equiv M_2/M_1$	0.846 ± 0.019	...
π_{orb} (mas)	21.63 ± 0.28	...
Distance (pc)	46.22 ± 0.60	...

Note. — When expressed in Julian years, the period is 13.9562 ± 0.0077 yr, and the time of periastron passage is 1995.871 ± 0.013 . The values listed in the table correspond to the mode of the posterior distributions from our MCMC analysis, with uncertainties representing the 68.3% credible intervals. Δ_{Griffin} is the offset to be applied to the Griffin RVs to place them on the same system as the CfA velocities. The f symbols represent multiplicative scaling factors for the nominal errors of the radial velocity and astrometric measurements, solved for simultaneously with the other elements. Priors in square brackets are uniform over the ranges specified, except those for the error inflation factors f , which are log-uniform.

8000 d, although they could not rule out a longer period of roughly 10,000 d.

Our own observations of vB 304 at the CfA began in 1980. We measured the velocities of both components of the inner pair (listed in Table 4) using templates with $T_{\text{eff}} = 4750$ and 4000 K for the primary and secondary, and $v \sin i = 2$ km s $^{-1}$ for both. The measured flux ratio is $\ell_{\text{Ab}}/\ell_{\text{Aa}} = 0.108 \pm 0.006$ at 5187 Å. Although our spectra show no sign of the third star, its dynamical influence on the velocities of the primary and secondary is obvious. A combined spectroscopic solution of the inner and outer orbits using our RVs, similar to the one performed by Tomkin & Griffin (2002), supports the period of ~ 8000 d proposed by those authors, and our velocities now cover two cycles of that orbit. Furthermore, astrometric measurements of the relative position of the tertiary since its discovery have been obtained by several observers, and those observations independently confirm the outer period. An astrometric-only orbital solution by Tokovinin (2021a) gives the period as 22.92 ± 0.15 yr (8383 ± 55 d), and other orbital elements consistent with ours.

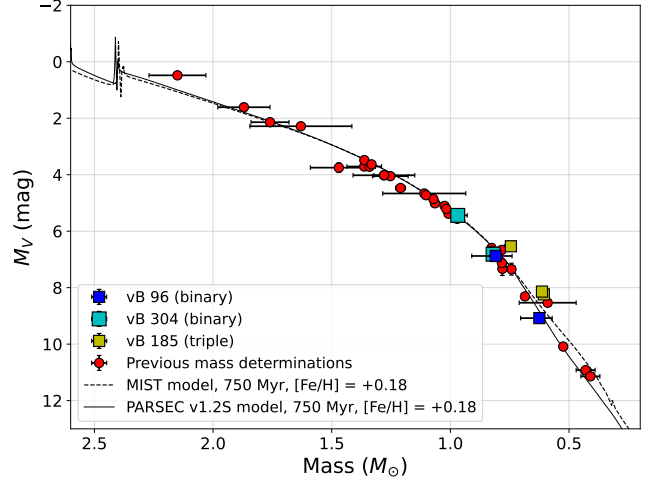


Figure 25. Mass-luminosity relation for the Hyades in the visual band. Empirical determinations are shown for vB 96, vB 304, and vB 185, as labeled. Circles represent other previously published dynamical mass determinations in the cluster. The lines show model isochrones from the PARSEC v1.2S series (Chen et al. 2014) and the MIST series (Choi et al. 2016).

Here we have performed a joint MCMC astrometric-spectroscopic orbital solution combining the RVs of Griffin, Tomkin, and our own, along with the astrometric measurements of the tertiary from the WDS. As pointed out by Tomkin & Griffin (2002), however, in principle the Griffin measurements of the primary could be biased due to blending with the much fainter secondary star, which was not seen in those observations. Because they go back to 1973, the Griffin measurements are potentially valuable for constraining the outer orbit. Therefore, as a test, we incorporated them and allowed them to contribute to the determination of their own value of the velocity semiamplitude K_{Aa} , separate from the one constrained by the other observations. The remaining spectroscopic elements of the inner binary were constrained by all observations. While the Griffin semiamplitude did come out marginally smaller than the value from the other observations, the difference was much smaller than the uncertainties, so we chose to ignore it and to solve for a single common parameter K_{Aa} . A similar concern could be raised about the even fainter tertiary, which neither we nor Tomkin or Griffin detected, but its effect will be completely negligible.

Table 19 presents the results and other derived properties from our combined astrometric-spectroscopic solution, compared to orbital solutions by others. For the inner binary, the times of observation were adjusted iteratively in our solution for the light travel time resulting from motion in the outer orbit.

The inner and outer spectroscopic orbits are shown in Figure 26. The orbit of the tertiary on the plane of the sky is shown in the top panel of Figure 27. The lower panels display the position angle and angular separation as a function of time, along with our best-fit model. The WDS measurements cover slightly more than one orbital cycle.

While the astrometry provides additional properties of the outer orbit, it is not sufficient to make a determination of the masses of the three stars in vB 304 because the tertiary has not been detected spectroscopi-

Table 19
Orbital Parameters for vB 304, Compared with Results by Others

Parameter	Griffin et al. (1985a)	Tomkin & Griffin (2002)	Tokovinin (2021a)	This paper	Prior
P_A (day)	60.821 ± 0.013	60.8081 ± 0.0005	...	60.80936 ± 0.00017	[40, 80]
$T_{\text{peri},A}$ (BJD)	44397.6 ± 0.4	50417.70 ± 0.06	...	50174.555 ± 0.041	[51140, 51200]
$\sqrt{e_A} \cos \omega_{Ab}$	-0.3670 ± 0.0014	[-1, 1]
$\sqrt{e_A} \sin \omega_{Ab}$	$+0.2723 \pm 0.0019$	[-1, 1]
K_{Aa} (km s $^{-1}$)	25.27 ± 0.22	25.85 ± 0.04	...	25.818 ± 0.019	[5, 50]
K_{Ab} (km s $^{-1}$)	...	33.44 ± 0.10	...	33.439 ± 0.089	[5, 50]
P_{AB} (day)	...	8074 ± 81	8386 ± 55	8310 ± 17	[5000, 12000]
$T_{\text{peri},AB}$ (BJD)	...	51548 ± 26	51538 ± 26	51561 ± 14	[50000, 53000]
a_{AB}'' (")	0.210 ± 0.005	0.2117 ± 0.0056	[0.1, 0.5]
$\sqrt{e_{AB}} \cos \omega_A$	-0.376 ± 0.016	[-1, 1]
$\sqrt{e_{AB}} \sin \omega_A$	-0.6943 ± 0.0070	[-1, 1]
$\cos i_{AB}$	0.803 ± 0.024	[-1, 1]
Ω_{AB} (deg)	161.7 ± 3.1	341.3 ± 2.1	[0, 360]
K_A (km s $^{-1}$)	...	2.18 ± 0.06	...	2.146 ± 0.051	[0.1, 10]
γ (km s $^{-1}$)	$+42.43 \pm 0.14$	$+40.17 \pm 0.07$...	$+40.165 \pm 0.040$	[30, 60]
ΔRV (km s $^{-1}$)	-0.412 ± 0.051	[-5, 5]
Error Scaling Factors					
$f_{Aa, \text{Tom}}$	1.128 ± 0.091	[-5, 5]
$f_{Ab, \text{Tom}}$	1.06 ± 0.15	[-5, 5]
$f_{Aa, \text{CfA}}$	1.004 ± 0.093	[-5, 5]
$f_{Ab, \text{CfA}}$	0.998 ± 0.088	[-5, 5]
f_θ	3.0 ± 1.0	[-5, 5]
f_ρ	3.00 ± 0.81	[-5, 5]
Derived Properties					
e_A	0.218 ± 0.008	0.2102 ± 0.0016	...	0.20886 ± 0.00093	...
ω_{Aa} (deg)	143.0 ± 2.1	142.9 ± 0.4	...	143.43 ± 0.27	...
i_A (deg)	70.9 ± 6.1	...
i_{AB} (deg)	36.2 ± 2.5	36.6 ± 2.3	...
e_{AB}	...	0.604 ± 0.017	0.611 ± 0.015	0.6232 ± 0.0090	...
ω_A (deg)	...	242.9 ± 2.5	241.4 ± 2.3	241.6 ± 1.2	...
K_B (km s $^{-1}$)	7.65 ± 0.84	...
a_{AB} (au)	9.83 ± 0.26	...
M_{AB} (M_\odot)	1.83 ± 0.15	...
M_A (M_\odot)	1.43 ± 0.15	...
M_{Aa} (M_\odot)	0.809 ± 0.085	...
M_{Ab} (M_\odot)	0.624 ± 0.066	...
M_B (M_\odot)	0.403 ± 0.014	...
$q \equiv M_{Ab}/M_{Aa}$...	0.773 ± 0.002	...	0.7721 ± 0.0022	...
$q \equiv M_B/M_A$	0.278 ± 0.031	...

Note. — The values listed correspond to the mode of the posterior distributions from our MCMC analysis, with uncertainties representing the 68.3% credible intervals. Times of periastron passage are referred to BJD 2,400,000. The values of $T_{\text{peri},A}$ by other authors differ from ours by very nearly an integer number of cycles. ΔRV represents a systematic velocity offset added to our velocities to translate them to the reference frame of Tomkin. The f symbols represent multiplicative scaling factors for the nominal errors of the radial-velocity and astrometric measurements, solved for simultaneously with the other elements. Priors in square brackets in the last column are uniform over the ranges specified, except those for the error inflation factors, which are log-uniform.

cally. For this, we made use of the parallax provided in the Gaia DR3 catalog, $\pi_{\text{DR3}} = 21.54 \pm 0.11 \text{ mas}^{10}$. Because of the complicated nature of the source, the reported parallax uncertainty is several times larger than is typical for stars of this brightness. If taken at face value, this parallax leads to absolute masses for the three stars as listed in the bottom section of Table 19. Other derived properties are listed there as well. The masses we inferred for the primary and secondary are somewhat larger than those suggested by Tomkin & Griffin (2002), which relied on an adopted spectral type for the primary.

With an estimate of the absolute magnitudes of the primary and secondary, a comparison is possible against predictions from stellar evolution models for the Hyades cluster. Our measured spectroscopic flux ratio, con-

verted to the V band using PHOENIX model spectra from Husser et al. (2013), leads to a brightness difference of $\Delta V = 2.20 \pm 0.13 \text{ mag}$. Apparent magnitude measurements for vB 304 in the literature vary by a little more than 0.1 mag, and $B - V$ estimates by 0.3 mag, possibly due to intrinsic variability caused by spots. We therefore adopted the brighter of the magnitude estimates, $V = 10.077 \pm 0.069$ (from the Tycho-2 Catalog, transformed to the Johnson system; Høg et al. 2000), which may be expected to more closely represent the unspotted stellar surfaces. After a small correction of +0.01 mag to remove the light contribution from the tertiary (based on its mass), we obtained absolute magnitudes for the primary and secondary of $M_V = 6.878 \pm 0.072$ and 9.08 ± 0.13 , respectively, ignoring extinction. The comparison against model isochrones for the Hyades is shown in Figure 25, together with other empirical mass determinations in the cluster. The properties of vB 304 derived

¹⁰ This value includes a parallax zero-point correction of +0.036 mas (Lindegren et al. 2021).

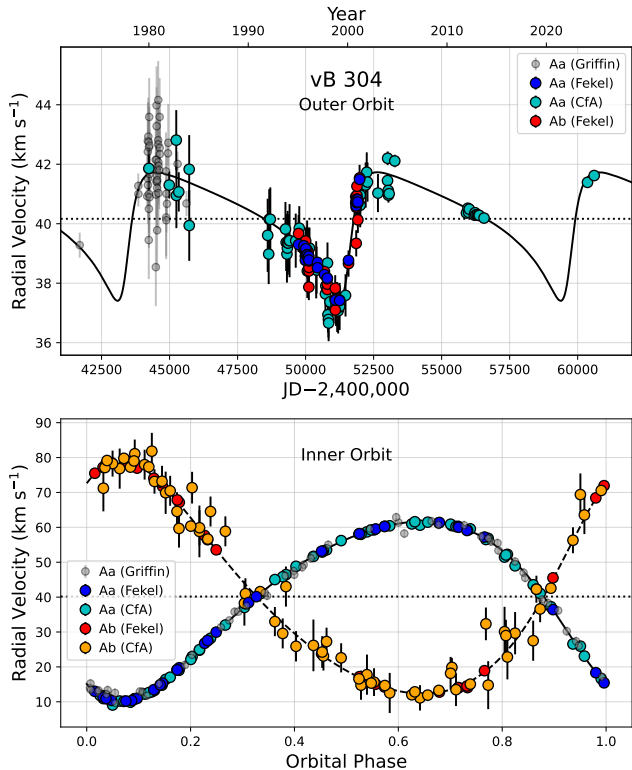


Figure 26. *Top:* Our model for the outer spectroscopic orbit of vB 304, together with the RV measurements of the primary and secondary from which the inner motion has been subtracted. The dotted line represents the center of mass of the triple system. *Bottom:* Velocities in the inner spectroscopic orbit, after removing the motion of the inner binary in the outer orbit.

here should be considered to be preliminary, given the incomplete astrometric coverage and the need to rely on the Gaia parallax to constrain the solution.

(466) VB 185

This is another hierarchical triple system, and a member of the cluster, also known as HD 29608. As in the case of vB 304, the initial report of a spectroscopic orbit for the inner binary is due to Griffin et al. (1985a), and was based on the detection of the primary star only. The period is 276 days. The outer companion was first recorded by the Hipparcos mission at a separation of $0''.46$, and carries the designation WDS 04404+1631.¹¹ In a more detailed spectroscopic study by Tomkin (2003), all three stars in the system were detected, and a drift in the center-of-mass velocity of the inner binary was measured for the first time, resulting from the action of the tertiary. Masses for the components were estimated from assumed spectral types of K0, K5, and K5 for components Aa, Ab, and B.

Spectroscopic observations at the CfA began on New Years Day, 1980. The spectra from the Digital Speedometers only show the primary clearly; the velocities may be found in Table 3. The more recent spectra from TRES show all three stars, and their radial velocities were measured with TRICOR. They are listed in Ta-

¹¹ A claimed detection in 1991 by speckle interferometry (Mason et al. 1993), along with several subsequent ones, turns out to be of a different binary, as indicated in the WDS.

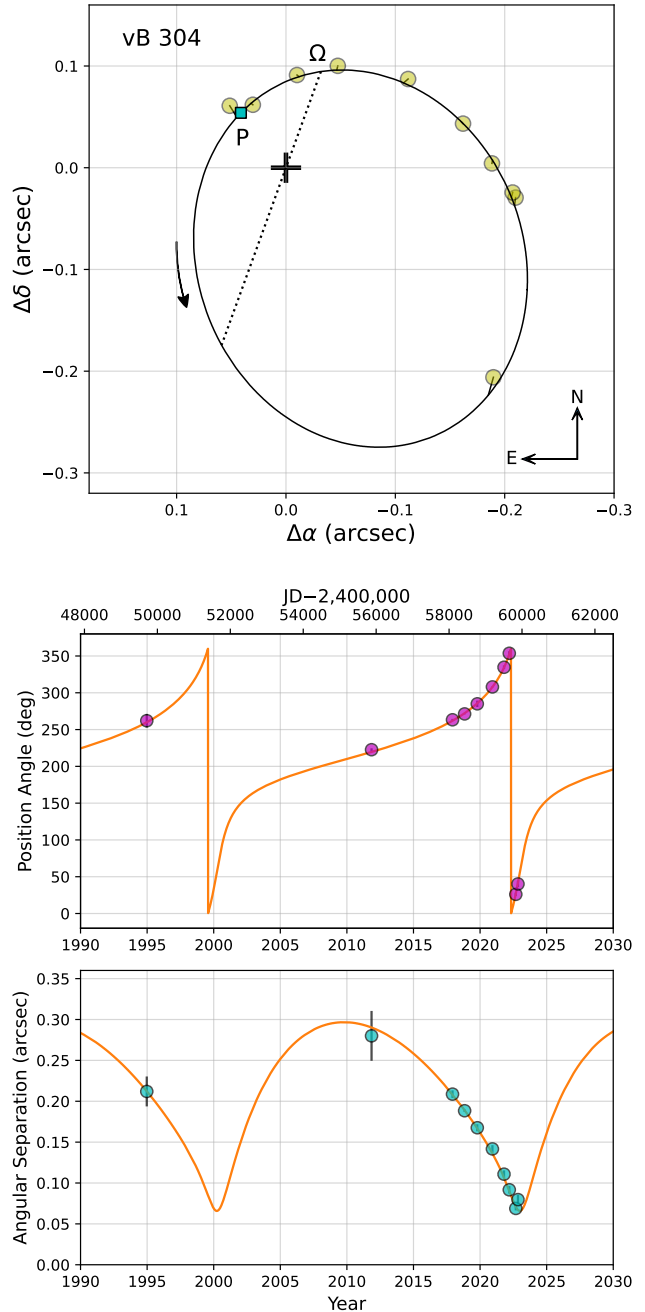


Figure 27. Astrometric orbit of vB 304, similar to Figure 24.

ble 20. For the primary we adopted a synthetic template with $T_{\text{eff}} = 5000$ K, and for the secondary and tertiary we used $T_{\text{eff}} = 4250$ K. Surface gravities of $\log g = 4.5$ were assumed, along with no rotational broadening. The measured flux ratios at the mean wavelength of our observations (~ 5187 Å) are $\ell_2/\ell_1 = 0.160 \pm 0.011$ and $\ell_3/\ell_1 = 0.175 \pm 0.013$.

More than two dozen additional measurements of the relative position of the wide companion of vB 304 have been made since its discovery, and are listed in the WDS, although they only cover a bit less than half of the outer orbit. An astrometric solution with a period of 68.2 yr was reported by Tokovinin (2021b). The spectroscopic observations of Griffin et al. (1985a) predate the astro-

Table 20
Radial Velocity measurements of vB 185 from TRES

BJD (2,400,000+)	RV_{Aa} (km s^{-1})	RV_{Ab} (km s^{-1})	RV_B (km s^{-1})
55910.9633	57.24	23.27	38.20
55965.6634	51.09	31.31	38.20
56016.5925	35.97	50.40	38.21
56196.0179	57.60	23.83	38.19
56228.0360	54.23	28.39	38.34
56290.8993	36.80	49.63	38.63
56309.8581	31.60	56.82	37.80
56348.7480	25.74	63.11	37.14
56385.6217	33.11	55.19	37.98
56559.0011	39.74	46.98	38.61
60354.6585	58.37	25.03	36.20
60364.7123	57.55	26.03	36.41
60386.6782	53.95	29.86	36.11
60591.0211	54.78	29.05	36.38
60600.8943	56.80	26.84	36.19
60612.9908	58.12	26.36	36.39
60614.0255	58.30	24.77	36.49

Note. — Initial uncertainties for our orbital analysis were assumed to be 0.15, 0.60, and 0.60 km s^{-1} for stars Aa, Ab, and B, respectively.

metric ones by about 20 years, and the CfA observations started about 10 years before the astrometry. Both could help with the period. We therefore carried out a combined MCMC astrometric-spectroscopic analysis, which included the RVs of Griffin et al. (1985a), Tomkin (2003), our own, and the relative positions from the WDS. In principle this allows the masses of all three stars to be derived, along with the orbital parallax. A caveat is that the spectroscopic observations of Griffin et al. (1985a) and the CfA spectra obtained with the Digital Speedometers only reveal the brighter primary star, so its radial velocities may be influenced by the presence of the other two components. This will generally add scatter, and the measured primary velocities will tend to underestimate the true RV range for that star, resulting in a bias of the semiamplitude K_{Aa} toward smaller values. For this reason, in addition to the standard orbital elements, our orbital analysis allowed both the Griffin velocities and the Digital Speedometer velocities to contribute to their own primary velocity semiamplitude for the inner binary, as done for vB 304. We also allowed for systematic offsets between the velocities of Griffin and our own relative to those of Tomkin. As a precaution, we also solved for a systematic offset between the primary and secondary velocities from TRES, to guard against the possibility of template mismatch.

Initial tests gave unrealistically small masses, along with a small distance. More reasonable results were obtained by imposing a Gaussian prior on the orbital parallax, based on the parallax π_{DR3} as listed in the Gaia DR3 catalog, along with its corresponding uncertainty. Because the system is complex, the parallax error from Gaia is many times larger than it would otherwise be. Furthermore, a bias in π_{DR3} cannot be ruled out. We present the results of our solution in Table 21, although we consider them to be preliminary at the moment given the incomplete observational coverage of the outer orbit. It is also possible that some of the uncertainties are underestimated.

The period of the outer orbit (79.2 yr) is 1.5% longer

Table 21
Orbital Parameters for vB 185

Parameter	Value	Prior
Outer Orbit		
P_{AB} (yr)	79.2 ± 1.8	[30, 100]
$T_{\text{peri},AB}$ (yr)	2007.48 ± 0.21	[1980, 2020]
a_{AB} (")	0.4878 ± 0.0041	[0.1, 0.7]
$\sqrt{e_{AB}} \cos \omega_B$	$+0.040 \pm 0.015$	[-1, 1]
$\sqrt{e_{AB}} \sin \omega_B$	$+0.507 \pm 0.015$	[-1, 1]
$\cos i_{AB}$	$+0.4837 \pm 0.0097$	[-1, 1]
Ω_{AB} (deg)	358.95 ± 0.42	[0, 360]
K_A (km s^{-1})	2.416 ± 0.066	[0.5, 20]
K_B (km s^{-1})	5.31 ± 0.13	[0.5, 20]
γ (km s^{-1})	$+40.610 \pm 0.069$	[30, 50]
Inner Orbit		
P_A (day)	276.7678 ± 0.0085	[200, 400]
$T_{\text{peri},A}$ (BJD-2,400,000)	50021.19 ± 0.66	[49900, 50100]
$\sqrt{e_A} \cos \omega_{Aa}$	-0.1546 ± 0.0042	[-1, 1]
$\sqrt{e_A} \sin \omega_{Aa}$	-0.2698 ± 0.0035	[-1, 1]
K_{Aa} (km s^{-1})	15.950 ± 0.027	[5, 50]
K_{Ab} (km s^{-1})	19.625 ± 0.043	[5, 50]
$K_{Aa,Griffin}$ (km s^{-1})	14.19 ± 0.22	[5, 50]
$K_{Aa,DS}$ (km s^{-1})	15.00 ± 0.16	[5, 50]
ΔRV_{CfA} (km s^{-1})	-0.45 ± 0.11	[-5, 5]
$\Delta RV_{\text{Griffin}}$ (km s^{-1})	-1.21 ± 0.18	[-5, 5]
$\Delta RV_{Aa,Ab}$ (km s^{-1})	-0.23 ± 0.17	[-5, 5]
Error Scaling Factors		
$f_{Aa, Tomkin}$	1.41 ± 0.26	[-5, 5]
$f_{Ab, Tomkin}$	0.78 ± 0.14	[-5, 5]
$f_{B, Tomkin}$	1.36 ± 0.24	[-5, 5]
$f_{Aa, TRES}$	1.01 ± 0.25	[-5, 5]
$f_{Ab, TRES}$	1.04 ± 0.20	[-5, 5]
$f_{B, TRES}$	0.76 ± 0.17	[-5, 5]
$f_{Aa, Griffin}$	1.05 ± 0.12	[-5, 5]
$f_{Aa, DS}$	1.55 ± 0.17	[-5, 5]
f_θ	1.90 ± 0.37	[-5, 5]
f_ρ	1.71 ± 0.36	[-5, 5]
Derived Properties		
i_{AB} (deg)	61.08 ± 0.64	...
e_{AB}	0.259 ± 0.015	...
ω_B (deg)	85.5 ± 1.7	...
a (au)	22.72 ± 0.36	...
e_A	0.0967 ± 0.0019	...
ω_{Aa} (deg)	240.18 ± 0.83	...
M_A (M_\odot)	1.351 ± 0.046	...
M_B (M_\odot)	0.614 ± 0.021	...
$q_{AB} \equiv M_B/M_A$	0.454 ± 0.020	...
M_{Aa} (M_\odot)	0.745 ± 0.025	...
M_{Ab} (M_\odot)	0.606 ± 0.021	...
$q_A \equiv M_{Ab}/M_{Aa}$	0.8129 ± 0.0022	...
π_{orb} (mas)	21.47 ± 0.20	...
Distance (pc)	46.58 ± 0.44	...

Note. — The solution accounts for light travel time in the outer orbit. The values listed correspond to the mode of the posterior distributions from our MCMC analysis, with uncertainties representing the 68.3% credible intervals. The f symbols represent multiplicative scaling factors for the nominal errors of the radial velocity and astrometric measurements, solved for simultaneously with the other elements. Priors in square brackets are uniform over the ranges specified, except those for the error inflation factors f , which are log-uniform.

than the one reported by Tokovinin (2021b). Our position angle for the ascending node in the outer orbit (Ω_{AB}) and the argument of periastron for the tertiary (ω_B) are in the opposite quadrant compared to his, as his solution did not make use of radial velocities to remove the 180° ambiguity. Other elements show minor

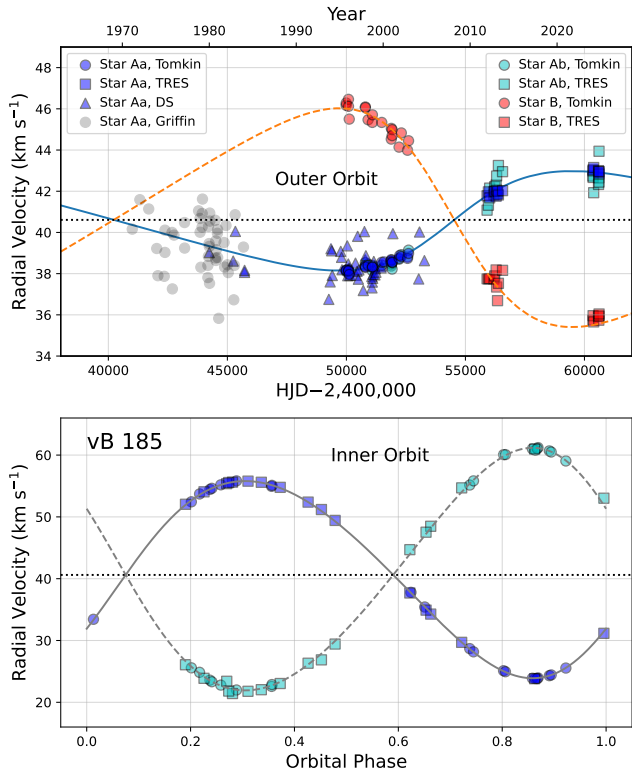


Figure 28. *Top:* Outer spectroscopic orbit for vB 185, with the RV measurements from Tomkin (2003), Griffin et al. (1985a), and CfA (Digital Speedometers and TRES). Motion in the inner binary has been subtracted from the measurements of Aa and Ab. For the Digital Speedometer and Griffin velocities, this was done using the corresponding semiamplitudes $K_{Aa,DS}$ and $K_{Aa,Griffin}$; for those from TRES and Tomkin (2003), we used K_{Aa} (see Table 21). The dotted line represents the center-of-mass velocity of the triple. *Bottom:* Inner orbit (symbols as in the top panel).

differences. And as anticipated, the primary velocity semiamplitudes from the Griffin and Digital Speedometer velocities (14.19 ± 0.22 and 15.00 ± 0.16 km s⁻¹, respectively) are significantly smaller than the value constrained by the Tomkin and TRES observations, which resolve all three stars ($K_{Aa} = 15.950 \pm 0.027$ km s⁻¹). The inclination angle for the inner orbit is inferred to be $79^\circ \pm 3^\circ$. We show the inner and outer spectroscopic orbits in Figure 28, along with our model, and the astrometric orbit in Figure 29.

Our dynamical mass measurements for vB 185, coupled with estimates of the intrinsic brightness of each component, offer a chance to compare them against other similar measurements in the Hyades, and with models of stellar evolution. We estimated the apparent visual magnitude of each of the three stars by converting our spectroscopic flux ratios at ~ 5187 Å to the visual band, using PHOENIX spectra from Husser et al. (2013), and adopting a total apparent brightness for the system of $V = 9.472 \pm 0.004$. The distance modulus was based on the distance in Table 21. We obtained absolute visual magnitudes for stars Aa, Ab, and B of 6.524 ± 0.027 , 8.229 ± 0.068 , and 8.129 ± 0.073 , respectively.¹² As seen

¹² These values imply a magnitude difference between the tertiary and the inner binary of $\Delta V = 1.81 \pm 0.08$. This is close to the average of the three available direct measurements of this difference from the WDS, at wavelengths near the V band (1.84 ± 0.07 ;

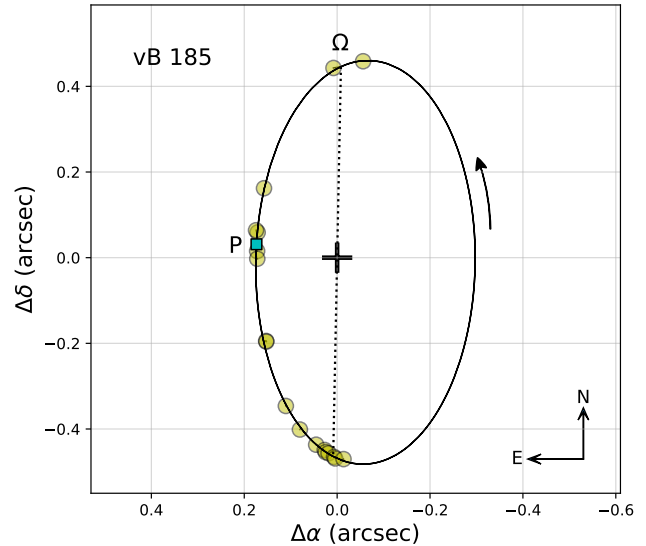


Figure 29. Astrometric orbit of vB 185, with the measurements from the WDS. Two lunar occultation observations, which are one-dimensional, were not used. The dotted line represents the line of nodes, and “Ω” marks the ascending node. Periastron is indicated with the square labeled “P”.

in Figure 25, although the slope from the measurements for vB 185 is consistent with the trend from other binaries in the Hyades and from the models, all three components fall slightly above the isochrones. This is likely due to a bias in our masses, caused by the challenges noted earlier. A more definitive comparison with theory must await a more complete coverage of the outer orbit from both astrometric and spectroscopic observations.

(545) VB 149

This is a close visual pair of nearly equally bright components (WDS 04574+0100, HD 31622, $\rho \approx 0''.3$; Aitken 1914). The binary nature of the object has compromised the astrometric solution from Gaia DR3 (2/3 of the image profiles were found to be double-peaked), and no parallax or proper motion were reported in the catalog. However, the parallax and proper motion from the Hipparcos catalog (source HIP 23044) indicate it is not a member of the Hyades, and the distance places it well below the cluster main sequence.

A handful of early RV measurements of a blend of the two components made between 1973 and 1992 (Griffin et al. 1988; CORAVEL¹³) showed no change with time, and confirmed it as a non-member. Our own observations between 1992 and 1999 supported those findings. In 2004 the spectra we gathered changed character, and appeared clearly double-lined for a period of about two months. Subsequent observations after 2005 were single-lined again, or showed slight broadening. This suggested we caught the periastron passage in a possibly very eccentric binary with a long orbital period, most likely containing the same companion discovered by the visual observers. Analysis with TODCOR allowed us to measure the velocities of both components in all our spectra, with adopted template parameters of $T_{\text{eff}} = 5750$ K for both

ESA 1997; Horch et al. 2010).

¹³ <https://webda.physics.muni.cz/>

Table 22
Orbital Parameters for vB 149

Parameter	Value	Prior
P (day)	11597 ± 61	[6000, 20000]
T_{peri} (BJD-2,400,000)	53071.9 ± 4.4	[52000, 54000]
a'' (")	0.1732 ± 0.0016	[0.02, 0.20]
$\sqrt{e} \cos \omega_1$	$+0.9437 \pm 0.0037$	[-1, 1]
$\sqrt{e} \sin \omega_1$	-0.096 ± 0.021	[-1, 1]
$\cos i$	-0.142 ± 0.034	[-1, 1]
Ω (deg)	124.96 ± 0.55	[0, 360]
K_1 (km s $^{-1}$)	13.59 ± 0.42	[1, 30]
K_2 (km s $^{-1}$)	13.93 ± 0.47	[1, 30]
γ (km s $^{-1}$)	$+36.907 \pm 0.073$	[0, 60]
Error Scaling Factors		
f_θ	1.84 ± 0.42	[-5, 5]
f_ρ	1.73 ± 0.40	[-5, 5]
f_1	1.00 ± 0.17	[-5, 5]
f_2	1.01 ± 0.17	[-5, 5]
Derived Properties		
i (deg)	98.2 ± 1.9	...
e	0.9000 ± 0.0050	...
ω_1 (deg)	354.2 ± 1.3	...
a (au)	12.93 ± 0.36	...
M_1 (M_\odot)	1.083 ± 0.096	...
M_2 (M_\odot)	1.058 ± 0.089	...
$q \equiv M_2/M_1$	0.977 ± 0.037	...
π_{orb} (mas)	13.41 ± 0.38	...
Distance (pc)	74.6 ± 2.2	...

Note. — The values listed correspond to the mode of the posterior distributions from our MCMC analysis, with uncertainties representing the 68.3% credible intervals. The argument of periastron listed (ω_1) is for the primary. The symbols f_θ and f_ρ represent multiplicative scaling factors for the nominal errors of the astrometric measurements, solved for simultaneously with the other elements, and f_1 and f_2 are the corresponding factors for the primary and secondary radial velocities. Priors in square brackets are uniform over the ranges specified, except those for the error inflation factors f , which are log-uniform.

stars, along with $v \sin i$ values of 5 and 4 km s $^{-1}$ for the primary and secondary components, respectively. The flux ratio we determined is $\ell_2/\ell_1 = 0.780 \pm 0.036$. However, the orbital period cannot be determined from the velocities alone.

Fortunately, the measurements of the relative position of vB 149 going back to 1913 complement the spectroscopy very well, and allow the period to be determined reliably. We used a listing of all such measurements from the WDS, together with our velocities, to carry out a joint MCMC astrometric-spectroscopic orbital solution. The resulting elements and derived properties are presented in Table 22. The orbit is indeed very eccentric ($e = 0.9000 \pm 0.0050$), quite close to edge-on ($i = 98.2 \pm 1.9^\circ$), and has a period of 31.8 yr.

Figure 30 displays the spectroscopic model with our velocities. The top panel of Figure 31 shows that, because of the high eccentricity, the binary has only been spatially resolved near its maximum angular separation. The lower panels display the measurements as a function of time, which cover about two and a half orbital cycles.

The original Hipparcos catalog (ESA 1997) reported a parallax of 12.62 ± 1.89 mas. The revised version of the catalog (van Leeuwen 2007) gave 12.27 ± 1.76 mas. The orbital parallax we obtain here, 13.41 ± 0.38 mas, is several times more precise, but is consistent with the earlier estimates within their larger uncertainties. The

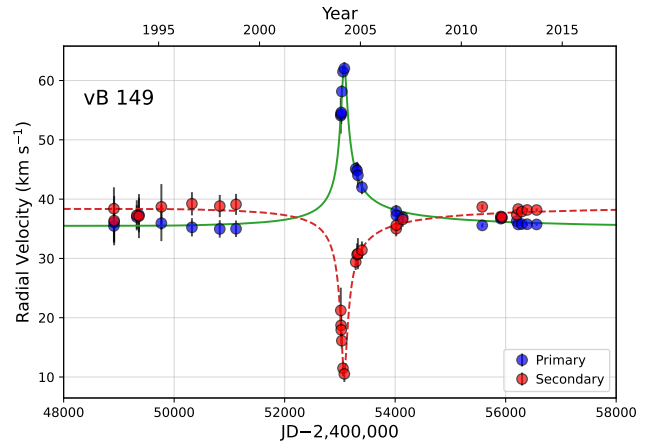


Figure 30. Radial velocity measurements of vB 149, with our model for the spectroscopic orbit.

corresponding distance is 74.6 ± 2.2 pc, far behind the cluster. Both components are of solar type, with masses marginally larger than the Sun.

Because of the very elongated shape of its orbit, vB 149 is relatively rare among the known visual binaries, as is the system vB 80 discussed earlier ($e = 0.915$). Only about 5.5% of all systems in the Sixth Catalog of Orbits of Visual Binary Stars (Hartkopf et al. 2001) have eccentricities as high as 0.9 or higher. While the maximum separation between the components of vB 149 is about 24.6 au, at periastron they come within just 1.3 au of each other.

(585) HD 34031

Our 9 RVs (one from the year 2000, and the others from 2012–2014) show a clear variation (see Table 3), but are not sufficient to establish an orbit. By adding 4 measurements from the public Elodie archive¹⁴ (2004–2005) and 7 measurements from the public Sophie archive¹⁵ (2009–2010), we were able to establish that this is a triple system. We adopted individual RV uncertainties for these two data sets of 0.20 and 0.12 km s $^{-1}$, respectively. The inner orbital period is 78.5 d, and the outer period appears to be 850 d, although we consider the latter to be somewhat tentative at the present time, given the small number of observations. The elements of our preliminary orbital solution that solves for both orbits simultaneously are given in Table 23. The center-of-mass velocity clearly indicates HD 34031 is not a member of the Hyades.

The ratio of the outer and inner periods is among the smallest known (~ 10.8). An alternative outer period of about 480 d is also possible, and would imply a period ratio of only ~ 6 , although we consider it less likely. That solution gives an rms residual somewhat larger than the model we favor. Plots of our preferred model with the observations are shown in Figure 32.

APPENDIX B: NOTES

In the following we include additional information of interest for selected targets in our sample. In more than two dozen cases, an object in our survey forms a wide

¹⁴ <http://atlas.obs-hp.fr/elodie/>

¹⁵ <http://atlas.obs-hp.fr/sophie/>

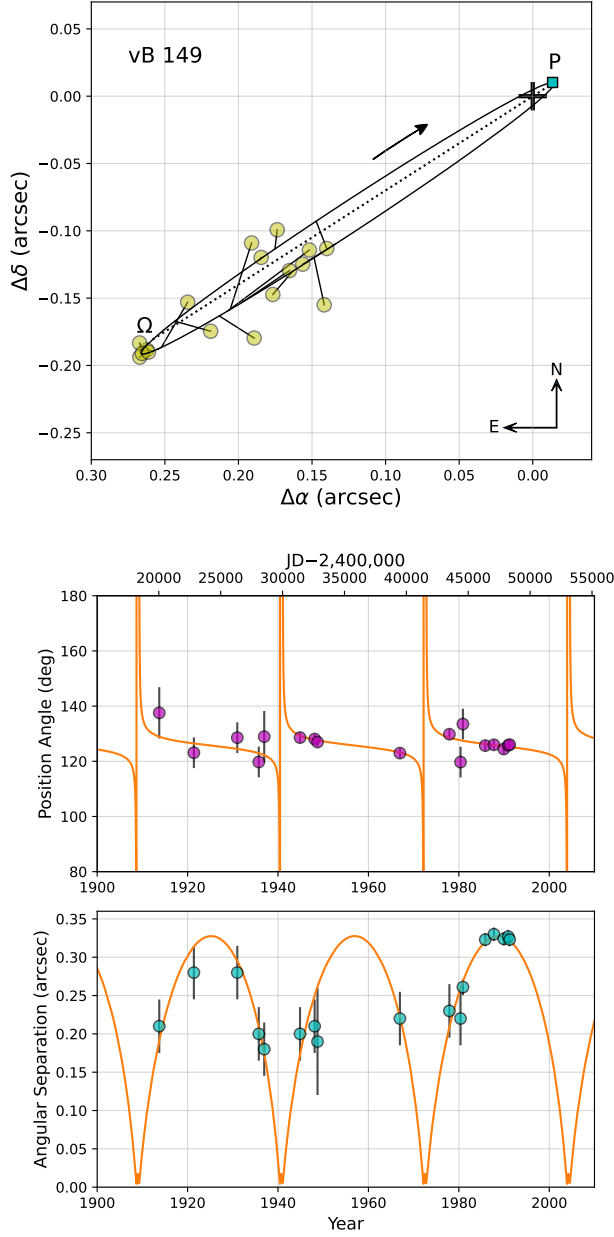


Figure 31. *Top:* Measured positions of the secondary of vB 149 relative to the primary (plus sign) on the plane of the sky. Periastron is indicated with a square labeled “P”, and the dotted line represents the line of nodes. The letter “Q” marks the ascending node, at which the secondary is receding from the observer. *Middle and bottom:* Position angles and separations as a function of time, shown with our model.

physical pair with another survey target. We list all such cases with angular separations up to $30''$ in Table 24. About half of these pairs are considered members of the cluster. In several instances one or the other component, or both, are themselves binaries, implying a higher multiplicity system. Other targets have even wider companions listed in the WDS, which we do not include here.

In several cases the Hipparcos intermediate astrometric data (abscissa residuals) have sufficient precision to detect the motion of the center-of-light of SB1 or SB2 systems, when the phase coverage is reasonably com-

Table 23
Orbital Parameters for HD 34031

Parameter	Value	Prior
P_A (day)	78.5400 ± 0.0058	[50, 100]
$T_{\text{peri},A}$ (BJD-2,400,000)	55114.91 ± 0.70	[55100, 55170]
$\sqrt{e_A} \cos \omega_{Ab}$	$+0.234 \pm 0.011$	[-1, 1]
$\sqrt{e_A} \sin \omega_{Ab}$	$+0.141 \pm 0.013$	[-1, 1]
K_{Aa} (km s^{-1})	11.867 ± 0.047	[5, 20]
P_{AB} (day)	848.9 ± 1.9	[300, 1000]
$T_{\text{peri},AB}$ (BJD-2,400,000)	54721.9 ± 4.7	[54500, 55300]
$\sqrt{e_{AB}} \cos \omega_A$	$+0.476 \pm 0.019$	[-1, 1]
$\sqrt{e_{AB}} \sin \omega_A$	$+0.400 \pm 0.035$	[-1, 1]
K_A (km s^{-1})	3.721 ± 0.077	[1, 5]
γ (km s^{-1})	$+13.474 \pm 0.082$	[0, 20]
ΔRV (km s^{-1})	$+0.703 \pm 0.065$	[-5, 5]
Derived Properties		
e_A	0.0750 ± 0.0043	...
ω_{Aa} (deg)	31.0 ± 3.2	...
$a_{Aa} \sin i$ (10^6 km)	12.782 ± 0.051	...
$M_{Ab} \sin i / (M_{Aa} + M_{Ab})^{2/3}$	0.23806 ± 0.00094	...
e_{AB}	0.386 ± 0.027	...
ω_A (deg)	39.5 ± 3.1	...
$a_A \sin i$ (10^6 km)	40.21 ± 0.56	...
$M_B \sin i / (M_A + M_B)^{2/3}$	0.1531 ± 0.0021	...

Note. — The values listed correspond to the mode of the posterior distributions from our MCMC analysis, with uncertainties representing the 68.3% credible intervals. ΔRV represents a systematic velocity offset between the Sophie and Elodie measurements and our own. Priors in square brackets in the last column are uniform over the ranges specified, except those for the error inflation factors, which are log-uniform. Light travel time effects have been accounted for in the solution.

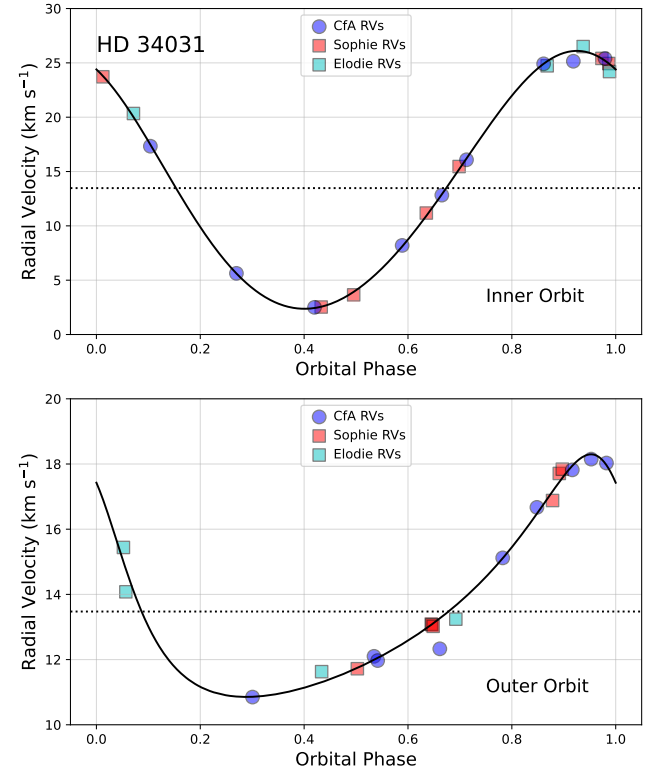


Figure 32. RV measurements of HD 34031, together with our models for the inner and outer orbits. In each case, the motion in the other orbit has been subtracted for display purposes. The dotted line represents the center-of-mass velocity.

Table 24
Physical Pairs With Separations under 30'' Among the Survey Targets

Visual Primary	Visual Secondary	G_{prim} (mag)	G_{sec} (mag)	ρ ('')	Memb.	Prim. Binarity	Sec. Binarity
(5) HD 15128A	(6) HD 15128B	7.77	9.31	1.41	NM	DUP	DUP
(10) HD 17383	(9) HIP 13042	8.95	10.31	23.88	NM	DUP	...
(11) G 75-42A	(12) G 75-42B	11.39	11.99	1.30	NM	VAR,DUP,RUWE	DUP,RUWE
(27) BD+25 522A	(26) BD+25 522B	10.57	12.42	3.23	M	RUWE	...
(32) HIP 15368A	(31) HIP 15368B	11.56	12.59	0.89	NM	DUP,RUWE	DUP
(40) vB 3	(41) vB 207	8.13	10.12	19.91	NM	SB1,DUP,RUWE,VBO	...
(48) LP 413-18	(49) LP 413-19	11.69	12.08	16.15	M	SB2,DUP,RUWE	SB2,RUWE
(73) HD 24098A	(72) HD 24098B	6.40	10.08	4.59	M
(88) LP 474-428 A	(89) LP 474-428 B	13.13	13.40	2.21	M	DUP,RUWE	DUP,RUWE
(96) HD 25068A	(97) HD 25068B	9.93	12.35	4.29	NM	RUWE	...
(111) HG 7-73A	(112) HG 7-73B	11.33	11.75	5.50	M	RUWE	...
(134) G 39-1A	(133) G 39-1B	7.04	8.95	2.82	NM	VAR,ACC	VAR,DUP
(136) vB 11	(135) vB 12	5.98	8.68	3.58	M	DUP	LT,RUWE
(143) LP 357-168 A	(144) LP 357-168 B	12.55	12.65	1.76	M	DUP	DUP
(154) REID 88	(153) REID 88B	12.36	13.77	5.55	M	VAR,LT,DUP,RUWE	...
(162) PELS 20	(161) HD 284163B	9.07	13.29	5.07	M	SB3p,DUP,RUWE,ACC,vbop	...
(250) HD 27691	(249) HD 27691B	7.14	8.37	1.25	M	SB2,DUP,ACC,vbo	DUP
(277) vB 140	(276) vB 140B	8.73	12.95	7.11	NM	SB2,RUWE,ACC,vbo	SB2,RUWE
(296) EPIC 210953703	(295) EPIC 210953791	10.96	11.09	5.48	NM	VAR,DUP,RUWE	...
(301) vB 56	(300) HD 27962B	4.30	8.10	1.81	M	ACC	LT
(345) HAN 432	(346) HG 7-232B	11.36	13.23	1.67	M	SB1,DUP,RUWE	DUP
(440) HD 29205A	(439) HD 29205B	8.79	9.08	2.02	NM	SB1,RUWE	...
(501) LP 416-565	(502) LP 416-566	12.54	13.17	3.54	M	RUWE	...
(531) HD 284908	(530) vB 145	9.30	10.96	3.91	NM	VAR,RUWE	...
(553) HD 31734A	(552) HD 31734B	8.10	10.23	1.68	NM	DUP	...
(577) vB 131	(578) vB 132	5.97	8.94	11.42	M	VB	DUP,VB
(616) HD 39251A	(617) HD 39251B	7.82	9.55	2.51	NM	SB1	...

Note. — After the SIMBAD names of the brighter and fainter component of each pair, the columns list the Gaia magnitudes, the angular separation based on the Gaia DR3 positions, membership, and the binarity codes as described in Section 8.

plete. This allows the inclination angle i to be determined, along with the semimajor axis of the photocenter (a''_{phot}) and the position angle of the ascending node (Ω). We report those results in Table 25, from separate solutions we carried out for each system.

(39) BD+12 479. – The 6.88-day SB1 orbit we report is considered to be preliminary because of the small number of observations.

(50) vB 5. – The long-term downward velocity trend we observe is supported by earlier RVs by Griffin et al. (1988), and others, as well as by the high-precision measurements by Paulson et al. (2004), who reported a slope of -0.1364 m s^{-1} per day over a period of about 6 yr. This is likely due to the 0''.8 speckle companion detected by Patience et al. (1998). No additional companions were found in adaptive optics imaging by Guenther et al. (2005).

(53) BD+05 526. – This is listed as an eclipsing binary with a period of 13.25 d (Prša et al. 2022). Our observations show no significant change in velocity, and no sign of double lines. It has a 0''.6 visual companion.

(68) LP 357-4. – RVs for this object were published previously by Torres et al. (2021) as part of a survey of the Pleiades region, and indicated no significant change. New velocities since then have now revealed this to be an SB1, and a member of the Hyades, with elevated chromospheric activity.

(81) HG 7-33. – Stauffer et al. (1997) tentatively identified this object as being double-lined.

(102) PELS 9. – This is listed in the literature as an

exoplanet host (Kepler/K2 designation K2-111 b). It is not a member of the cluster.

(120) HD 25444. – Our RVs (consistent with a few by Tokovinin & Smekhov 2002) show a slight increase with time. Much older (1917–1918) RVs from Mount Wilson strengthen the trend, which is consistent with what is expected in the 496 yr astrometric orbit reported for the object (Table 10). While the current mean RV is 3 km s^{-1} lower than expected, it is trending in the right direction for membership. We tentatively classify the target as ‘M?’.

(128) HG 7-92. – Although the period is well determined, some of the other orbital elements are still somewhat uncertain because the observations do not cover the periastron passage.

(130) vB 231. – This cluster member has a substellar companion (a hot Jupiter) reported by Quinn et al. (2014). We do not consider the planet in the present study, which only deals with stellar companions.

(134/133) G 39-1 A/B. – A premature astrometric orbit has been reported for this $\sim 3''$ common proper motion pair, with a period of 590 yr (Table 10). They are non-members.

(170) vB 17. – Paulson et al. (2004) reported a downward trend in their RV measurements of about 180 m s^{-1} over 2000 d.

(250/249) HD 27691 A/B. – This is a hierarchical triple system and a member of the cluster, in which the visual primary is an SB2 and the tertiary is about $1''.2$ away. Our orbit for the SB2 is listed in Table 6. A visual orbit

Table 25
Survey Targets With Photocenter Motion Detectable in the Hipparcos Observations

Target	Memb.	SB1/SB2	P (days)	a''_{phot} (mas)	i (deg)	Ω (deg)
(7) G 36-30	NM	SB1	1228	41.2 ± 7.1	76.3 ± 3.2	49.1 ± 6.7
(14) HD 17922	M	SB1	319	9.9 ± 1.3	116.8 ± 7.2	230.8 ± 5.0
(103) vB 8	M	SB1	856	8.07 ± 0.72	89.8 ± 7.3	190.6 ± 9.7
(257) vB 43	M	SB2	590	7.0 ± 1.8	21 ± 69	6 ± 11
(343) vB 68	M	SB2	330	9.2 ± 1.4	99 ± 10	137 ± 11
(362) vB 77 ^a	M	SB1	239	10.82 ± 0.98	18 ± 38	308.6 ± 5.8
(378) vB 82	M	SB1	91	1.98 ± 0.64	81 ± 27	1 ± 26
(392) vB 285 ^b	M	SB1	848	12.0 ± 1.5	17 ± 44	218.3 ± 6.6
(443) vB 102	M	SB1	734	9.4 ± 1.3	112.4 ± 7.5	119.7 ± 9.2
(456) HD 29479	NM	SB1	817	10.4 ± 1.3	85.0 ± 4.8	32.0 ± 5.6
(506) vB 115	M	SB1	1203	11.3 ± 1.6	145 ± 27	115.7 ± 7.6
(556) HD 32662 ^c	NM	SB1	998	15.4 ± 1.3	74.9 ± 4.9	335.7 ± 5.5
(569) HD 240622	NM	SB1	649	8.2 ± 1.4	64 ± 12	32.4 ± 8.1
(575) vB 130	M	SB1	156	3.03 ± 0.83	148 ± 73	357 ± 20

^a A similar solution was reported by Jancart et al. (2005).

^b An independent astrometric solution at a different wavelength, based on HST observations, was reported by McArthur et al. (2011).

^c The Hipparcos catalog also reported a solution for the photocenter motion, but adopted an incorrect period (668 d) and assumed a circular orbit.

for the tertiary with a period of 247 yr has been reported by Josties & Mason (2021). We used TRICOR to measure the velocities of all three stars. RVs for tertiary were also measured separately by Griffin (2012), who suggested a very slight downward drift over 37 yr of coverage, consistent with being caused by motion in the 247 yr outer orbit. The inner pair (250) HD 27691 A has been resolved interferometrically using the Center for High Angular Resolution Astronomy (CHARA) array (Schaefer et al. 2022), although the details are not yet available. The orbital elements for that 4 d orbit are listed in the Sixth Catalog of Orbits of Visual Binary Stars (Hartkopf et al. 2001), and include the inclination angle ($48^{\circ}31 \pm 0^{\circ}30$) and the semimajor axis (1.266 ± 0.003 mas). Combining this information with our spectroscopic results, we obtain absolute masses of $1.089 \pm 0.065 M_{\odot}$ and $0.557 \pm 0.020 M_{\odot}$, currently limited by the spectroscopy. The orbital parallax is 21.75 ± 0.38 mas.

(263) HAN 296. – We see no change in the velocities. Stauffer et al. (1997) reported the detection of double lines. They used the designation vA 288.

(270) vB 50. – A preliminary astrometric orbit has been reported by Zirm (2008) with a period of about 112 yr and a semimajor axis of $0''.73$. This is the same orbit as the spectroscopic one, which has a large eccentricity ($e = 0.98$) and a still rather poorly determined period. A solution combining RVs and available astrometry is not entirely satisfactory. The RV measurements are concentrated around the periastron passage.

(275) vB 52. – This object has a close companion at about $1''$ that we do not resolve. Paulson et al. (2004) reported a downward trend in the velocities of 33.3 m s^{-1} per 1000 d, likely related to this companion. Their high-precision RVs show a superimposed variation of unknown origin with a much shorter period, and a very small amplitude of a few tens of m s^{-1} .

(295) EPIC 210953791. – This target shows double lines. Our 5 pairs of RV measurements are listed in Table 4, and used templates with temperatures of 5750 K for both stars along with $v \sin i$ values of 4 and 2 km s^{-1}

for the primary and secondary. The measured flux ratio is $\ell_2/\ell_1 = 0.77 \pm 0.05$. Using the Wilson (1941) method, we obtain a mass ratio of $q = 0.98 \pm 0.03$ and a center-of-mass velocity of $\gamma = 54.4 \pm 0.2 \text{ km s}^{-1}$. This velocity is consistent with the mean RV of another of our targets, (296) EPIC 210953703, which is $5''.5$ away. Gaia reports similar parallaxes and proper motions, suggesting they form a physical pair. Both are non-members.

(301) vB 56. – This is a blue straggler. The astrometric acceleration reported by Gaia is likely due to the $1''.8$ visual companion, which shows long-term changes in its RV.

(316) vB 62. – Gaia DR3 reported a faint companion to this SB1 ($\Delta G = 7.8$ mag) $11''.1$ away with the same parallax and proper motion, suggesting physical association. This would imply the system is triple. The inner binary has been resolved with the CHARA array, and has an orbital inclination angle of $30^{\circ}9 \pm 2^{\circ}1$.

(332) TYC 3333-1738-1. – The 3 spectra we obtained are double-lined; the RVs from TODCOR are listed in Table 4, and used templates with a temperature of 5750 K and no rotation for both stars. The measured flux ratio is 0.785 ± 0.013 at $\sim 5187 \text{ \AA}$. We estimate a mass ratio of $q = 0.971 \pm 0.001$ and a center-of-mass velocity of $10.28 \pm 0.01 \text{ km s}^{-1}$. This target is not a member of the Hyades.

(343) vB 68. – This SB2 has been spatially resolved using the CHARA array, yielding an inclination angle of $114^{\circ}2 \pm 3^{\circ}3$ and a semimajor axis of 26.9 ± 1.6 mas. With this information, we obtained absolute masses for the components of $1.52 \pm 0.14 M_{\odot}$ and $0.884 \pm 0.087 M_{\odot}$ (limited in this case by the astrometry), and an orbital parallax of 21.5 ± 1.4 mas. The inclination angle and position angle of the ascending node, as determined using the Hipparcos intermediate data (Table 25), are consistent with the interferometric values.

(345/346) HAN 432/HG 7-232B. – The primary of this wide pair listed in Table 24 (HAN 432) has a close $0''.14$ companion half a magnitude fainter, reported by Morzinski (2011).

(348) vB 70. – This is ϵ Tau, one of the four giants in the Hyades. A planetary companion has been reported by Sato et al. (2007).

(355) HD 28271. – We have a single RV for this non-member. Tokovinin & Gorynya (2001) and Willmarth et al. (2016) report very similar SB1 orbits with a period of 461 d.

(362) vB 77. – This SB1 was resolved with the CHARA array, giving an inclination angle of $16^{\circ}5 \pm 1^{\circ}3$. Hipparcos detected the wobble of the center of light, and the inferred inclination angle and position angle of the line of nodes (Table 25) are in good agreement with the CHARA values, although they are less precise.

(369) LP 358-348. – Three transiting planets have been discovered around this star, based on photometry from the Kepler/K2 mission (Mann et al. 2018). The system is known in the exoplanet field as K2-136.

(392) vB 285. – An astrometric orbit corresponding to the motion of the photocenter of this SB1 was reported by McArthur et al. (2011), based on measurements with the Hubble Space Telescope. They obtained a semimajor axis of 14.58 ± 0.24 mas and an inclination angle of $134^{\circ}1 \pm 0^{\circ}9$. The Hipparcos observations also reveal this motion, and yield a somewhat similar semimajor axis (at a different wavelength) of 12.0 ± 1.5 mas.

(401) vB 288. – Stauffer et al. (1997) detected and measured the RVs of the secondary of this SB1 on two occasions. They used the designation vA 677.

(423) HAN 601. – A $0^{\prime\prime}08$ companion interior to the one listed by Gaia was reported by Morzinski (2011), and is about 1.8 mag fainter in the H band.

(429) HAN 611. – Tokovinin et al. (2006) reported a period for the outer orbit of this triple system of 406 yr, although it does not appear that a full orbital solution is available. The inner binary is an SB2, and the system is not a member of the Hyades.

(430) vB 184. – Membership of this object in the cluster had long been considered uncertain, until RVs by Griffin (1985b) that predate ours showed an average that matched the expected velocity quite precisely, supporting membership (see also Cudworth 1985). However, our measurements since then have shown a consistent upward trend *away* from the expected velocity (4 km s^{-1} too positive as of 2013). A visual companion that has been followed since 1888 has shown little change in position angle, but a significant decrease in angular separation from $2^{\prime\prime}3$ to $0^{\prime\prime}1$ in 2013. This suggests a highly inclined orbit possibly approaching periastron around 2013, which might explain the velocity changes we see. Three measurements between 2015 and 2017 from Gaia DR2 and the GALAH survey are 1 km s^{-1} lower, and are consistent with that scenario. On this basis, we have listed the object as ‘M?’.

(440/439) HD 29205 A/B. – The components of this $2^{\prime\prime}$ visual binary were observed separately on nights of good seeing, and in combined light on other nights. For the latter spectra we used TODCOR to measure the individual velocities. Component A is an SB1, and both A and B are non-members of the Hyades. A premature visual orbit

based on very little phase coverage has been reported, with a period of 965 yr.

(443) vB 102. – An astrometric orbit for the outer companion of this triple system was reported by Tokovinin (2021c). See also Table 9 and Section 11.3. It is a cluster member, and the inner pair is an SB1.

(448) vB 104. – The secondary in this SB1 has been resolved interferometrically on two occasions at a separation of about 10 mas, and the angular diameter of the primary has also been measured (De Furio et al. 2022). We tentatively detect the secondary in our spectra with TODCOR, but only in about half of the exposures.

(490) vB 142. – It has been claimed (e.g., Díaz et al. 2012) that the 989 d secondary in this SB1 is likely substellar, although this has not been confirmed.

(520) vB 122. – A visual orbit based on Hipparcos data has been reported by Söderhjelm (1999), with a period of 16.28 yr, a semimajor axis for the relative orbit of $0^{\prime\prime}188$, and $e = 0.46$. The Gaia DR3 catalog reports the companion was partially resolved in 21% of the scans. Our RVs, and a few earlier ones from Griffin et al. (1988), show no change and are measured from the blended lines of the components.

(550) HD 31768. – Tokovinin (2014) reported a period estimate of 103 yr for the visual companion.

(578) vB 132. – Several astrometric orbits for the close visual companion of this target have been reported. The latest one, by Docobo & Campo (2020), gives an orbital period of 34.38 yr and a semimajor axis of $0^{\prime\prime}282$. vB 132 is a common proper motion companion of (577) vB 131.

(615) HD 39275. – The 4 spectra we collected are double-lined, and yield a mass ratio of 0.98 ± 0.16 and a center-of-mass velocity of $16.5 \pm 2.2 \text{ km s}^{-1}$, which indicates the system is not a member of the Hyades. The individual velocities are listed in Table 4, and were obtained with adopted temperatures for the templates of 5500 and 5250 K for the primary and secondary, and line broadenings of 12 and 10 km s^{-1} , respectively. The measured flux ratio is 0.406 ± 0.020 .

(616/617) HD 39251 A/B. – The components of this $2^{\prime\prime}5$ visual binary were observed separately on a few nights, and on other nights only the combined light could be observed. For the latter we used TODCOR to disentangle them. Star A is an SB1, and the Gaia parallaxes and proper motions, as well as the mean RVs we measured, indicate that star B is physically associated. They are not members of the cluster.

The spectra on which this work was based were gathered by a large number of colleagues, students, and remote observers over the past 45 years. We thank them all. We are also grateful to R. J. Davis and J. Mink for maintaining the Digital Speedometer and TRES databases, and for help with the reduction software. The anonymous referee is thanked for a careful reading of the manuscript, and for many constructive suggestions. We acknowledge the long-term support from the Smithsonian Astrophysical Observatory that enabled this study, in the form of telescope time and instrumentation.

The research has made extensive use of the SIMBAD and VizieR databases, operated at the CDS, Strasbourg, France, and of NASA’s Astrophysics Data System Abstract Service. We also acknowledge the use of the Fourth Catalog of Interferometric Measurements of Binary Stars (Hartkopf et al. 2001, and online updates), and of the Washington Double Star Catalog (WDS), maintained at the U.S. Naval Observatory. R. Matson (USNO) was helpful in providing individual astrometric measurements from the WDS. The work has used data from the European Space Agency (ESA) mission *Gaia* (<https://www.cosmos.esa.int/gaia>), processed by the *Gaia* Data Processing and Analysis Consortium (DPAC, <https://www.cosmos.esa.int/web/gaia/dpac/consortium>). Funding for the DPAC has been provided by national institutions, in particular the institutions participating in the *Gaia* Multilateral Agreement. The computational resources used for this research include the Smithsonian High Performance Cluster (SI/HPC), Smithsonian Institution (<https://doi.org/10.25572/SIHPC>).

APPENDIX C: ORBIT FIGURES

We include here plots of the RV observations and models for 80 single-lined spectroscopic binaries, of which 30 are new, and 20 double-lined binaries, of which 9 are new. Additional orbits are presented in Appendix B for 5 binaries and 5 triples. Among these, a total of 7 inner or outer spectroscopic orbits are new, along with several of the astrometric orbits.

In addition to these systems, to our knowledge there are four binary or multiple systems in the Hyades with known spectroscopic orbits that host a white dwarf. Three are included in our survey: the eclipsing binary V471 Tau, HAN 346 (a quadruple system), and vB 34 (in which the white dwarf is the tertiary, and has a 184 yr astrometric orbit by Zhang et al. 2023). The fourth white dwarf system is known as HZ 9 (Lanning & Pesch 1981), and is not in our survey.

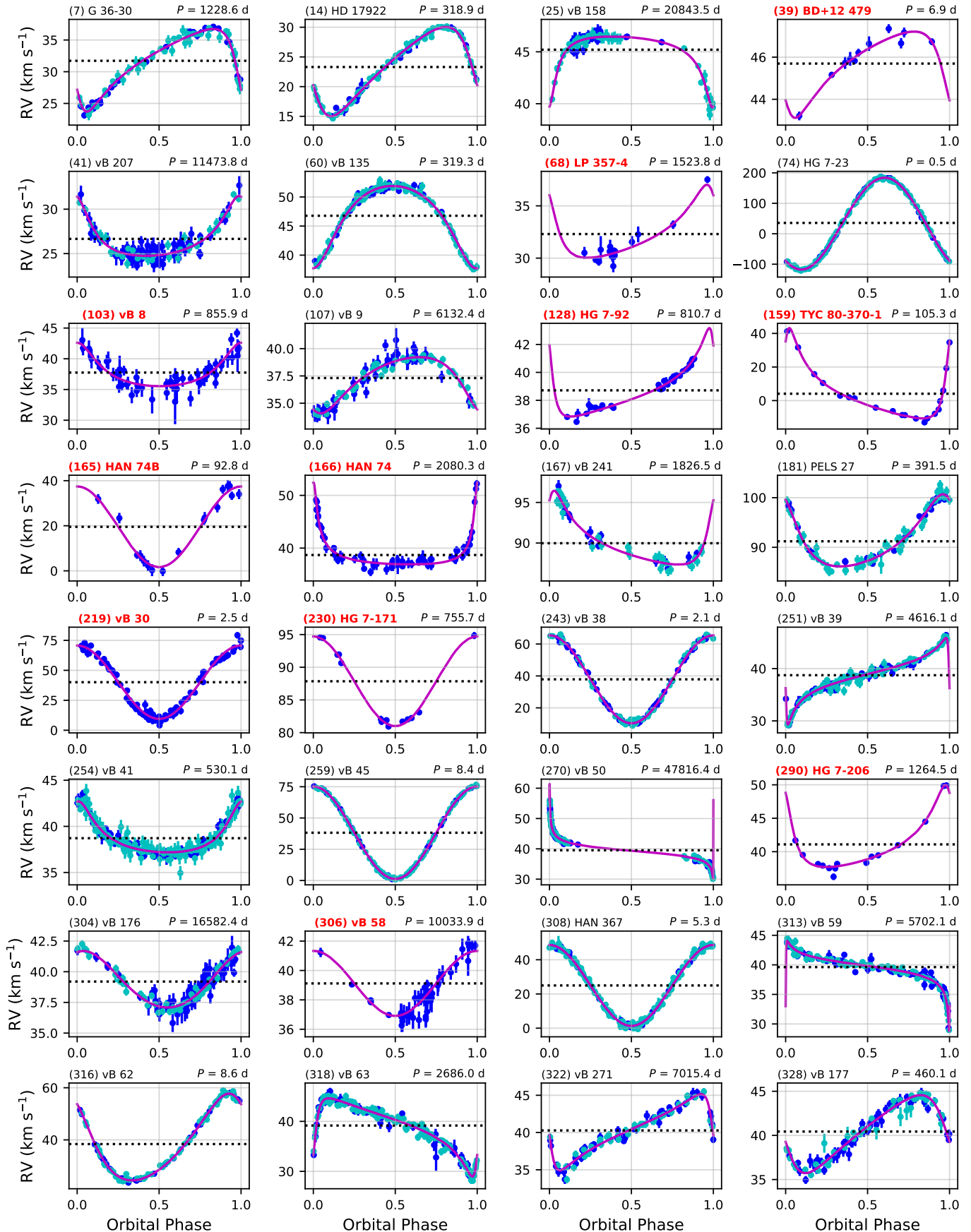


Figure 33. Single-lined spectroscopic orbits. Running numbers, SIMBAD names, and orbital periods are shown on the title line of each panel. For new orbits, the running numbers and SIMBAD names are shown in red. Blue symbols correspond to the CFA observations, and cyan symbols to RVs by others (see Table 5). Our best-fit models are shown by the magenta lines, and the center-of-mass velocity of each system is indicated with a dotted line.

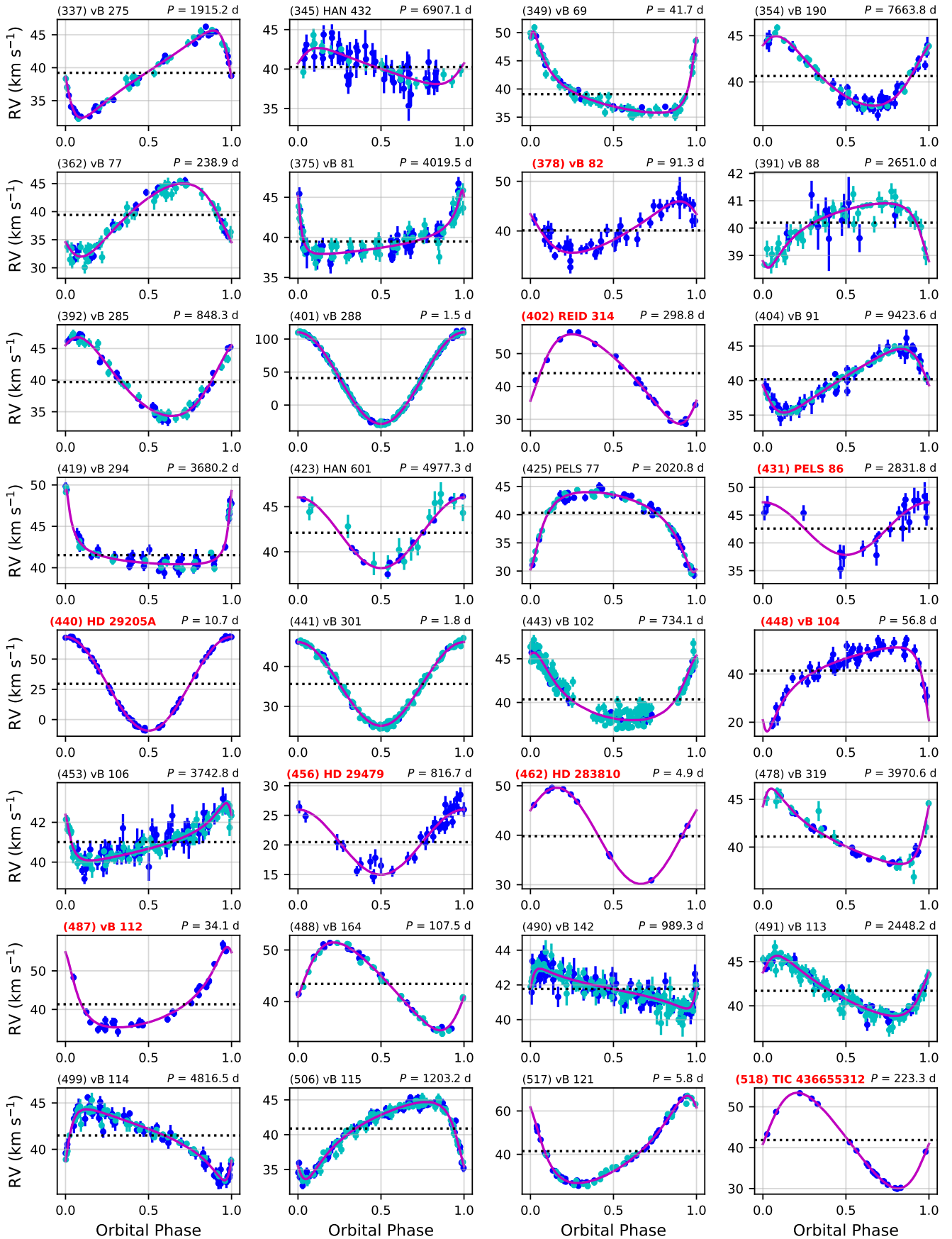


Figure 33. Single-lined spectroscopic orbits (continued).

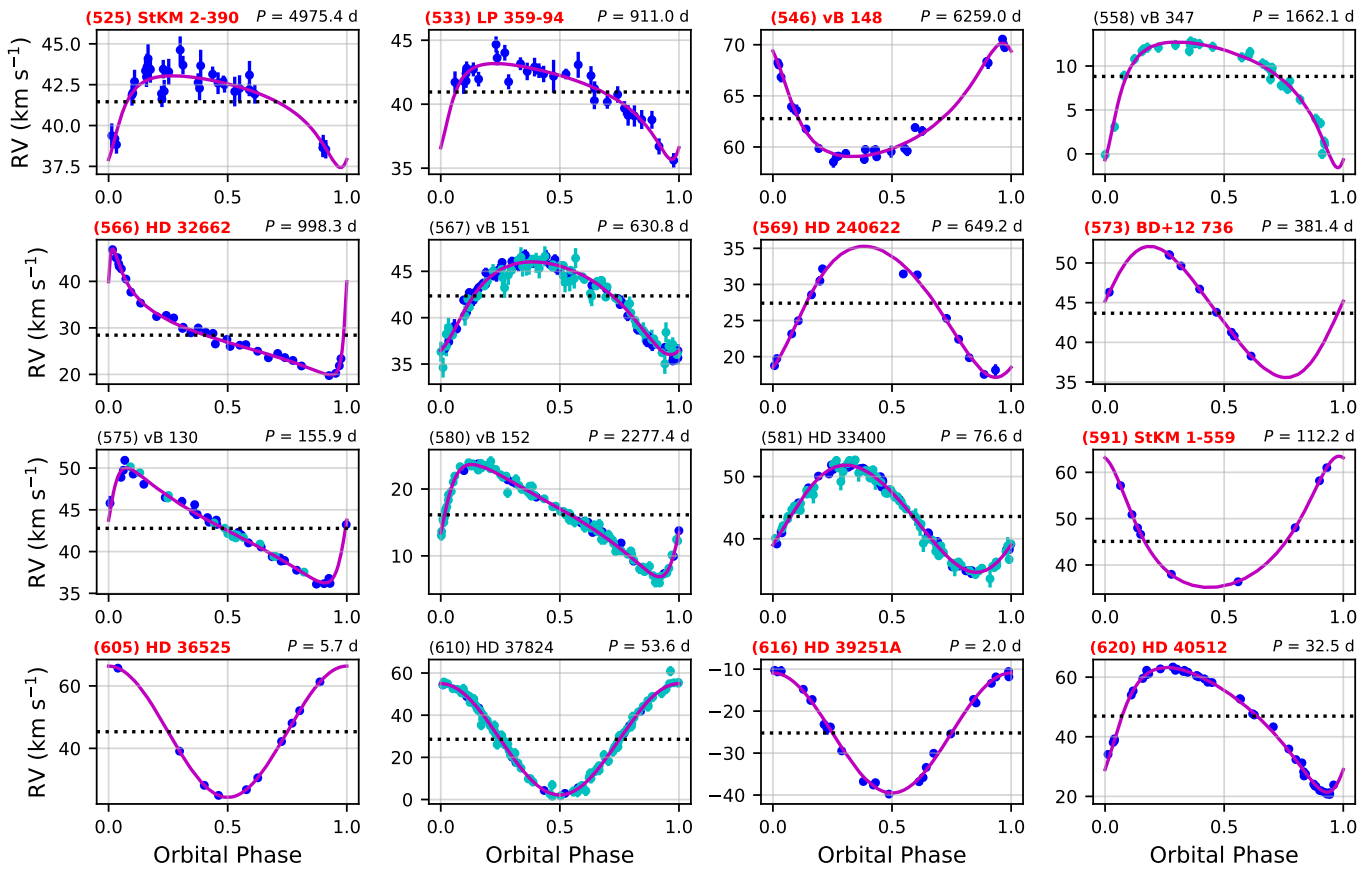


Figure 33. Single-lined spectroscopic orbits (continued).

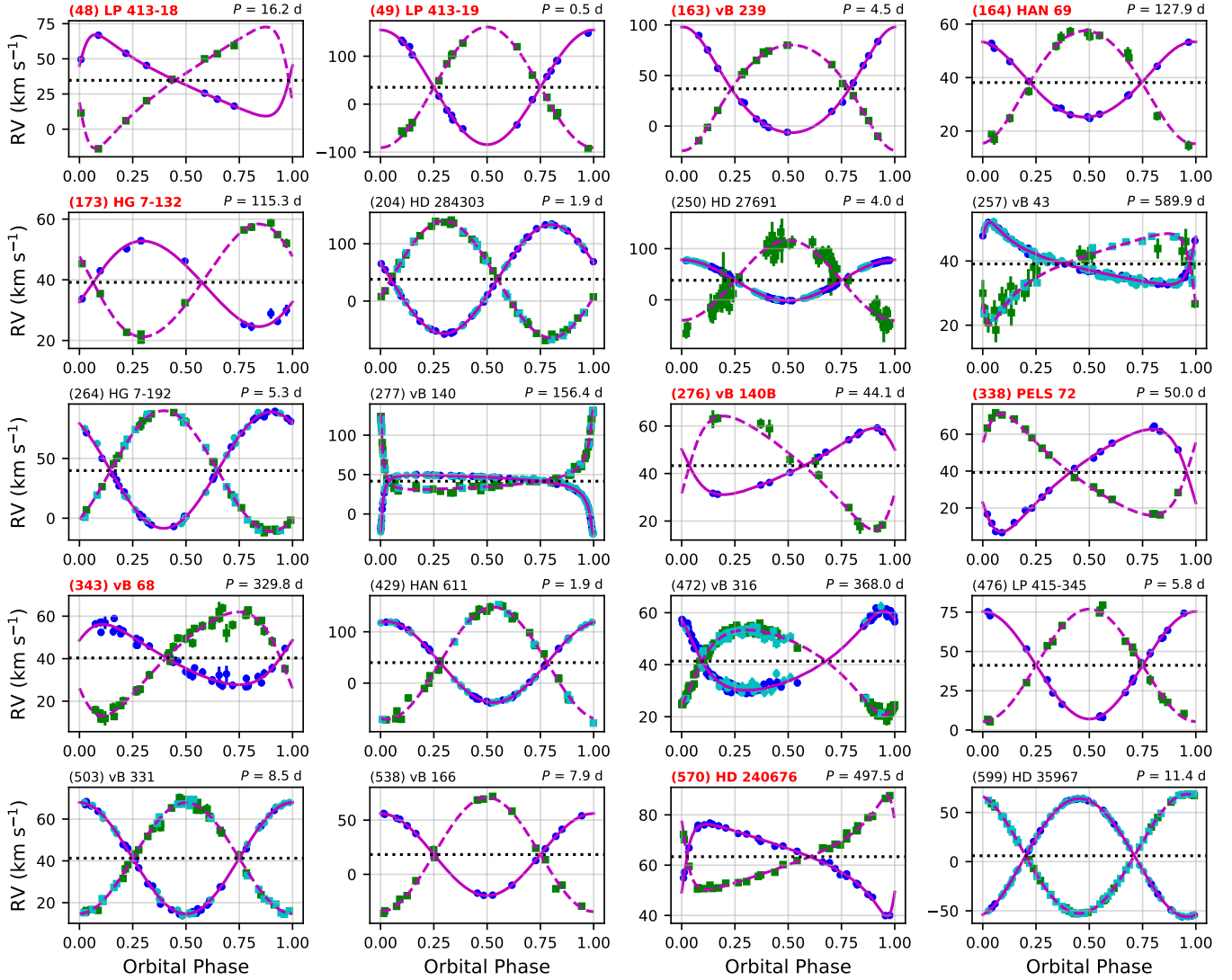


Figure 34. Double-lined spectroscopic orbits. Running numbers, SIMBAD names, and orbital periods are shown on the title line of each panel. For new orbits, the running numbers and SIMBAD names are shown in red. Blue and green symbols correspond to the CfA observations, and cyan symbols to RVs by others (see Table 6). Our best-fit model is shown by the red lines (solid for the primary, dashed for the secondary), and the center-of-mass velocity of each system is indicated with a dotted line.

REFERENCES

- Aitken, R. G. 1914, *Lick Observatory Bulletin*, 251, 52
- Albrow, M. D. 2024, *MNRAS*, 528, 4, 6211
- Altmann, M., Roeser, S., Demleitner, M., et al. 2017, *A&A*, 600, L4
- Babusiaux, C., Fabricius, C., Khanna, S., et al. 2023, *A&A*, 674, A32
- Balona, L. A. 1987, *South African Astronomical Observatory Circular*, 11
- Bashi, D., Mazeh, T., & Faigler, S. 2023, *MNRAS*, 522, 1, 1184
- Bender, C. F. & Simon, M. 2008, *ApJ*, 689, 416
- Benedict, G. F., Franz, O. G., Horch, E. P., et al. 2021, *AJ*, 161, 6, 285
- Beyer, A. C. & White, R. J. 2024, *ApJ*, 973, 28
- Brandt, T. d. 2018, *ApJS*, 239, 31
- Brandt, T. D. 2021, *ApJS*, 254, 42
- Brandt, T. d. 2024, *PASP*, 136, 073001
- Brogaard, K., Pakštienė, E., Grundahl, F., et al. 2021, *A&A*, 645, A25
- Buchhave, L. A., Latham, D. W., Johansen, A., et al. 2012, *Nature*, 486, 375
- Burnham, S. W. 1894, *Publications of Lick Observatory*, 2, 221
- de Bruijne, J. H. J., Hoogerwerf, R., & de Zeeuw, P. T. 2001, *A&A*, 367, 111
- Campbell, W. W. 1910, *PASP*, 22, 131, 47
- Campbell, W. W. 1928, *Publications of Lick Observatory*, 16, 1
- Chen, Y., Girardi, L., Bressan, A., et al. 2014, *MNRAS*, 444, 2525
- Choi, J., Dotter, A., Conroy, C., et al. 2016, *ApJ*, 823, 102
- Conti, P. S. 1969, *ApJ*, 156, 661
- Cudworth, K. M. 1985, *PASP*, 97, 348
- Cutri, R. M., Skrutskie, M. F., van Dyk, S., et al. 2003, *The IRSA 2MASS All-Sky Point Source Catalog, NASA/IPAC Infrared Science Archive* (Washington, DC: NASA)
- Cvetković, Z. & Ninković, S. 2008, *New A*, 13, 587
- De Furio, M., Gardner, T., Monnier, J., et al. 2022, *ApJ*, 941, 118
- Detweiler, H. L., Yoss, K. M., Radick, R. R., et al. 1984, *AJ*, 89, 1038
- Díaz, R. F., Santerne, A., Sahlmann, J., et al. 2012, *A&A*, 538, A113
- Distler, A., Soares-Furtado, M., Vanderburg, A., et al. 2025, *AJ*, 169, 166
- Docobo, J. A., & Campo, P. 2020, *Double Stars Inf. Circ.* 202, 1
- Douglas, S. T., Agüeros, M. A., Covey, K. R., et al. 2014, *ApJ*, 795, 161
- Douglas, S. T., Agüeros, M. A., Covey, K. R., et al. 2016, *ApJ*, 822, 47
- Dravins, D., Lindegren, L., & Madsen, S. 1999, *A&A*, 348, 1040
- Duquenois, A. & Mayor, M. 1991, *A&A*, 248, 485
- Dutra-Ferreira, L., Pasquini, L., Smiljanic, R., et al. 2016, *A&A*, 585, A75
- El-Badry, K., Rix, H.-W., Tian, H., et al. 2019, *MNRAS*, 489, 5822
- ESA 1997, *The Hipparcos and Tycho Catalogues*, ESA Special Publication, Vol. 1200 (Noordwijk: ESA)
- Evans, N. W. & Oh, S. 2022, *MNRAS*, 512, 3846
- Fabricius, C., Luri, X., Arenou, F., et al. 2021, *A&A*, 649, A5
- Fekel, F. C. & Henry, G. W. 2005, *AJ*, 129, 1669
- Fekel, F. C., Scarfe, C. d., Barlow, D. J., et al. 2002, *AJ*, 123, 3, 1723
- Fernández-Hernández, J., & Joliet, E. 2019, *GOST Software User Manual*, Gaia DPAC
- Fűrész, G. 2008, PhD thesis, Univ. Szeged, Hungary
- Freund, S., Robrade, J., Schneider, P. C., et al. 2020, *A&A*, 640, A66
- Friel, E. d. 1995, *ARA&A*, 33, 381
- Gaia Collaboration, Brown, A. G. A., Vallenari, A., et al. 2018, *A&A*, 616, A1
- Gaia Collaboration, Smart, R. L., Sarro, L. M., et al. 2021, *A&A*, 649, A6
- Gaia Collaboration, Vallenari, A., Brown, A. G. A., et al. 2023a, *A&A*, 674, A1
- Gaia Collaboration, Arenou, F., Babusiaux, C., et al. 2023b, *A&A*, 674, A34
- Geller, A. M., Latham, D. W., & Mathieu, R. D. 2015, *AJ*, 150, 97
- Geller, A. M., Hurley, J. R., & Mathieu, R. d. 2013, *AJ*, 145, 8
- Geller, A. M., Mathieu, R. d., Latham, D. W., et al. 2021, *AJ*, 161, 4, 190
- Geller, A. M. & Mathieu, R. d. 2012, *AJ*, 144, 54
- Goodman, J. & Dickson, E. S. 1998, *ApJ*, 507, 2, 938
- Goos, F. 1908, *Dissertation*, Rheinischen Friedrich-Wilhelms Universität of Bonn
- Gossage, S., Conroy, C., Dotter, A., et al. 2018, *ApJ*, 863, 67
- Gosset, E., Damerdjji, Y., Morel, T. et al. 2026, *A&A*, 693, 124
- Griffin, R. F. 1985b, *PASP*, 97, 858
- Griffin, R. F. 2001, *The Observatory*, 121, 244
- Griffin, R. F. 2012, *Journal of Astrophysics and Astronomy*, 33, 29
- Griffin, R. F. 2013, *The Observatory*, 133, 144
- Griffin, R. F. 2016, *The Observatory*, 136, 179
- Griffin, R. F. & Gunn, J. E. 1974, *ApJ*, 191, 545
- Griffin, R. F. & Gunn, J. E. 1978, *AJ*, 83, 1114
- Griffin, R. F., Mayor, M., & Gunn, J. E. 1982, *A&A*, 106, 221
- Griffin, R. F., Gunn, J. E., Zimmerman, B. A., et al. 1985a, *AJ*, 90, 609
- Griffin, R. F., Gunn, J. E., Zimmerman, B. A., et al. 1988, *AJ*, 96, 172
- Guenther, E. W., Paulson, D. B., Cochran, W. D., et al. 2005, *A&A*, 442, 3, 1031
- Gullikson, K., Kraus, A., & Dodson-Robinson, S. 2016, *AJ*, 152, 40
- Gunn, J. E., Griffin, R. F., Griffin, R. E. M., et al. 1988, *AJ*, 96, 198
- Halbwachs, J.-L., Kiefer, F., Lebreton, Y., et al. 2020, *MNRAS*, 496, 1355
- Halbwachs, J.-L., Mayor, M., & Udry, S. 2018, *A&A*, 619, A81
- Halbwachs, J.-L., Pourbaix, D., Arenou, F., et al. 2023, *A&A*, 674, A9.
- Hanson, R. B. 1975, *AJ*, 80, 379
- Hao, C. J., Xu, Y., Hou, L. G., et al. 2024, *ApJ*, 963, 153
- Hartkopf, W. I., Mason, B. D., & Worley, C. E. 2001, *AJ*, 122, 3472
- Høg, E., Fabricius, C., Makarov, V. V., et al. 2000, *A&A*, 355, L27
- Hole, K. T., Geller, A. M., Mathieu, R. D., et al. 2009, *AJ*, 138, 159
- Holl, B., Sozzetti, A., Sahlmann, J., et al. 2023, *A&A*, 674, A10
- Horch, E. P., Falta, D., Anderson, L. M., et al. 2010, *AJ*, 139, 205
- Husser, T.-O., Wende-von Berg, S., Dreizler, S., et al. 2013, *A&A*, 553, A6
- Hut, P., McMillan, S., Goodman, J., et al. 1992, *PASP*, 104, 981
- IJspeert, L. W., Tkachenko, A., Johnston, C., et al. 2024, *A&A*, 691, A242
- Imbert, M. 2006, *Romanian Astronomical Journal*, 16, 3
- Izmailov, I. S. 2019, *Astronomy Letters*, 45, 1, 30
- Jadhav, V. V., Kroupa, P., Wu, W., et al. 2024, *A&A*, 687, A89
- Jancart, S., Jorissen, A., Babusiaux, C., et al. 2005, *A&A*, 442, 365
- Jantzen, K. 1913, *Astronomische Nachrichten*, 196, 117
- Jerabkova, T., Boffin, H. M. J., Beccari, G., et al. 2021, *A&A*, 647, A137
- Josties, J., & Mason, B. D. 2021, *IAU Double Stars Inf. Circ.* 205, 1
- Kraft, R. P. 1965, *ApJ*, 142, 681
- Kraft, R. P. 1967, *ApJ*, 150, 551
- Kurtz, M. J. & Mink, D. J. 1998, *PASP*, 110, 934
- Lanning, H. H. & Pesch, P. 1981, *ApJ*, 244, 280
- Laos, E., Stassun, K. G., & Mathieu, R. d. 2020, *ApJ*, 902, 2, 107
- Latham, D. W. 1985, in *Proc. IAU Coll. 88, Stellar Radial Velocities*, ed. A. G. Philip & D. W. Latham (Schenectady, NY: L. Davis Press), 21
- Latham, D. W. 1992, in *IAU Coll. 135, Complementary Approaches to Double and Multiple Star Research*, ASP Conf. Ser. 32, eds. H. A. McAlister & W. I. Hartkopf (San Francisco: ASP), 110
- Latham, D. W., Nordström, B., Andersen, J., Torres, G., Stefanik, R. P., Thaller, M., & Bester, M. 1996, *A&A*, 314, 864
- Latham, D. W., Stefanik, R. P., Torres, G., Davis, R. J., Mazeh, T., Carney, B. W., Laird, J. B., & Morse, J. A. 2002, *AJ*, 124, 1144
- Leão, I. C., Pasquini, L., Ludwig, H.-G., et al. 2019, *MNRAS*, 483, 5026
- Lebreton, Y., Fernandes, J., & Lejeune, T. 2001, *A&A*, 374, 540
- Leiner, E. M., Mathieu, R. d., Gosnell, N. M., et al. 2015, *AJ*, 150, 1, 10

- Liebing, F., Jeffers, S. V., Zechmeister, M., et al. 2023, *A&A*, 673, A43
- Linck, E., Mathieu, R. d., & Latham, D. W. 2024, *AJ*, 168, 205
- Lindegren, L. 2018, Re-normalising the Astrometric chi-square in Gaia DR2, GAIA-C3-TN-LU-LL-124-01, (Lund: Gaia DPAC)
- Lindegren, L., Bastian, U., Biermann, M., et al. 2021, *A&A*, 649, A4
- Lindegren, L., Madsen, S., & Dravins, D. 2000, *A&A*, 356, 1119
- Lodieu, N., Smart, R. L., Pérez-Garrido, A., et al. 2019, *A&A*, 623, A35
- Lucy, L. B. & Ricco, E. 1979, *AJ*, 84, 401
- Ludendorff, H. 1910, *Astronomische Nachrichten*, 184, 23, 373
- Mann, A. W., Vanderburg, A., Rizzuto, A. C., et al. 2018, *AJ*, 155, 4
- Mason, B. D., McAlister, H. A., Hartkopf, W. I., et al. 1993, *AJ*, 105, 220
- Madsen, S. 2003, *A&A*, 401, 565
- Mason, B. D., Tokovinin, A., Mendez, R. A., et al. 2023, *AJ*, 166, 4, 139
- Mason, B. D., Wycoff, G. L., Hartkopf, W. I., et al. 2001, *AJ*, 122, 3466
- Mathieu, R. d. & Mazeh, T. 1988, *ApJ*, 326, 256
- Mathieu, R. d., Meibom, S., & Dolan, C. J. 2004, *ApJL*, 602, 2, L121
- Mayo, A. W., Dressing, C. d., Vanderburg, A., et al. 2023, *AJ*, 165, 235
- Mayor, M. & Mazeh, T. 1987, *A&A*, 171, 157
- Mazeh, T. 1990, *AJ*, 99, 675
- Mazeh, T. 2008, *EAS Publications Series*, 29, 1
- Mazeh, T. & Goldberg, D. 1992, *ApJ*, 394, 592
- McAlister, H. A., Hartkopf, W. I., Hutter, D. J., et al. 1987, *AJ*, 93, 688
- McArthur, B. E., Benedict, G. F., Harrison, T. E., et al. 2011, *AJ*, 141, 172
- McClure, R. d. 1982, *ApJ*, 254, 606
- McNamara, B. J. & Sekiguchi, K. 1986, *ApJ*, 310, 613
- Meibom, S. & Mathieu, R. d. 2005, *ApJ*, 620, 2, 970
- Meibom, S., Mathieu, R. d., & Stassun, K. G. 2006, *ApJ*, 653, 1, 621
- Meingast, S. & Alves, J. 2019, *A&A*, 621, L3
- Mermilliod, J.-C., Andersen, J., Latham, D. W., et al. 2007, *A&A*, 473, 829
- Mermilliod, J.-C., Grenon, M., & Mayor, M. 2008c, *A&A*, 491, 951
- Mermilliod, J.-C. & Mayor, M. 1999, *A&A*, 352, 479
- Mermilliod, J.-C., Mayor, M., & Udry, S. 2009, *A&A*, 498, 949
- Mermilliod, J.-C., Platais, I., James, D. J., et al. 2008b, *A&A*, 485, 95
- Mermilliod, J.-C., Rosvick, J. M., Duquennoy, A., et al. 1992, *A&A*, 265, 513
- Mermilliod, J.-C., Queloz, D., & Mayor, M. 2008a, *A&A*, 488, 409
- Meunier, N., Mignon, L., & Lagrange, A.-M. 2017, *A&A*, 607, A124
- Milliman, K. E., Mathieu, R. d., Geller, A. M., et al. 2014, *AJ*, 148, 2, 38
- Moe, M. & Di Stefano, R. 2017, *ApJS*, 230, 15
- Morzinski, K. M. 2011, PhD thesis, Univ. of California Santa Cruz
- Muller, P. 1978, *A&AS*, 32, 173
- Murphy, S. J., Moe, M., Kurtz, D. W., et al. 2018, *MNRAS*, 474, 4322
- Narayan, R. S., Linck, E., Mathieu, R. D., & Geller, A. M. 2026, *AJ*, 171, 102
- Nine, A. C., Milliman, K. E., Mathieu, R. d., et al. 2020, *AJ*, 160, 4, 169
- Nordström, B., Latham, D. W., Morse, J. A., et al. 1994, *A&A*, 287, 338
- North, P. & Zahn, J.-P. 2003, *A&A*, 405, 677
- Oh, S. & Evans, N. W. 2020, *MNRAS*, 498, 1920
- Olivares, J., Bouy, H., Dorn-Wallenstein, T. Z., et al. 2025, *A&A*, 693, A12
- Patience, J., Ghez, A. M., Reid, I. N., et al. 1998, *AJ*, 115, 1972
- Paulson, D. B., Cochran, W. d., & Hatzes, A. P. 2004, *AJ*, 127, 3579
- Pels, G., Oort, J. H., & Pels-Kluyver, H. A. 1975, *A&A*, 43, 423
- Penev, K. M. & Schussler, J. A. 2022, *MNRAS*, 516, 6145
- Perryman, M. A. C., Brown, A. G. A., Lebreton, Y., et al. 1998, *A&A*, 331, 81
- Pinsonneault, M. H., Terndrup, D. M., Hanson, R. B., et al. 2003, *ApJ*, 598, 588
- Plaskett, J. S. 1915, *Publications of the Dominion Observatory Ottawa*, 2, 61
- Prša, A., Kochoska, A., Conroy, K. E., et al. 2022, *ApJS*, 258, 16
- Quinn, S. N., White, R. J., Latham, D. W., et al. 2014, *ApJ*, 787, 27
- Raghavan, D., McAlister, H. A., Henry, T. J., et al. 2010, *ApJS*, 190, 1
- Rappaport, S., Deck, K., Levine, A., et al. 2013, *ApJ*, 768, 33
- Reid, N. 1992, *MNRAS*, 257, 257
- Reid, I. N. & Mahoney, S. 2000, *MNRAS*, 316, 827
- Reino, S., de Bruijne, J., Zari, E., et al. 2018, *MNRAS*, 477, 3197
- Risbud, D., Jadhav, V. V., & Kroupa, P. 2025, *A&A*, 694, A258
- Röser, S., Schilbach, E., & Goldman, B. 2019, *A&A*, 621, L2
- Röser, S., Schilbach, E., Piskunov, A. E., et al. 2011, *A&A*, 531, A92
- Russell, H. N. 1914, *ApJ*, 40, 282
- Sato, B., Izumiura, H., Toyota, E., et al. 2007, *ApJ*, 661, 527
- Savanov, I. S. & Dmitrienko, E. S. 2018, *Astronomy Reports*, 62, 238
- Schaefer, G., Anugu, N., Bender, C., et al. 2022, *BAAS*, 240, 305.07
- Schiller, S. J. & Milone, E. F. 1987, *AJ*, 93, 1471
- Schlesinger, F. & Baker, R. H. 1910, *Publications of the Allegheny Observatory of the University of Pittsburgh*, 1, 21, 135
- Schwan, H. 1990, *A&A*, 228, 69
- Shahaf, S., Mazeh, T., & Faigler, S. 2017, *MNRAS*, 472, 4, 4497
- Söderhjelm, S. 1999, *A&A*, 341, 121
- Stauffer, J. R., Balachandran, S. C., Krishnamurthi, A., et al. 1997, *ApJ*, 475, 604
- Stefanik, R. P. & Latham, D. W. 1985, in *IAU Coll. 88, Stellar Radial Velocities*, eds. A. G. D. Philip and D. W. Latham (Schelectady: L. Davis Press), 213
- Stefanik, R. P. & Latham, D. W. 1992, *IAU Colloquium 135: Complementary Approaches to Double and Multiple Star Research*, eds. H. A. McAlister & W. I. Hartkopf (San Francisco: ASP), 32, 173
- Stefanik, R. P., Latham, D. W., & Torres, G. 1999, *IAU Colloq. 170: Precise Stellar Radial Velocities*, 185, 354
- Szentgyorgyi, A. H., & Fűrész, G. 2007, *Precision Radial Velocities for the Kepler Era*, in *The 3rd Mexico-Korea Conference on Astrophysics: Telescopes of the Future and San Pedro Mártir*, ed. S. Kurtz, *RMxAC*, 28, 129
- Tal-Or, L., Trifonov, T., Zucker, S., et al. 2019, *MNRAS*, 484, L8
- Terquem, C., Papaloizou, J. C. B., Nelson, R. P., et al. 1998, *ApJ*, 502, 2, 788
- Tokovinin, A. A. 1990, *Soviet Astronomy Letters*, 16, 440
- Tokovinin, A. 2014, *AJ*, 147, 86
- Tokovinin, A. 2021a, *IAU Inf. Circ.* 203, 3
- Tokovinin, A. 2021b, *IAU Inf. Circ.* 204, 1
- Tokovinin, A. 2021c, *AJ*, 161, 3, 144
- Tokovinin, A. A. & Gorynya, N. A. 2001, *A&A*, 374, 227
- Tokovinin, A., Mason, B. D., Mendez, R. A., et al. 2022, *AJ*, 164, 2, 58
- Tokovinin, A., Mason, B. d., Mendez, R. A., et al. 2024, *AJ*, 168, 28
- Tokovinin, A. A. & Smekhov, M. G. 2002, *A&A*, 382, 118
- Tokovinin, A., Thomas, S., Sterzik, M., et al. 2006, *A&A*, 450, 681
- Tomkin, J. 2003, *The Observatory*, 123, 372
- Tomkin, J. 2005, *The Observatory*, 125, 232
- Tomkin, J. & Griffin, R. F. 2002, *The Observatory*, 122, 1
- Tomkin, J., Griffin, R. F., & Alzner, A. 2007, *The Observatory*, 127, 87
- Torres, G. 2007, *AJ*, 133, 2684
- Torres, G. 2019a, *ApJ*, 883, 105
- Torres, G., Stefanik, R. P., & Latham, D. W. 2019b, *ApJ*, 885, 9
- Torres, G., Latham, D. W., & Quinn, S. N. 2021, *ApJ*, 921, 117
- Torres, G., Neuhäuser, R., & Guenther, E. W. 2002, *AJ*, 123, 1701
- Torres, G., Schaefer, G. H., Stefanik, R. P., et al. 2024a, *ApJ*, 971, 31
- Torres, G., Stefanik, R. P., & Latham, D. W. 2024b, *ApJ*, 960, 121
- Torres, G., Schaefer, G. H., Stefanik, R. P., et al. 2024c, *MNRAS*, 527, 8907
- Torres, G., Stefanik, R. P., Andersen, J., Nördstrom, B., Latham, D. W., & Clausen, J. V. 1997d, *AJ*, 114, 2764

- Torres, G., Stefanik, R. P., & Latham, D. W. 1997a, *ApJ*, 474, 256
Torres, G., Stefanik, R. P., & Latham, D. W. 1997b, *ApJ*, 479, 268
Torres, G., Stefanik, R. P., & Latham, D. W. 1997c, *ApJ*, 485, 167
Vaccaro, T. R., Wilson, R. E., Van Hamme, W., et al. 2015, *ApJ*, 810, 157
van Bueren, H. G. 1952, *Bull. Astron. Inst. Netherlands*, 11, 385
van Leeuwen, F. 2007, *A&A*, 474, 653
Vereshchagin, S. V., Reva, V. G., & Chupina, N. V. 2013, *Astronomy Reports*, 57, 52
Wang, F., Fang, M., Fu, X., et al. 2025, *ApJ*, 979, 92
Wayman, P. A., Symms, L. S. T., & Blackwell, K. C. 1965, *Royal Greenwich Observatory Bulletins*, 98, 33.
Weis, E. W. 1983, *PASP*, 95, 29
Weis, E. W., Deluca, E. E., & Upgren, A. R. 1979, *PASP*, 91, 766
Willmarth, D. W., Fekel, F. C., Abt, H. A., et al. 2016, *AJ*, 152, 46
Wilson, O. C. 1941, *ApJ*, 93, 29
Wilson, R. E. 1948, *ApJ*, 107, 119
Worley, C. E. & Douglass, G. G. 1997, *A&AS*, 125, 523
Wu, Y., Hadden, S., Dewberry, J., et al. 2025, *ApJL*, 982, L34
Zahn, J.-P. 1966, *Annales d'Astrophysique*, 29, 489
Zahn, J.-P. 1975, *A&A*, 41, 329
Zahn, J.-P. 1977, *A&A*, 57, 383
Zahn, J.-P. 1989, *A&A*, 220, 1-2, 112
Zahn, J.-P. & Bouchet, L. 1989, *A&A*, 223, 112
Zanazzi, J. J. 2022, *ApJL*, 929, L27
Zhang, H., Brandt, T. d., Kiman, R., et al. 2023, *MNRAS*, 524, 695
Zirm, H. 2008, *IAU Double Stars Inf. Circ.* 166, 1
Zucker, S., & Mazeh, T. 1994, *ApJ*, 420, 806
Zucker, S., Torres, G., & Mazeh, T. 1995, *ApJ*, 452, 863
Zurhellen, W. 1907, *Astronomische Nachrichten*, 173, 23, 353